Petrology and geochemistry of the Saddle North Cu-Au Porphyry Deposit, British Columbia, Canada.

Luis Fernando Zappa Figueroa

A thesis submitted in partial fulfillment of the requirements for the Degree of Master of Science (Geology)

Supervisors: Dr. Peter Hollings (Lakehead University) and Dr. Shaun Barker (MDRU – Mineral Deposit Research Unit, University of British Columbia)

Department of Geology

Lakehead University

Thunder Bay, Ontario

2025

Abstract

The Saddle North porphyry Cu-Au deposit, northwestern British Columbia, Canada, is located in the Upper Triassic Stuhini Group and is associated with the Late Triassic to Early Jurassic Tatogga Suite intrusions. This study integrates petrographic, geochemical, and geochronological data to characterize the deposit's intrusive evolution, alteration assemblages, and mineralization processes. Four intrusive phases (FQMP-I1 to FQMP-I4) of feldspar-quartz-monzodiorite porphyry were identified based on petrographic and geochemical criteria, demonstrating a progressive compositional evolution and varying intensities of potassic alteration. High-precision LA-ICP-MS U-Pb zircon geochronology yielded crystallization ages ranging from 205.3 \pm 1.7 Ma to 208.2 \pm 1.8 Ma, confirming the temporal overlap between intrusive emplacement and hydrothermal activity. Re-Os dating of molybdenite veins returned a model age of 205.6 \pm 0.8 Ma, corroborating a genetic link between mineralization and magmatism.

Whole-rock geochemistry reveals that the intrusions are alkaline to weakly calc-alkaline, with moderate to strong Nb, Ti, and Eu depletions consistent with subduction-related arc magmas. Micro-XRF maps further constrain the spatial distribution of key alteration minerals and elemental enrichments within the core of the deposit. Eight vein types were recognized and categorized into four paragenetic stages: early (A–D), main (C, F, G), late (E, F, G), and post-mineral (G, H). Early-stage veins (A- and B-type) are associated with magnetite, chalcopyrite, and molybdenite and are found in potassic-altered FQMP-I1 and I2 intrusions. The vein paragenesis and alteration zoning indicate a progressive decline in temperature and fluid metal content during hydrothermal evolution. These findings collectively support a magmatic-hydrothermal continuum model for Saddle North, similar to other porphyry systems in the Golden Triangle, such as Red Chris and Galore Creek, emphasizing its potential as a significant Cu-Au mineralizing centre in the Canadian Cordillera.

Acknowledgements

First and foremost, thank you to Dr. Peter Hollings for his patience and guidance throughout the process of completing this project. The encouragement, constructive criticism, and commitment to helping me accomplish my goals were invaluable.

I am very grateful for the endless support of everyone involved with the Mineral Deposit Research Unit (MDRU). I am especially thankful for the support of Drs. Shaun Barker, Kate Rubingh, Brian McNulty, Kyle Powers, Nikola Denisová, and the entire team, whose vast knowledge of porphyry systems and mineral deposit formation inspires me every day. I would like to thank Newmont Corporation for the conception of this research project and the project funding, as well as the whole exploration team for access to data, drill core, and facilities that were necessary for undertaking my work.

This study was funded by Lakehead University, Newmont Corporation, and a Natural Sciences and Engineering Research Council (NSERC Alliance program) grant to undertake research on a variety of porphyry deposits in British Columbia, with a focus on understanding the timing and genesis of porphyry deposits, magmatic history, fertility, and mineralization. Thank you to all who provided financial support to this project.

Thank you to all the faculty and fellow Lakehead University Department of Geology students for a great learning environment and for providing constructive and new ideas. Thank you also to Kristi Tavener and Jonas Valiunas, who provided valuable assistance with preparing the thin-section samples—likewise, special thanks to the great friends I've made in the department. You guys are the best.

Last but not least, thank you to my lovely wife for always having something insightful to offer, regardless of her endless support during this journey. Thank you to my son, Salomon Zappa Mosquera, for being a reason always to look forward. Thank you to my family for their unwavering support.

Table of Contents

Abstract	ı
Acknowledgements	ii
List of Figures	iv
List of Tables	viii
Chapter 1. Introduction	1
1.1. Objectives	4
1.2. Study Location	5
Chapter 2. Regional Geology	6
Chapter 3. Methodology	18
3.1. Sample Collection	18
3.2. Whole-rock geochemistry	18
3.3. Petrography	20
3.4. Micro-XRF	20
3.5. Geochronology (LA-ICPMS)	20
3.6. Re-Os Geochronology	21
Chapter 4. Results	22
4.1. Petrography	22
4.2. Hydrothermal Alteration	25
4.3. Vein Relationships	28
4.4. Whole rock geochemistry	36
4.5. Geochronology	39
Chapter 5. Discussion	46
Chapter 6. Conclusions	74
References	77
Appendix A. List of samples Saddle North	82
Appendix B. Petrography	83
Appendix C. Geochemistry major (wt.%.) and trace (ppm) element data.	103
Appendix D. Zircon II-Ph data for sample from Saddle North porphyry denosit	112

List of Figures

Figure 1.1. Global distribution of porphyry deposits, primarily located along convergent margins. 2
Figure 1.2. Terrane map showing Triassic–Jurassic assemblages of the Stikinia terrane, British Columbia.
Figure 1.3. Regional geology of the Tatogga property and the location of the Saddle North Project. 5
Figure 2.1. Tectonic realms of the Canadian-Alaskan Cordillera. 7
Figure 2.2. Triassic to Middle Jurassic magmatic belts and related mineral deposits in the Intermontane terranes.
Figure 2.3. Schematic cross-section showing mineralized zones at Saddle North. 10
Figure 2.4. Terrane map and locations of selected alkalic porphyry Cu-Au deposits in British Columbia. 12
Figure 2.5. General stratigraphic sequence of the Saddle North Project. 15
Figure 2. 6. Schematic representation of alteration and mineralization within the intrusive FQMP complex at Saddle North.
Figure 3.1. Drill hole locations within the study area. Indicates key sampling sites used for geological, geochemical, and geochronological data collection.
Figure 4.1. Petrographic characteristics of the FQMP intrusive phases (I1–I4). Highlights key mineralogical and textural differences between intrusive units.
Figure 4.2. Volcanic host rock sample (greenish) crosscut by porphyritic intrusion and calcite—quartz veins. Illustrates the contact zone and hydrothermal overprint.
Figure 4.3. Intrusive breccia with irregular clasts of volcanic host rock and vein structures. Indicates multiple intrusive and mineralizing events (thin section images).
Figure 4.4. Comparison of weakly and intensely potassically altered porphyry intrusions. Shows the irregular distribution of potassic alteration in the core of the system.

magnetite. Demonstrates alteration overprint and vein relationships.	27
Figure 4.6. Phyllic alteration zone intersected by quartz and carbonate veins, with coarse-grained prand magnetite dissemination.	yrite 28
Figure 4.7. Representative vein types classified by mineral assemblage, including quartz—magnetite—p and quartz—K-feldspar associations. Sample corresponds to thin section SSD23LZ073 (the red corresponds to the thin section and core sample).	•
Figure 4.8. Stockwork veins in FQMP-I1, I2, and I3. Illustrates evolving vein mineral assemblages throearly, main, and late mineralization stages.	ough 32
Figure 4.9. Post-mineral and early-stage veins in FQMP-I4 and the Stuhini Group, including molybde bearing quartz veins and late-stage carbonate overprints.	nite- 33
Figure 4.10. Micro-XRF elemental maps showing K and Ca distribution across FQMP phases. Revalteration patterns and late-stage carbonate veining.	veals 34
Figure 4.11. Micro-XRF map of P and Ca distribution in FQMP-I3. Indicates apatite presence and petrogenetic significance.	d its 36
Figure 4.12. Geochemical classification diagrams: A. TAS for plutonic rocks; B. Zr/Ti vs. Nb/Y for volc rocks. Used to distinguish magma types.	canic 37
Figure 4.13. Primitive mantle-normalized trace element spider diagrams for intrusive rocks (FQMP II and host volcanic rocks from Saddle North.	1–I4) 38
Figure 4.14. Concordia plots for zircon U-Pb ages from selected samples.	40
Figure 4.15. Additional concordia plots for zircon grains from dated samples.	41
Figure 4.16. U-Pb zircon age data for host rock sample SSD23LZ103 (Stuhini Group), providing a maxim depositional age constraint.	mum 42

Figure 4.5. Sericite overprinting potassic alteration, cut by quartz—calcite—sulfide veins and disseminated

Figure 4.17. U-Pb zircon age diagrams for several FQMP intrusive samples, documenting the timing of magmatic phases at Saddle North.

Figure 4.18. Quartz—molybdenite veins observed in a sample from the Saddle North intrusive complex. Highlights molybdenite mineralization in the system.

Figure 5.1 μ XRF image of FQMP-I1 showing K-feldspar and biotite alteration halos with disseminated magnetite, typical of potassic zones.

Figure 5.2. Conceptual cross-section of the Saddle North porphyry system. Depicts the distribution of Cu-Au mineralization and potassic alteration across intrusive phases.

Figure 5.3. µXRF images of vein-style mineralization associated with different FQMP phases and volcanic host rock, showing complex vein paragenesis.

Figure 5.4. Spider diagram of average geochemical compositions for the four FQMP intrusive phases at Saddle North.

Figure 5.5. Diagram comparing normalized LREE/MREE (La/Sm)n and MREE/HREE (Dy/Yb)n ratios. Used to interpret REE fractionation trends.

Figure 5.6. Nb/Yb—Th/Yb plot used to evaluate magma source characteristics and tectonic setting of the Saddle North intrusions.

Figure 5.7. Binary diagrams of La/Yb vs Yb, comparing Saddle North rocks to adakitic and typical arcrelated volcanic compositions.

Figure 5.8. Compilation of geochronological data for the FQMP phases. Illustrates the temporal evolution of magmatism in the Saddle North area.

List of Tables

Galore Creek, and Red Chris porphyry deposits.

Table 4.1 Classification of vein sets at the Saddle North porphyry deposit. Potassic alteration is crosscut by multiple quartz-rich vein types, each associated with distinct mineral assemblages and paragenetic stages.
Table 4.2. Summary of LA–ICP–MS U–Pb zircon ages from selected Saddle North samples. 43
Table 4.3. Summary of molybdenite Re-Os geochronology data from the Saddle North Project. Provides age constraints on the timing of mineralization. 45
Table 5.1. Intrusion paragenesis of the feldspar quartz monzodiorite porphyry (FQMP) phases, based on cross-cutting relationships and alteration intensity. 47
Table 5.2. Paragenetic sequence of vein types and their associated hydrothermal alteration assemblages at Saddle North.
Table 5.3. Whole-rock geochemical data summary for each of the FQMP intrusive phases at Saddle North. Used to assess compositional differences and magmatic evolution. 63
Table 5.4. Comparative summary of geological and mineralization features between the Saddle North,

73

Chapter 1. Introduction

Porphyry systems, including both epithermal and porphyry deposits, form some of the largest coppermolybdenum and copper-gold deposits worldwide (Sillitoe, 2010). The deposits typically feature large reserves and are spatially and genetically associated with shallow, felsic to intermediate porphyritic intrusions (Zhai et al., 2011). Globally, Cu-Au porphyry deposits are primarily distributed along subduction boundaries (e.g., island and continental arcs), where ore-forming parental magmas originate from the partial melting of the subducting slab or mantle wedge triggered by slab dehydration (Cooke et al., 2005; Sillitoe, 2010; Fig. 1.1). In the Canadian Cordillera, alkalic porphyry Cu-Au deposits are closely associated with volcanic arc terranes that have been incorporated onto the margin of the former North American continent (Fig. 1.1). Within the Cordillera, two specific arc terranes, the Quesnellia and Stikine terranes, predominantly contribute to the accumulated crust and the formation of porphyry mineralization (Logan & Milhanyuk, 2014; Fig. 1.2).

The Saddle North Project represents an important Cu-Au porphyry deposit within the Iskut district of northwestern British Columbia (Fig. 1.3). The deposit is hosted in Upper Triassic and older rocks that are intruded by the latest Triassic to earliest Jurassic monzonitic intrusive rocks of the regionally developed Tatogga Suite (Greig et al., 2020). The property is underlain by volcano-sedimentary sequences of the Upper Triassic Stuhini and Lower Jurassic Hazelton groups. It is part of a broader, precious metals-rich area commonly referred to as the 'Golden Triangle' (Greig et al., 2020).

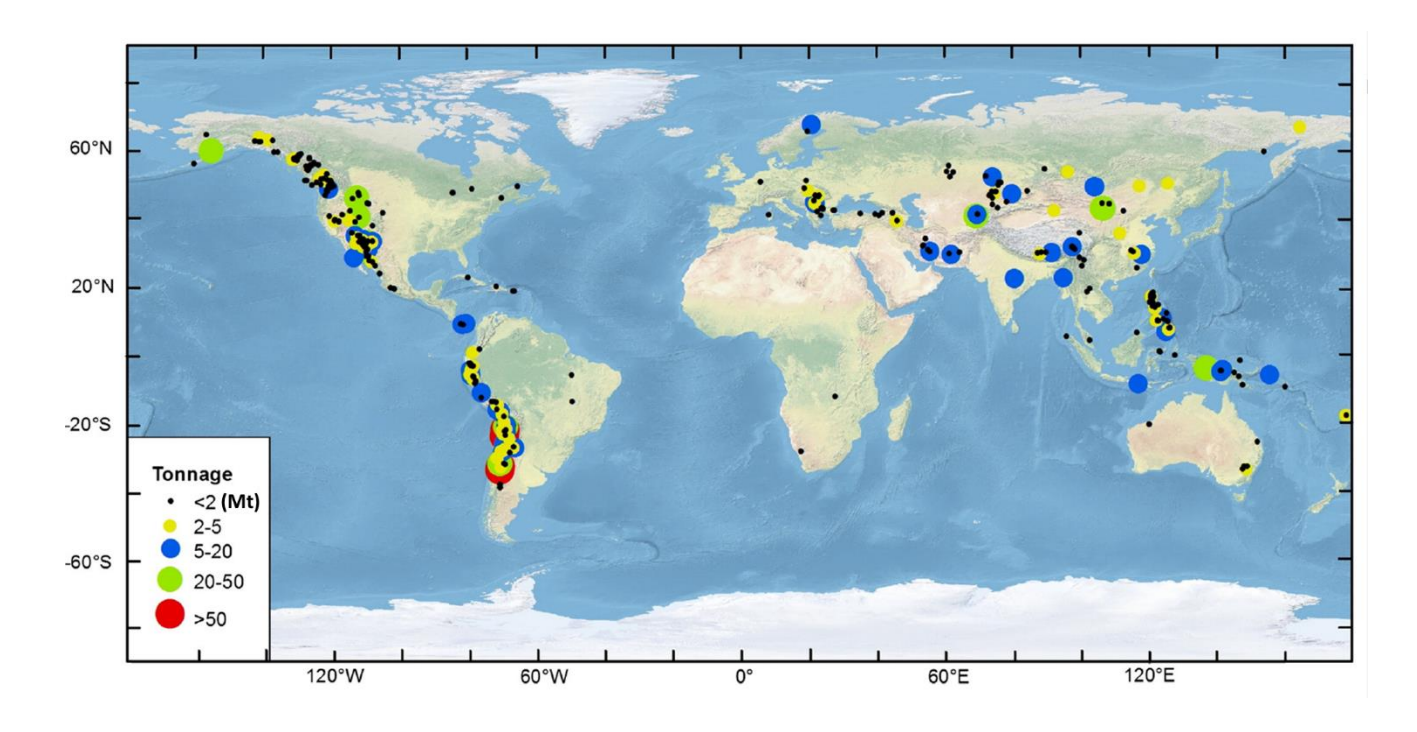


Figure 1.1. Global distribution of porphyry deposits. Most of the porphyry Cu deposits occur along convergent margins. Modified after Sun et al. (2013) and Mutschler et al. (2010).

The Saddle North Cu-Au porphyry deposit in northwestern British Columbia (Fig. 1.2) has characteristics of both alkalic and calc-alkalic deposits (Micko, 2014; GT Gold, 2020). Many features of Saddle North are similar to porphyry deposits in the Iskut district of northwestern British Columbia, such as Red Chris and Galore Creek, as part of a geologically significant region recognized for its exceptional endowment of precious metal deposits (Rosset, 2015; Tombe, 2019; Lawley, 2025). Saddle North has high-grade ore (> 1% Cu and 1 g/t Au) present to depth in two of the four mineralized centers characterized by pervasive K-feldspar alteration and veins preserved in the central part of the system (http://www.gtgoldcorp.ca GT Gold, 2020).

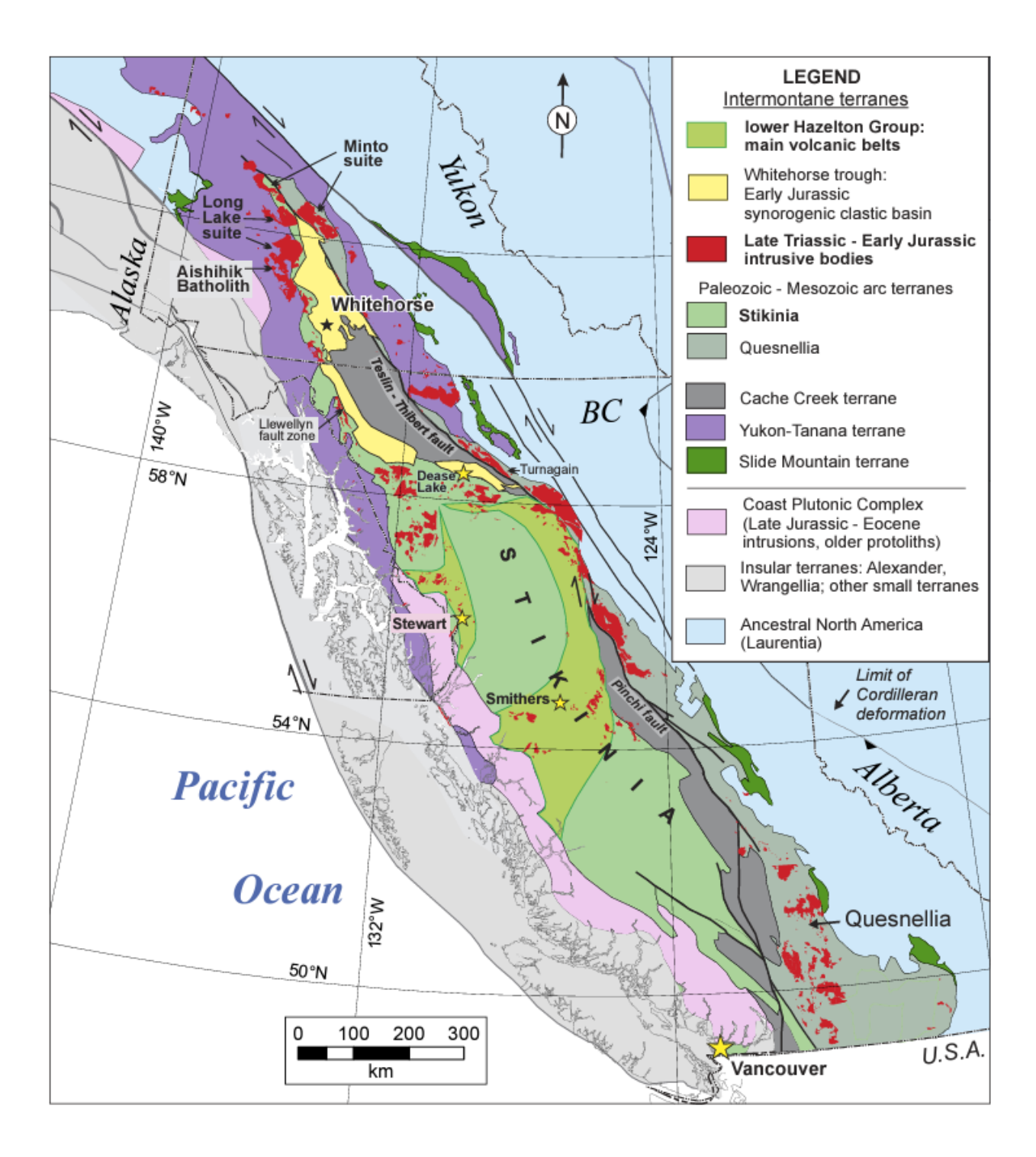


Figure 1.2. Terrane map of the Canadian Cordillera Triassic–Jurassic assemblages of Stikinia. British Columbia. From Logan and Milhanyuk (2014).

This research is part of a broader collaboration between the Mineral Deposit Research Unit (MDRU) at the University of British Columbia (UBC), Lakehead University and Newmont Mining Corporation, supported by 15 industry partners and an NSERC Alliance grant. The larger project aims to advance the understanding of porphyry deposit formation, magmatic history, and the paragenetic relationships between mineralization and alteration processes in British Columbia. Specifically, this study focuses on the geology, alteration, and mineralization of the Saddle North porphyry deposit to refine interpretations of alteration assemblages and mineral chemistry. Advances in lithogeochemistry, magmatic mineral analysis, and mineral chemistry techniques over the last 15 years have significantly improved the ability to identify fertile porphyry systems and determine their proximity and direction (Wilkinson et al., 2015; Cooke et al., 2020; Layton-Matthews & McClenaghan, 2021), leading to better understanding of porphyry system evolution, hydrothermal alteration, and more precise characterization of mineralization, improving the correlation between hydrothermal pulses and intrusive events.

1.1. Objectives

The primary objective of this research was to investigate the magmatic paragenesis of the Saddle North porphyry system and characterize the alteration assemblages in the porphyry environment by integrating the geology and hydrothermal alteration assemblages, using drill core samples from a vertical section through the dominant ore-bearing zone. A secondary but complementary objective of this study was to identify the temporal the relationship between alteration and mineralization using a combination of whole-rock geochemical data with high-precision U-Pb zircon and Re-Os molybdenite geochronology.

1.2. Study Location

The Tatogga property and Saddle North Project are located in the Stikine River region of the northwestern margin of the Stikine terrane in British Columbia, Canada (Fig. 1.3). The deposit is situated one kilometer east of the village of Iskut on Highway 37. It is hosted within the island arc component of the Stikine Terrane and the Lower to Upper Triassic Stuhini Group (Nelson et al., 2013), a series of distinct alkalienriched volcanic arcs and volcanogenic sedimentary rocks of mid-Paleozoic to mid-Mesozoic age that includes alkalic intrusive rocks that host porphyry Cu-Au deposits (Logan, 2005; Schwab et al., 2008). The study area is located within the steepest Stikine region, making access to portions of the property area difficult. Drill core is currently stored in a core yard storage located 20 Km NE of Terrace, British Columbia.

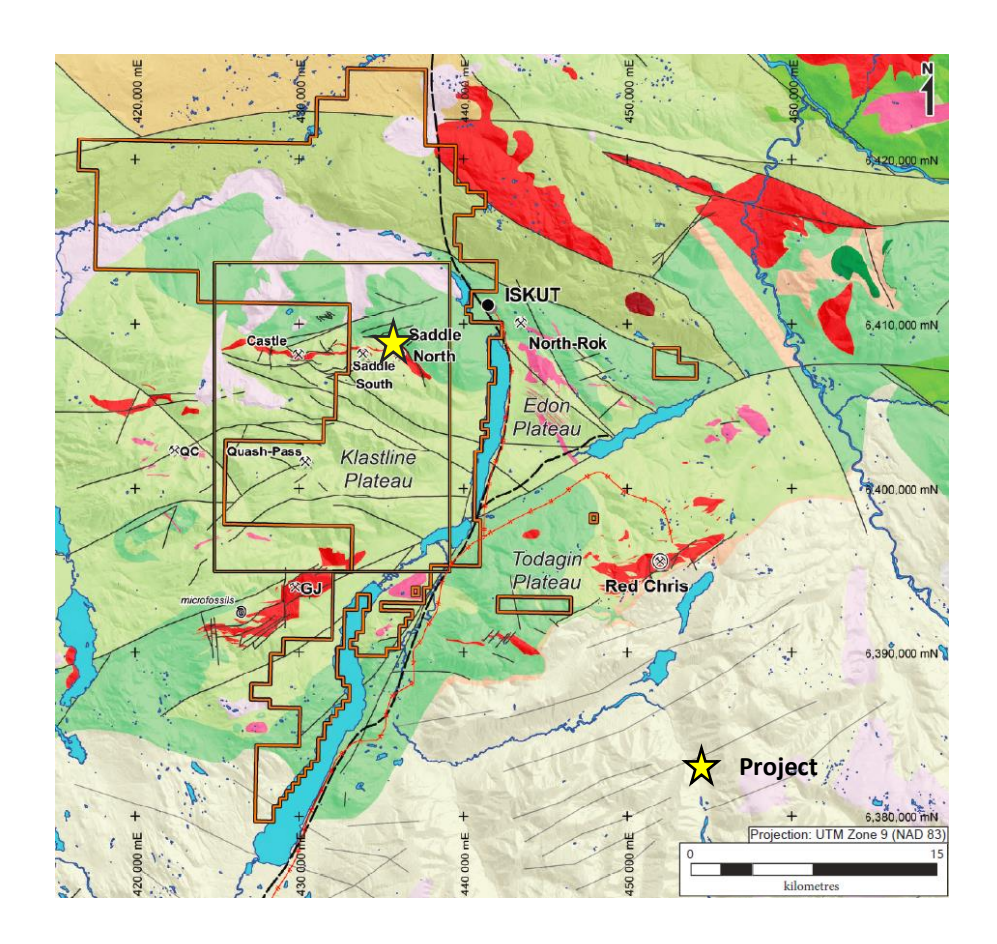


Figure 1.3. Geology of the Tatogga property, Saddle North Project location. Modified from Greig (2020).

Chapter 2. Regional Geology

The northern Cordilleran in western Canada comprises rocks from the Laurentian continental core to more recent rocks related to subduction and transform motion along the west coast of North America (Nelson et al., 2013). The orogeny formed due to the docking of at least two allochthonous terranes to the western margin of the North American continent (Monger et al., 1972). According to Nelson et al. (2013), the northern Cordillera consists of multiple terranes subdivided into first-order tectonic blocks: 1) Ancestral North America (Laurentia); 2) the allochthonous marginal pericratonic terranes (Intermontane terranes); 3) the exotic Insular and Farewell terranes; 4) Arctic Alaska; and 5) Mesozoic and younger arc and accretionary terranes (Fig. 2.1, red dashed line refers to the peri-Laurentian realm). The ancient Laurentian continent consists of 2.3 to 1.8 Ga cratonic basement, that is characterized by Proterozoic intra-cratonic basin subsidence and Paleozoic episodic spreading of the seafloor and the development of a long-lived passive margin that continued through the construction of Paleozoic and younger intraoceanic and continent-margin arcs through the Mesozoic (Nelson et al., 2013). The Tatogga Lake terrane extends along the Pacific margin of the North American Cordilleran (Fig. 2.2). It comprises volcanic arcs that were accreted to the edge of North America. In the Canadian Cordillera's central region (Fig. 2.2), the majority of the porphyry deposits occur in two specific arc terranes; Quesnellia which consists of Paleozoic (Devonian to Permian) sedimentary rocks that suggest a continental-margin-related sedimentary succession for at least part of the region (Monger et al., 1991; Erdmer et al., 2001a, 2001b), and Stikinia which is an oceanic island arc that was accreted to the western margin of North America by the late Middle Jurassic to form the Intermontane Belt of the Canadian Cordillera (Coney et al., 1980; Monger et al., 1982; Nelson and Colpron, 2007 and Logan, 2014).

The Stikine terrane is described by Alldrick (2004) as a series of five mid-Paleozoic to mid-Mesozoic volcanic arcs with two lulls in volcanism corresponding with tectonic uplift at the Triassic-Jurassic

boundary and in the Lower Jurassic, which are overlain by mid-Jurassic through mid-Cretaceous strata of the Bowser basin (Souther, 1972). The study area is located within the Stikine arc, part of the Stikine terrane composed of mafic to felsic, arc-related volcanic and clastic rocks (Fig. 2.3), underlain by Mesozoic volcanic and associated volcanoclastic and sedimentary rocks consisting of the Middle to Upper Triassic Stuhini Group, the Lower Jurassic Hazelton Group, and the Middle and Upper Jurassic to Lower Cretaceous Bowser Lake Group (Fig. 2.4; Monger et al., 1991; Ash et al., 1996).

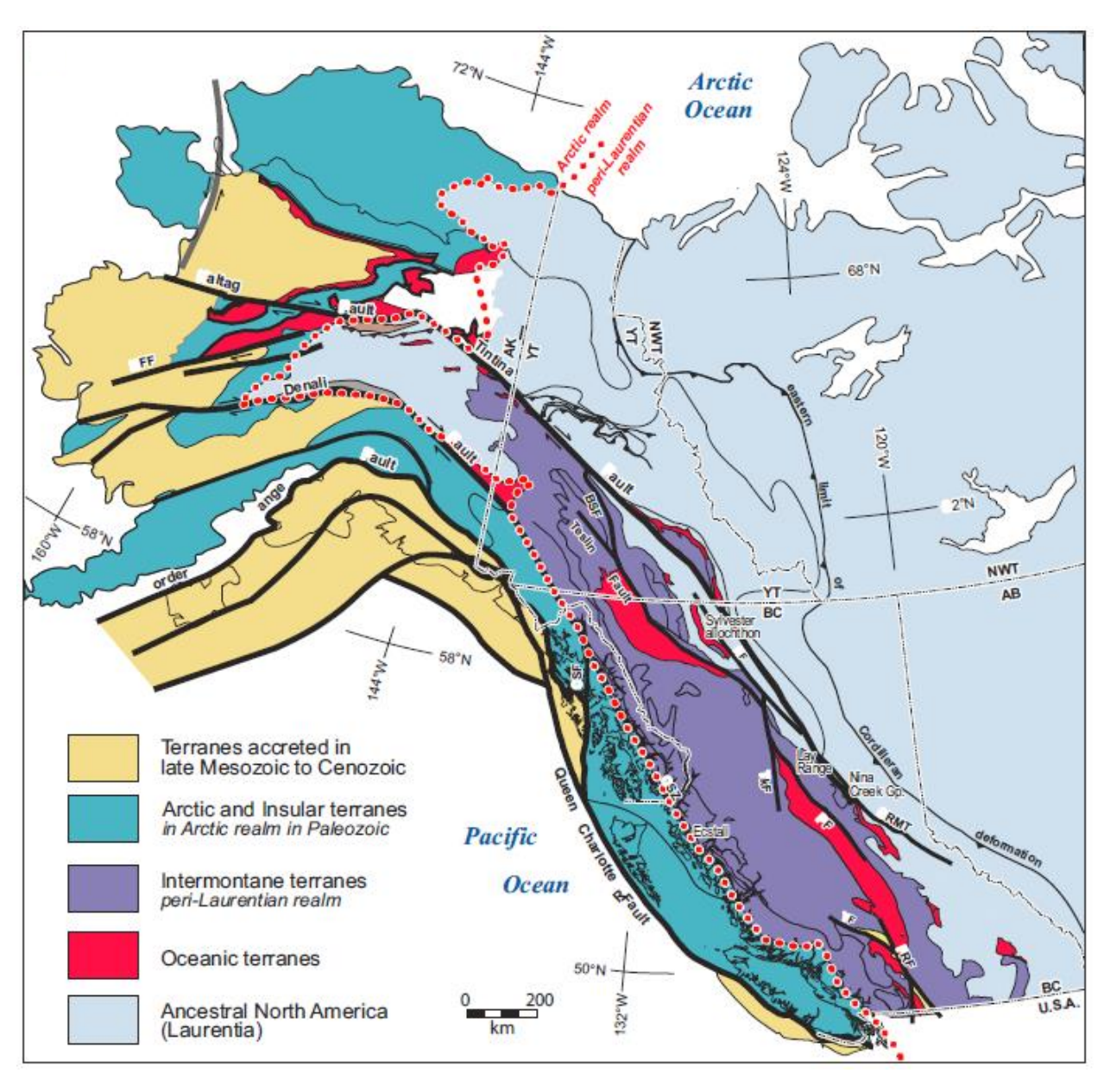


Figure 2.1. Tectonic realms of the Canadian-Alaskan Cordillera. From Nelson (2013).

The Canadian Cordillera hosts several porphyry deposits in the Late Triassic and Early Jurassic Quesnellia and Stikine Terranes, formed from a single marine island arc that experienced oroclinal bending accompanied by progressive amalgamation to North America in the Early Jurassic (Mihalynuk et al., 1994; Colpron et al., 2007; Nelson, 2007; and Micko, 2014). Two principal stratigraphic groups have been identified in these terranes: The Middle and Upper Triassic rocks of the Stuhini Group and the Lower and Middle Jurassic volcanic and clastic rocks of the Hazelton Group. These are associated with multiple intrusive events including: (1) Late Triassic calc-alkaline plutonic complexes associated with porphyry Cu-Mo (± Au) deposits, (2) Late Triassic alkalic diorite to monzonitic intrusive complexes associated with porphyry Cu-Au deposits (Fig. 2.2), and (3) Middle Jurassic alkali and calc-alkalic intrusive complex associated with porphyry Au-Cu deposits (Febbo, 2019). These events can generate multifaceted overprints of alteration and mineralization assemblages (Barr et al., 1976; Lang et al., 1995a; Mortensen et al., 1995; Logan, 2005; Scott et al., 2008; Logan & Mihalynuk, 2014; Pass et al., 2014; and Micko, 2014).

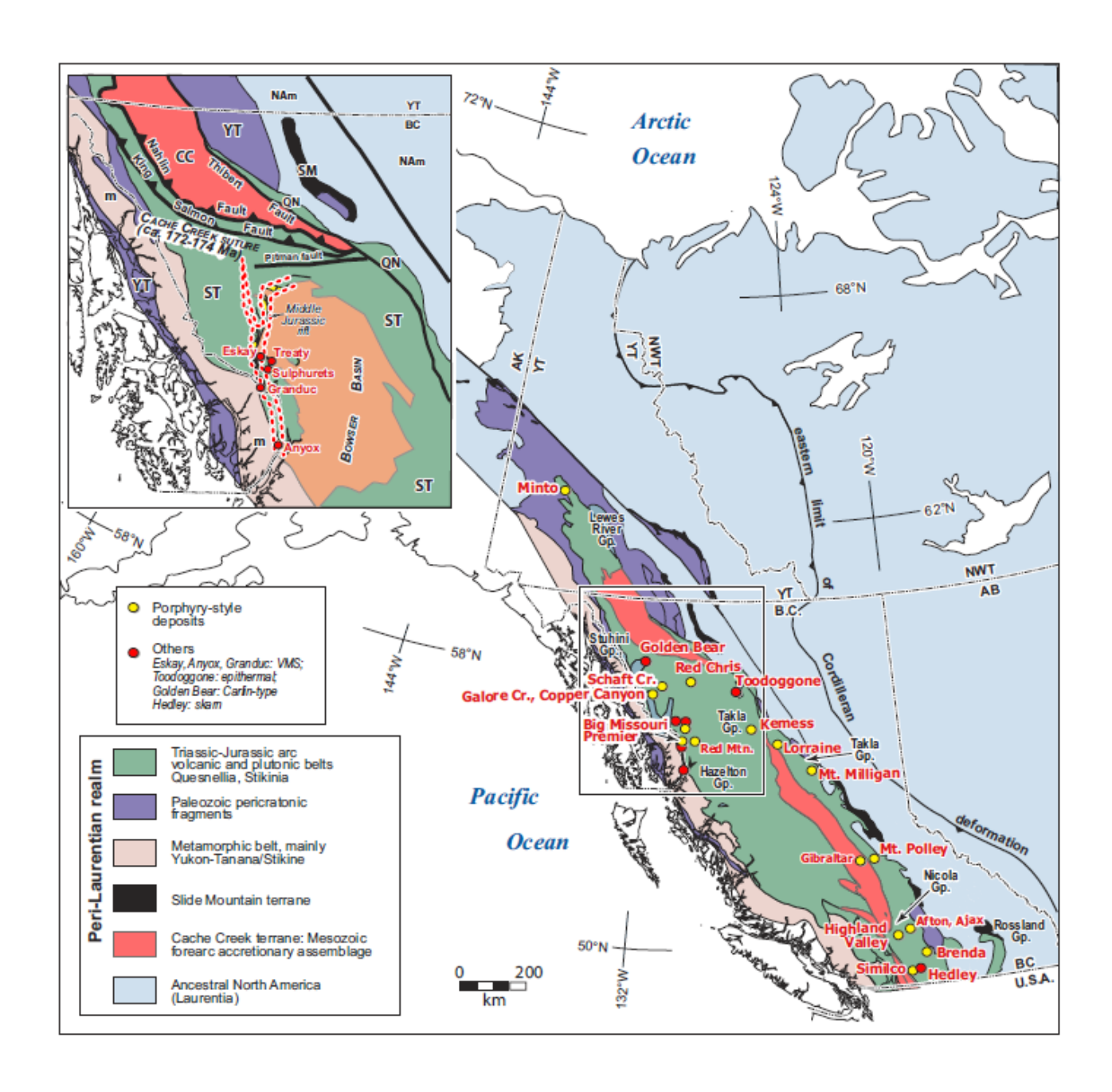


Figure 2.2. Triassic to Middle Jurassic magmatic belts and associated deposits of the Intermontane terranes (from Nelson, 2013).

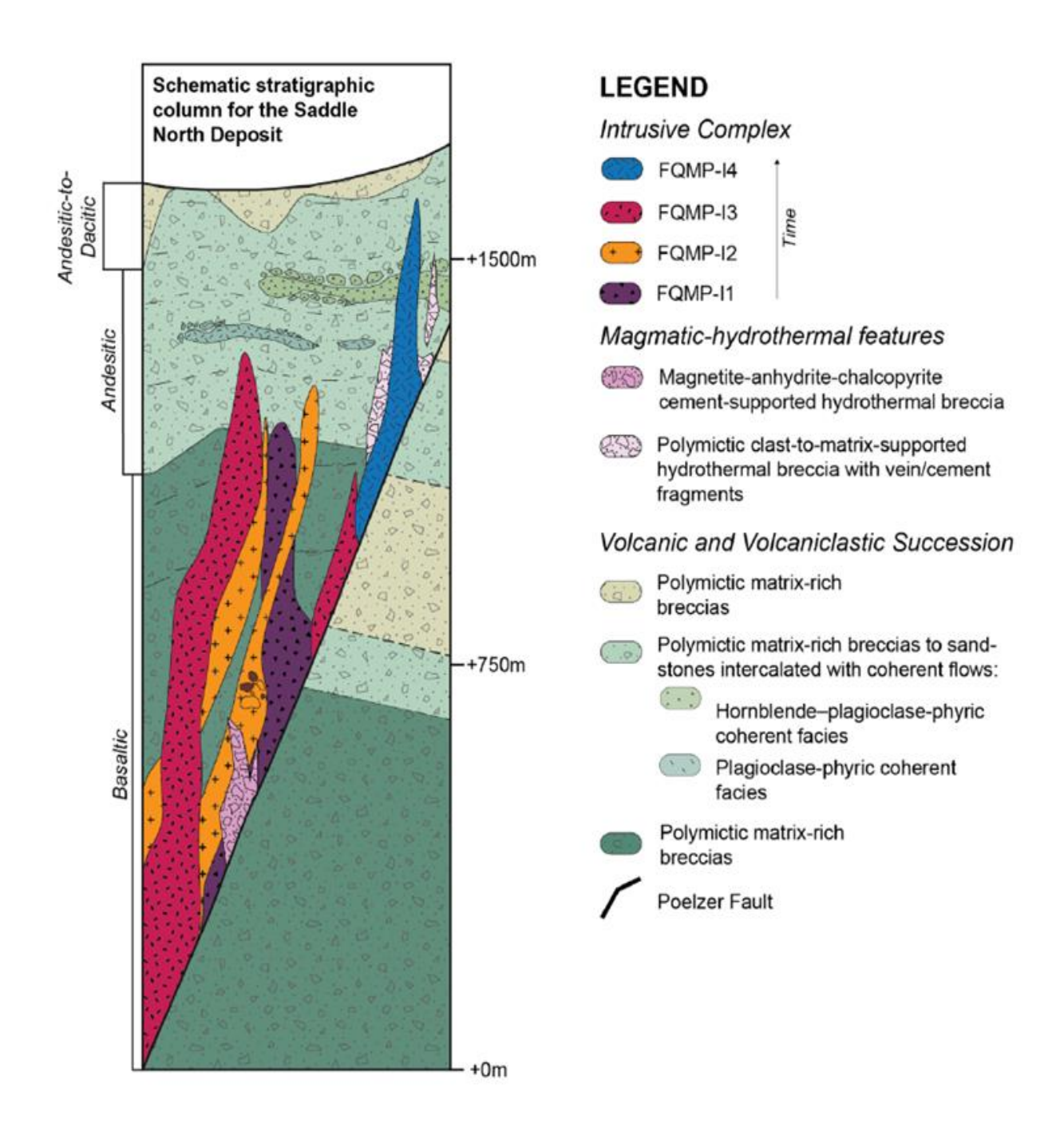


Figure 2.3. Schematic cross-section across the Saddle North mineralized zones of the Tatogga property. Modified from Geology, Au-Cu mineralization, hydrothermal alteration and structural features | Saddle North Rock Atlas internal report. Courtesy of Newmont's Saddle Exploration team.

The geology of the study area has been described by Miller and Smythe (2015). The Saddle North copper porphyry system is hosted in polyphase dioritic to monzodioritic intrusive rocks (G.T. Gold, 2020). The host rock consists of metamorphosed sedimentary and volcanic rocks ranging from the Early Devonian to the mid-Permian in age (Fig. 2.3). The host rocks include foliated mafic and felsic metavolcanic rocks, argillite, limestone, and layered marble (Ash et al., 1996). Stuhini Group rocks underly the host rocks in the southern parts, Hazelton Group rocks in the north, and local Tertiary volcanic rocks overlying both units in the study area's southern, western, and northern margins (Nelson, 2018; Figs. 2.3 and 2.4). Miller and Smythe (2015) described at least two generations of felsic dykes cutting lithologies of both the Hazelton and Stuhini Group rocks with an older strongly flow-folded, locally vesicular and largely aphyric variety and a younger second set of rhyolite dykes, characterized by a distinctive pink color and containing quartz eye phenocrysts sometimes with by feldspar phenocrysts (G.T. Gold, 2020; Fig. 2.5). Miller and Smythe (2015) defined the Stuhini Group rocks in the study area as predominantly finely laminated to meter-scale very fine-grained bedded sandstone and shale, occurring in altered carbonate-rich volcanic and epiclastic sequences with minor pyroxene-bearing basalt. The Stuhini Group is deformed with folds at various scales, possibly associated with thrust faults (Miller & Smythe, 2015).

Miller and Smythe (2015) identified and described three distinct lithological units within the Hazelton Group in the study area, each characterized by unique sedimentary or volcanic features. The first unit comprises medium- to coarse-grained sandstone, texturally and compositionally similar to sedimentary rocks of the underlying Stuhini Group. However, it can be distinguished by the presence of localized quartz veinlets, suggesting minor hydrothermal overprinting or syn- to post-depositional fluid activity. The second unit is a polymictic conglomerate and/or volcanic breccia, characterized by a clast-supported texture with subangular to well-rounded fragments. These clasts are predominantly composed of crowded feldspar porphyry, indicative of proximal volcanic or hypabyssal sources, and are hosted in a feldspathic matrix with subordinate maroon mudstone fragments. The nature and composition of this

unit suggest deposition in a volcaniclastic apron or syn-volcanic debris flow environment. The third and least abundant unit consists of rare, pillowed basalt flows, displaying pyroxene-phyric textures and pillow structures indicative of subaqueous extrusion. These basalts are mafic in composition and point to intermittent submarine volcanic activity during Hazelton Group deposition.

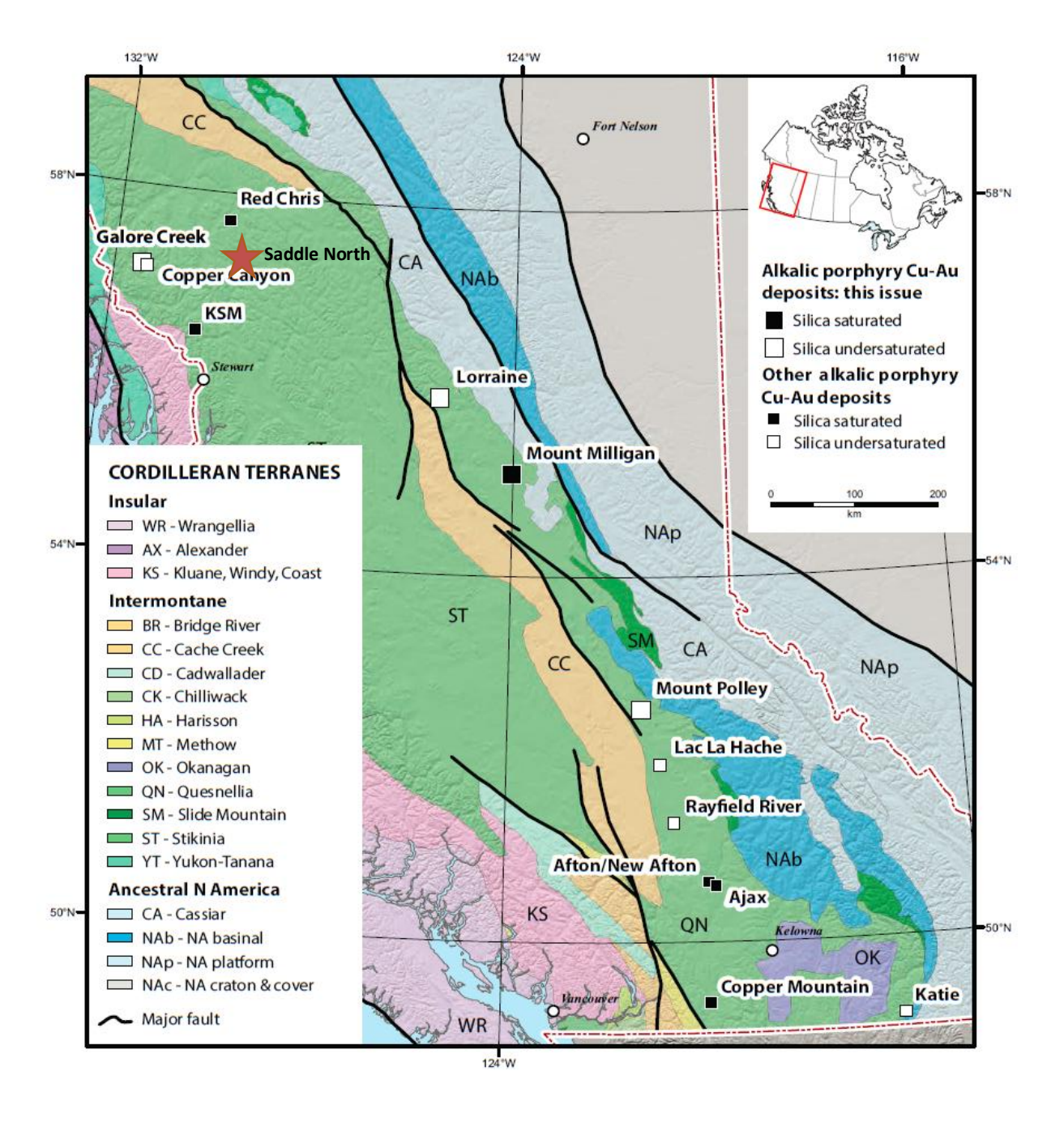


Figure 2.4. Terrane map and location of selected alkalic porphyry Cu-Au deposits of British Columbia. From Bissig & Cooke (2014).

Importantly, Miller and Smythe (2015) emphasized the close compositional and textural similarities between the Hazelton and Stuhini Groups, which pose significant challenges in delineating a clear stratigraphic contact between the two formations. This complexity underscores the tectonostratigraphic intricacies of the Stikine Terrane, where overlapping depositional environments and similar lithofacies reflect a dynamic arc-related setting during the Triassic to Early Jurassic transition (Fig. 2.5). They noted that the main difference between the two units was the presence or absence of quartz veins in the sandstones and the occurrence of maroon mudstone and hornblende-phyric fragments in the Hazelton conglomerates/breccias (Miller and Smythe, 2015). The Hazelton Group and the Stuhini Group are arcs that comprise a succession of clastic sedimentary rocks with lesser mafic volcanic and related epiclastic rocks. Both the Hazelton and Stuhini groups are locally intercalated with bimodal intermediate volcanic and volcanoclastic rocks, dominated by porphyritic basaltic flows that appear at the base, overlain by breccias and capped by fine-grained clastic sedimentary rocks ranging from siltstones to mudstones, volcanic sandstones, and minor carbonates (Fig. 2.5; Ash et al., 1996; Alldrick, 2004).

This stratigraphic sequence is predominantly underlain by sedimentary units of the Middle Jurassic to Lower Cretaceous Bowser Lake Group (Ash et al., 1996; Evenchick et al., 2007), which records a complex geological history involving arc-related magmatism, clastic sedimentation, and subsequent deformation. These processes reflect the prolonged tectonic evolution associated with accretionary events along the western margin of ancestral North America (Marsden & Thorkelson, 1992; Nelson et al., 2018). The Bowser Lake Group is locally faulted against, and in some areas structurally overlies, older metasedimentary and metavolcanic rocks of the Paleozoic Stikine Assemblage. The latter is composed of a heterogeneous belt of Early Devonian to mid-Permian deformed and foliated lithologies, including phyllitic mafic and felsic metavolcanic rocks, argillite, massive limestone, and banded marble (Ash et al., 1996). These units represent the basement to the overlying Mesozoic arc sequences and preserve evidence of early arc magmatism and marine sedimentation predating Mesozoic terrane amalgamation.

Regionally, these Paleozoic and Mesozoic successions are intruded by a suite of intermediate to felsic plutonic rocks forming part of an extensive east-west trending belt of mineralized intrusions. Locally referred to as the Saddle intrusions, this belt hosts the Saddle North porphyry copper-gold system. Mineralization at Saddle North is primarily associated with a multiphase intrusive complex collectively termed the Saddle North intrusive complex, which comprises a series of compositionally similar monzonitic to monzodioritic intrusions emplaced during the latest Triassic to earliest Jurassic (Greig, 2021). These intrusive rocks serve as both the source and conduit for the hydrothermal fluids responsible for porphyry-style Cu-Au ± Mo mineralization, and their emplacement is temporally and spatially linked to regional tectonomagmatic activity associated with subduction-related arc construction in the Stikine Terrane.

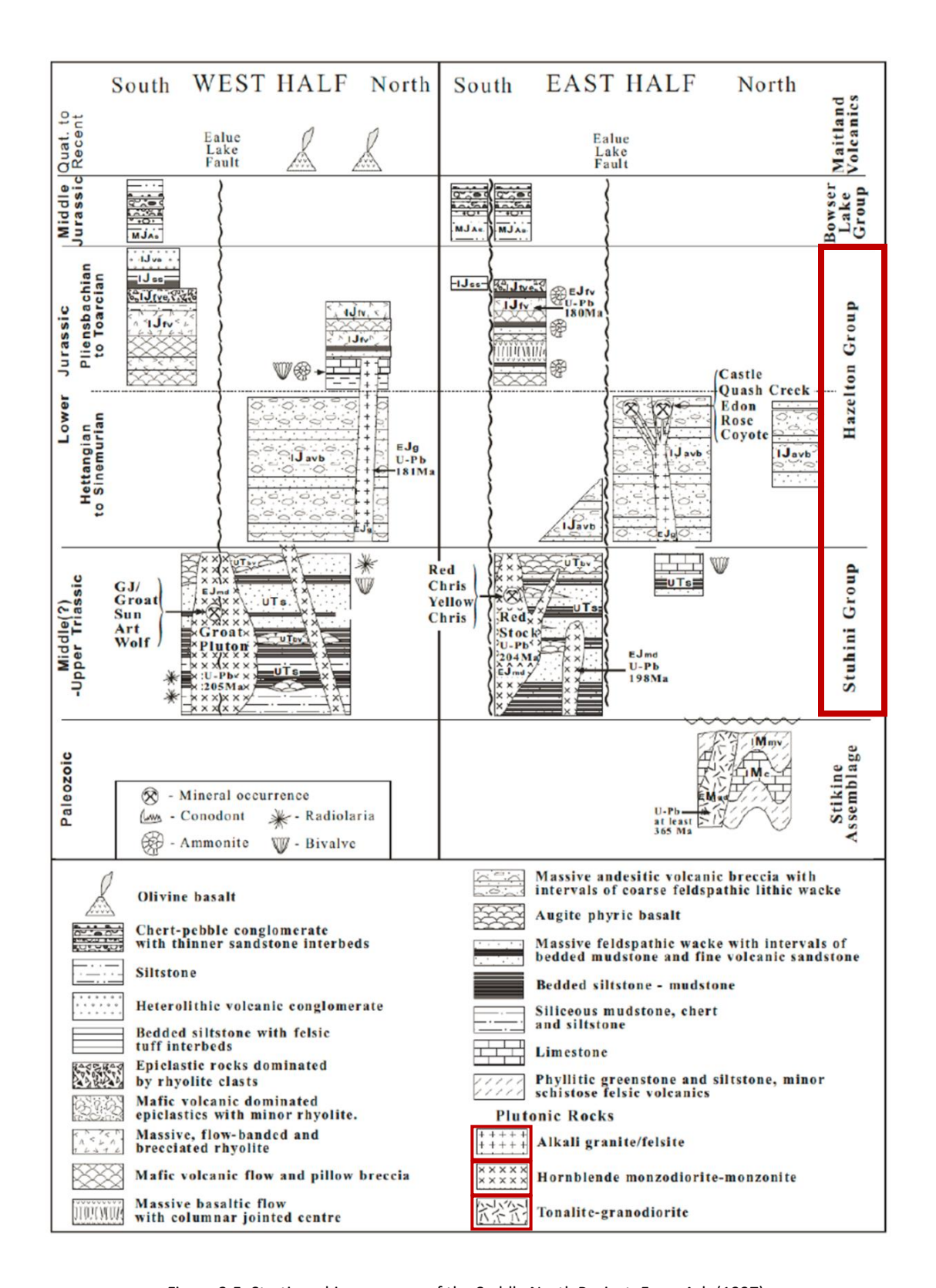


Figure 2.5. Stratigraphic sequence of the Saddle North Project. From Ash (1997).

The Saddle North project is a gold-rich — copper porphyry hosted in monzodiorite and monzonite intrusions emplaced into Stuhini Group volcanic and local volcanoclastic rocks, which are in turn unconformably overlain by rocks of the Hazelton Group (Fig. 2.5). The Intrusive contacts are generally transitional rather than sharp (43-101 Technical Report G.T. Gold, 2020). The intrusive complex is interpreted to be a series of igneous bodies that intruded volcanic rocks of the Stuhini Group over a short period during which local co-mingling and intrusive brecciation occurred (Stanley, 2021). Different porphyry alteration events of varying intensity have overprinted the intrusive lithologies (Fig. 2.6). Minor post-mineralization felsic and mafic dykes are also present (Fig. 2.5; G.T. Gold, 2020). Six alteration styles have been recognized in the monzonite to monzodiorite intrusion (43-101 Technical Report G.T. Gold, 2020): potassic, quartz-sericite-pyrite (QSP), chlorite sericite, weak to trace intermediate-argillic, and propylitic alteration (Fig. 2.5; G.T. Gold, 2020).

Geochronology of multiple intrusive phases within the footwall mineralization and ore-bearing zones indicates that the Late Triassic to Early Jurassic magmatic center was primarily active between approximately 206 and 202 Ma, broadly contemporaneous with other Late Triassic porphyry deposits situated in northern Stikinia, within the Canadian Cordillera (Mortensen, 1995; Ash et al., 1996; Greig, 2021). To further constrain the timing of mineralization, Re–Os dating of molybdenite extracted from calcite–quartz–chalcopyrite–pyrite veins—occasionally containing minor molybdenite and hosted within potassic-altered phases of the Saddle North intrusive complex—yielded ages between 204.2 ± 0.9 Ma and 207.8 ± 0.9 Ma (Greig, 2021). These results are not only internally consistent, but also align with the depositional age of the Stuhini Group stratigraphy. Together, these ages establish a geochronological framework that places the magmatic activity, vein formation, and associated mineralization at Saddle North firmly within the Late Triassic–Early Jurassic transition (~207–202 Ma), contemporaneous with regional porphyry copper systems across the Stikine Terrane. As of August 2020, the Saddle North Copper Gold Project had an indicated mineral resources of 298 Mt grading 0.28% Cu, 0.36 g/t Au, and 0.8 g/t Ag,

and an inferred mineral resource of 543 Mt grading 0.25% Cu, 0.31 g/t Au, and 0.7 g/t Ag (GT Gold Corporation Ltd., 2020).

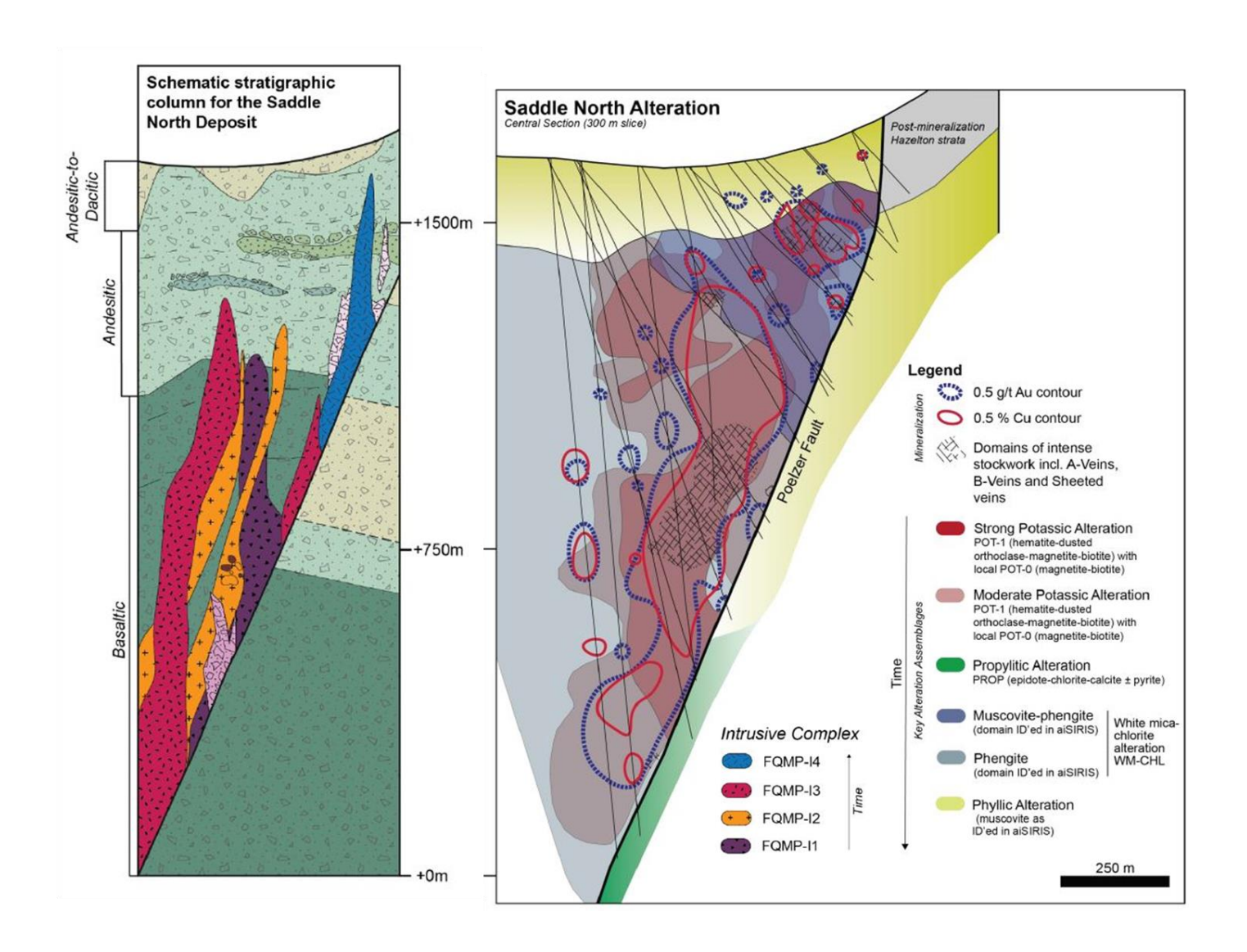


Figure 2.6. Schematic alteration and mineralization at Saddle North, intrusive feldspar-quartz-monzodiorite porphyry complex (Intrusive FQMP Complex). Modified from Geology, Au-Cu mineralization, hydrothermal alteration and structural features Saddle North Rock Atlas internal report. Courtesy of Newmont's Saddle Exploration team.

Chapter 3. Methodology

3.1. Sample Collection

Sampling was conducted in Terrace, British Columbia, at the Newmont core storage facility core for a week in mid-June 2023. A total of 102 samples from five drill holes (TTD093, TTD106, TTD109, TTD128, and TTD134; Fig. 3.1) were collected. Emphasis was placed on identifying the different intrusions and constraining cross-cutting relationships.

3.2. Whole-rock geochemistry

Thirty-five (35) whole-rock samples were collected from unaltered, altered, and mineralized units to study the geochemistry. They were prepared for major, trace, and rare earth elements analysis at ALS Minerals Laboratories in Vancouver, BC. The sample preparation process involved standard procedures such as drying, crushing, splitting, and pulverizing. The selected samples were analyzed by inductively coupled plasma-mass spectrometry (ICP-MS), inductively coupled plasma-atomic emission spectroscopy (ICP-AES), and X-ray fluorescence (XRF) to determine the elements present in the rocks, for the major rock-forming elements were analyzed by both X-Ray fluorescence and inductively-coupled atomic emission spectrometry (XRF, and ICP-AES, ALS method ME_XRF26), followed by measurement on a fused disc and extra digestion dissolution. Trace elements were analyzed by inductively coupled plasma mass spectrometry (ICP-MS, ALS method ME-MS81) after lithium borate fusion and four-acid digestion dissolution (more details; www.alschemex.com).

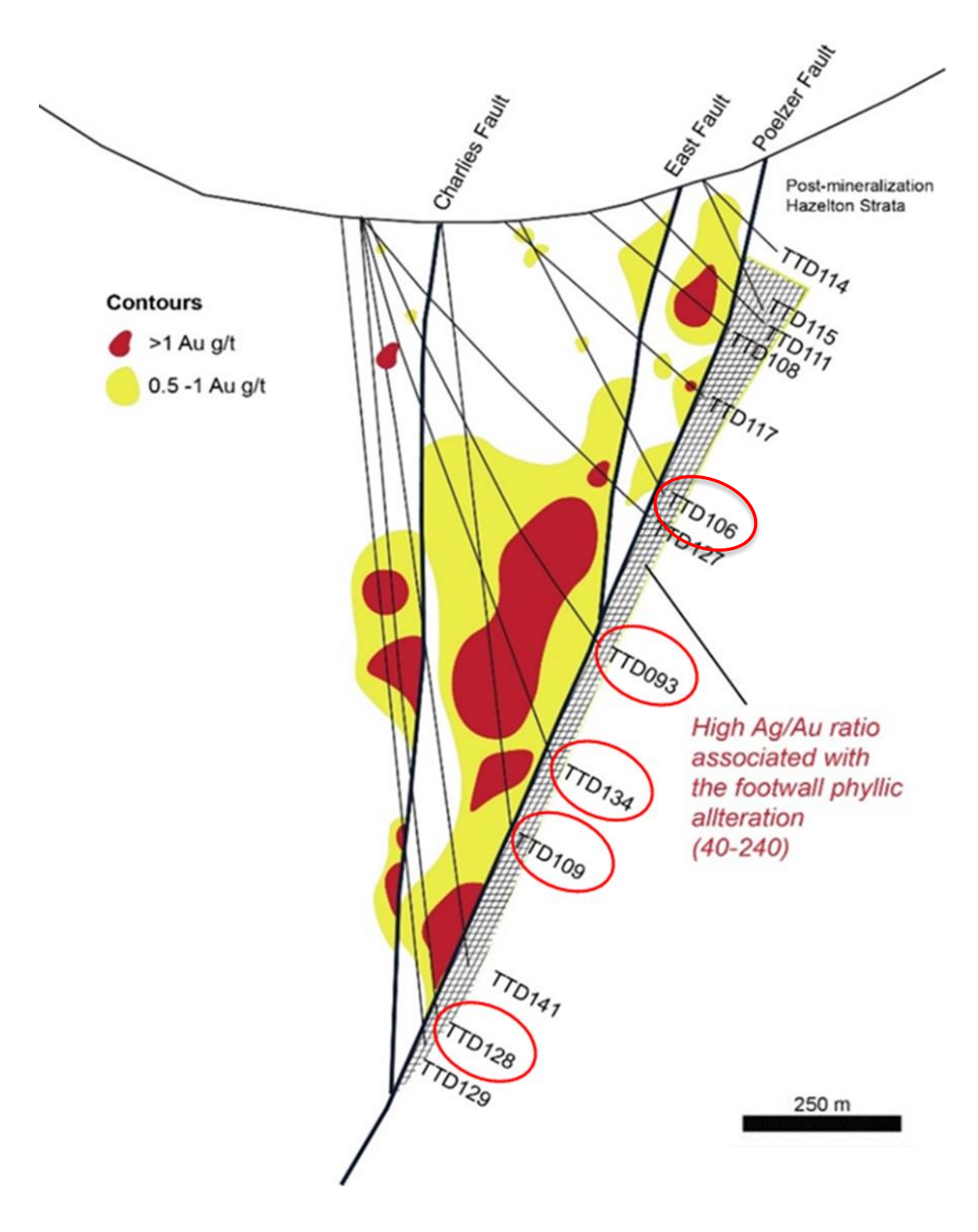


Figure 3.1. Drill hole locations. Modified from Geology, Au-Cu mineralization, hydrothermal alteration and structural features | Saddle North Rock Atlas internal report. Image courtesy of Newmont's Saddle Exploration team.

3.3. Petrography

Thin-sections were prepared at Lakehead University and subsequently described under transmitted and reflected light. Photomicrographs were acquired using an Olympus SC180 camera mounted on an Olympus Bx51 microscope. A total of eighteen (18) thin sections of key samples were selected from the Saddle North Gold Deposit.

3.4. Micro-XRF

Micro-XRF data were collected from whole rock samples and scanned at the University of British Columbia in partnership with MDRU (Mineral Deposit Research Unit), producing two-dimensional maps of XRF spectra that capture the spatial disparity of elemental composition and mineralogy using a Bruker Tornado μXRF scanner on split drill core samples at a spatial resolution (10 ms/pixel) of approximately 100 μm size producing X-ray spot sizes between 20–30 μm (Bruker, 2018). This technique combined quantification methods with fundamental parameters (FP). The micro-XRF method estimates element concentrations by modelling X-ray interactions within the sample and accounting for matrix effects such as absorption and enhancement (Elam et al., 2004; Flude, 2017). Furthermore, the method facilitates a detailed understanding of hydrothermal alteration patterns critical for assessing mineralization processes in porphyry gold deposits, as it allows for the spatial distribution of key alteration minerals to be visualized at a drill core scale (Barker, 2020). For this study, the samples were quantified in the μXRF maps for Al, Zr, Ca, Fe, K, Mg, Mn, P, S, Si, and Ti, elemental composition abundance.

3.5. Geochronology (LA-ICPMS)

Zircon grains were separated from 10 samples of the monzonite and monzodiorite porphyry for zircon U-Pb geochronology at the University of British Columbia. The detailed methods are described by Tafti et al.

(2009). Laser ablation-inductively coupled plasma-mass spectrometry (LA-ICP-MS) U–Pb zircon geochronology has been applied widely to in situ zircon dating. All zircons were assessed by transmitted and reflected light photomicrographs as well as with cathodoluminescence imaging to identify their internal structures and select spots for LA-ICP-MS U-Pb analyses. Dated zircon 91500 y LA-ICP-MS using a spot size of 35-125 μm and measured ²⁰⁷Pb/ ²⁰⁶Pb, ²⁰⁶Pb/ ²³⁸U, and ²⁰⁸Pb/ ²³²Th ratios were the external standard for the zircon U–Pb dating to correct depth-dependent elemental and isotopic fractionation and instrumental mass bias during analysis (Wiedenbeck et al., 1995 & Yuan, 2004).

3.6. Re-Os Geochronology

A sample of quartz–molybdenite ± pyrite vein was sent to the University of Alberta for Re-Os geochronology. Detailed methods used for molybdenite geochronology are described in detail by Selby and Creaser (2004). The samples were processed by metal-free milling and grinding, followed by density and magnetic separation to produce a molybdenite concentrate. The ¹⁸⁷Re and ¹⁸⁷Os concentrations in molybdenite were determined by isotope dilution mass spectrometry using Carius-tube, solvent extraction, anion chromatography, and negative thermal ionization mass spectrometry techniques. A mixed double spike containing known amounts of isotopically enriched ¹⁸⁵Re, ¹⁹⁰Os, and ¹⁸⁸Os was used. Isotopic analysis was completed using a Micromass Sector 54 mass spectrometer with a Faraday collector. Total procedural blanks for Re and Os are less than <3 picograms and 2 picograms, respectively, which are insignificant for the Re and Os concentrations in molybdenite.

Chapter 4. Results

4.1. Petrography

The Intrusive complex in the Saddle North area consists primarily of monzonite and monzodiorite rocks composed of plagioclase, orthoclase, and lesser amounts of quartz, biotite, and amphibole. Typically, the rocks exhibit a hypidiomorphic granular texture, where individual mineral grains are distinct but lack well-developed crystal faces (grain sizes used were very fine (<0.1 to 0.01 mm), fine (0.1 to 1mm), medium (1 to 3 mm) and coarse-grained (>3 mm)). Porphyries from the Saddle North area contain phenocrysts of mainly euhedral tabular plagioclase (0.4–3 mm), with lesser amounts of euhedral to subhedral bladed hornblende, tabular K-feldspar, biotite and small amounts of quartz, with strong quartz-feldspar alteration associated with the mineralization (Fig. 4.1). The groundmass is composed of fine-grained and granular quartz, oligoclase and K-feldspar, with minor hornblende and biotite. Porphyritic volcanic and volcanoclastic units are composed of abundant, very fine-grained plagioclase-phyric andesite and diorite with euhedral greyish-white plagioclase up to 2 cm long enclosed in a massive, fine-grained groundmass of dark grey plagioclase, quartz, and amphibole that is variably altered to sericite, chlorite and minor calcite. Most of the intermediate volcanic rocks have undergone strong quartz-sericite alteration (alteration intensities weak (0 to 30%), moderate (31 to 60%) and strong (61 to 100%)).

Four distinct intrusive porphyry phases were distinguished using petrographic and hand specimen criteria according to mineralogical variations, content (modal percentages based on visual estimates), and alteration intensity. Based on those differences the intrusions were divided into sub-phases but the original FQMP terminology proposed by Newmont has been retained for clarity. The first intrusive phase is a quartz monzonite-diorite porphyry with anhedral to subhedral phenocrysts dominated by plagioclase (60% sericitized), mafic minerals such as hornblende and biotite (10%), and K-feldspar (40%) with a

groundmass of K-feldspar and rare to absent quartz (Fig. 4.1; FQMP-I1). The second phase consists of plagioclase (55%-60%), mostly sericitized, hornblende and biotite (10%-15%), and 25% K-feldspar phenocrysts in a fine-grained quartz-plagioclase-hornblende groundmass that is weakly to strongly magnetic (measured on the core with pencil magnet; Fig. 4.1; FQMP-I2). The third phase is a monzonite porphyry that is comprised of euhedral to subhedral hornblende-biotite (15-20%) and sericitized plagioclase (55-60%), with microcrystalline (35%) K-feldspar and lesser (3%) quartz in the groundmass (Fig. 4.1, FQMP-I3). The fourth phase is characterized by lower phenocryss contents of tabular plagioclase (60%) and tabular K-feldspar (34%), with hornblende and biotite (10%) similar to the first phase but with less intense K-feldspar alteration (Fig. 4.1; FQMP-I4). Secondary minerals include clay, chlorite, sericite, calcite, muscovite, and epidote, and all samples show varying degrees of alteration intensities (weak to strong mostly K-feldspar) decreasing through the intrusive stages with distinct veining styles.

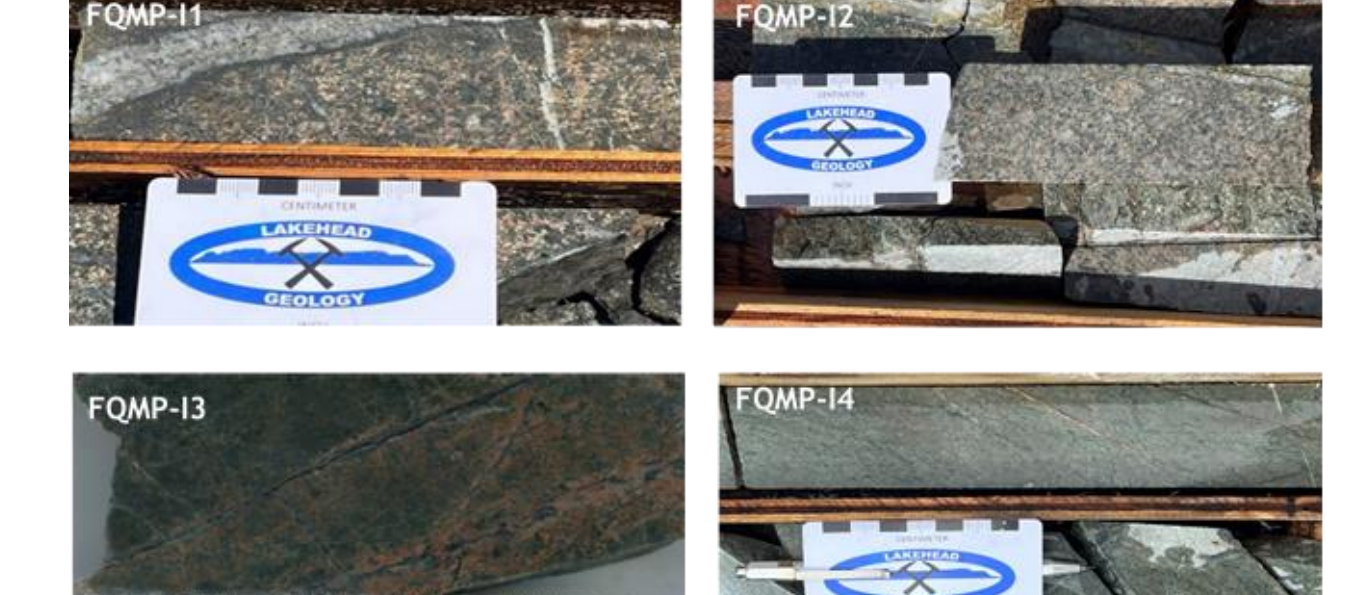


Figure 4.1. A. Intrusive feldspar-quartz-monzonite-diorite porphyry (FQMP). FQMP-I1: Phenocrystic orthoclase and plagioclase-phyric monzonite and tabular Feldspar (SSD23LZ073, TTD-134 930.3m), FQMP-I2: Hornblende-biotite phyric monzodiotite (SSD23LZ006, TTD-109 1015.45m), FQMP-I3: Pyroxene, hornblende, biotite, plagioclase phyric monzonite (SSD23LZ010, TTD-109 1130m) and FQMP-I4: Phenocrystic plagioclase and orthoclase phyric monzonite (SSD23LZ055, TTD-134 701m).

The Stuhini Group volcanic rocks and mafic-derived volcano-sedimentary rocks are composed of basaltic to basaltic andesite volcanic flows and form the main host to the porphyry Cu-Au deposit. The volcanic rocks at Saddle North are medium to dark green, fine-grained with rare plagioclase phenocrysts up to 3 mm in length (Fig. 4.2). The Stuhini Group is variably altered across the contact zone with the intrusive unit in the study area ranging from weak to intense carbonate clay alteration, as pale grey to white rocks with abundant pyrite clots (Fig. 4.2). The volcanic rocks commonly contain pyrite stringers and pyrite replacing mafic phenocrysts that contain abundant <1 mm micro-fractures commonly filled with pyrite and chalcopyrite, carbonate ± quartz. Secondary minerals including calcite replace or fill veins, whereas clay minerals, minor chlorite, and epidote mostly occurred as replacement textures.



Figure 4.2. Sample SSD23LZ001 (TTD-109 18.56m) volcanic (greenish) country rock which consists of a fine-grained groundmass cross-cut by porphyritic intrusive rock (contact zone), cut by some calcite and quartz veins.

At Saddle North, the intrusive breccia is poorly to moderately sorted and varies from clast to matrix-supported with sub-angular to sub-rounded clasts consisting of variable proportions of monomictic breccia, commonly > 1 cm in size (Fig. 4.3), matrix, and silica-cement. Both the matrix and clasts have a similar composition, with the matrix consisting of recrystallized rocks and zones of breccia that are variably altered (Fig. 4.3). The matrix comprises intensely altered monzodiorite, whereas the clasts are intensely altered with relict K-silicate alteration with weak clay overprinting. The matrix is typically fine-grained and dark grey to black with intact beige plagioclase phenocrysts. Within breccia zones, locally, quartz—calcite—pyrite veins occur, and in some instances, these veins are also brecciated. Quartz—magnetite veins cross-cut both the clasts and the matrix of the breccia and are associated with sulphide-bearing veins as well as disseminated sulphides. (Fig. 4.3).

4.2. Hydrothermal Alteration

Hydrothermal alteration within the Saddle North area comprises variously intense and pervasive styles. The two most abundant alteration styles are potassic and quartz sericite, affecting both the intrusions and host rock and are closely associated with gold and copper mineralization related to pervasive potassic to phyllic altered zones. The potassic and quartz-potassic alteration is pervasive in the deposit and closely associated with gold and base metal mineralization. Strong potassic alteration and quartz-potassic alteration are the most common alteration types at Saddle North (Fig. 4.4A), with both characterized by the development of fine-grained magnetite and secondary biotite in monzonite-diorite and monzonite that is in contact with mafic volcanic rocks. Locally, the potassic alteration is accompanied by both disseminated magnetite, pyrite and chalcopyrite and in various thin veins (Fig. 4.4B).

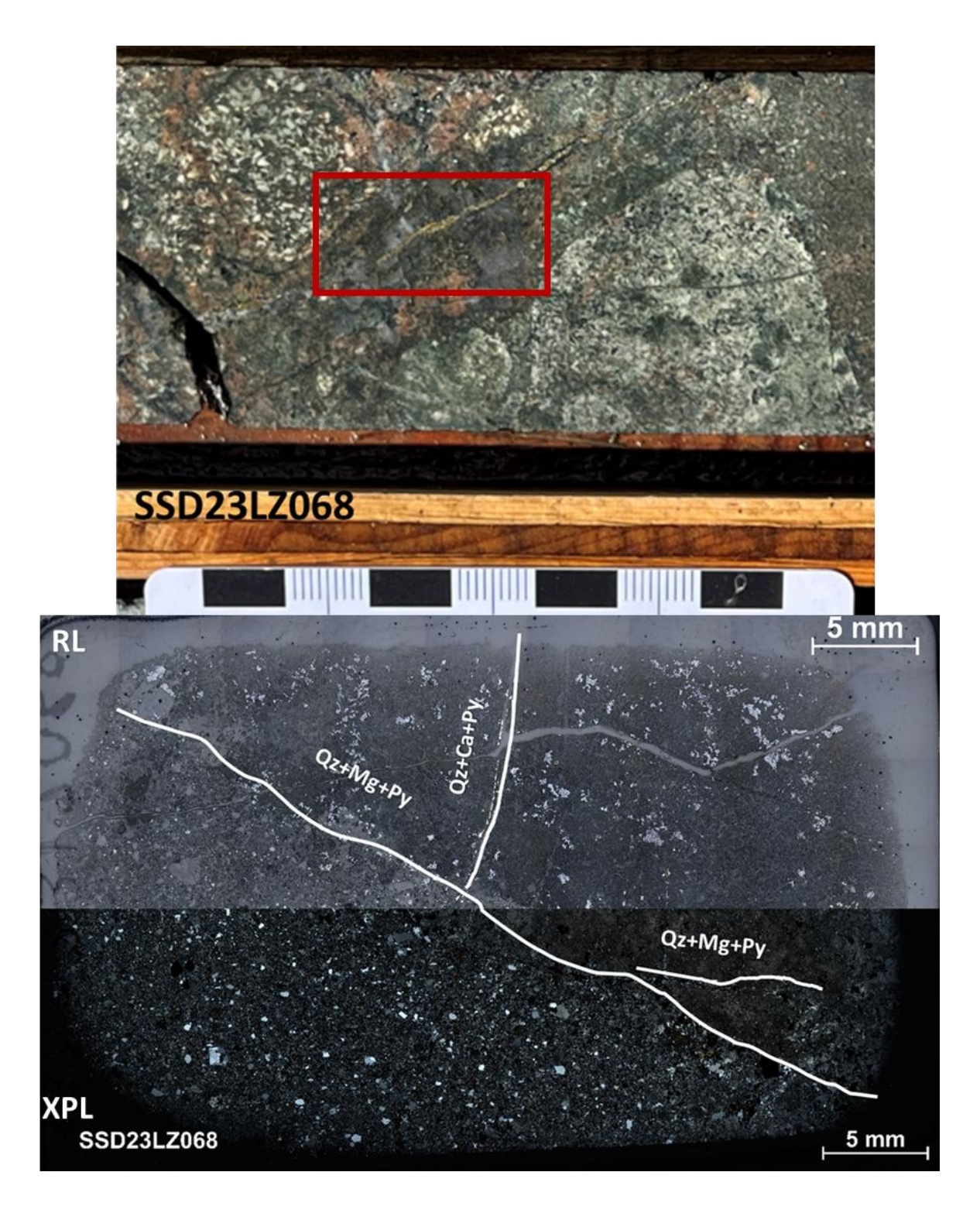


Figure 4.3. Intrusive breccia with irregular clasts is representative of the volcanic host rock, lines indicate the veins (thin section images (XPL) and (RL) Reflected light) — (Sample SSD23LZ068, TTD-134 883.3m).

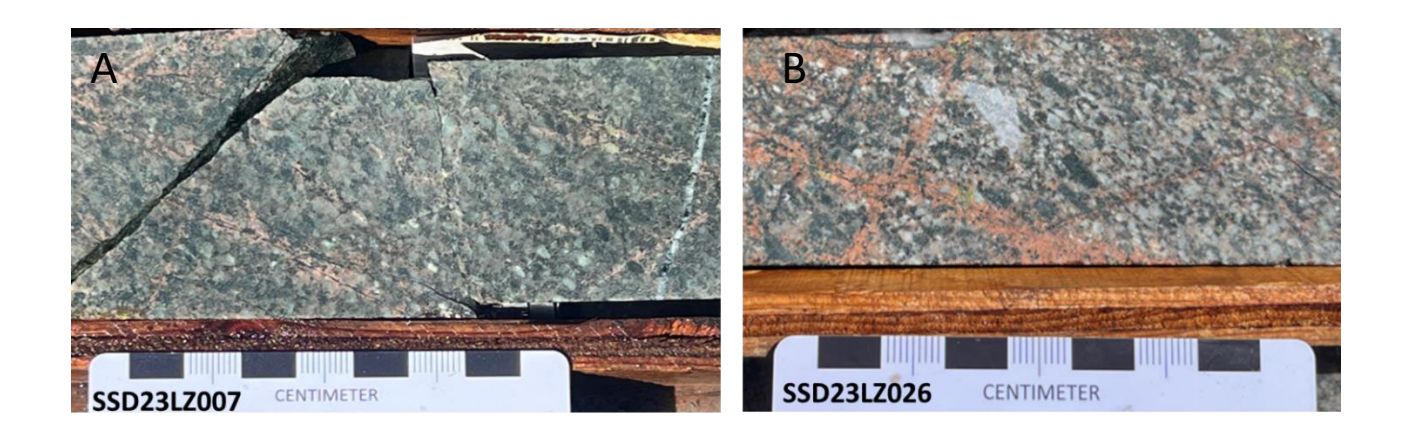


Figure 4.4. A. Weakly altered porphyry intrusion altered (potassic, sample SSD23LZ007, TTD-109, 1035m), and B. Intensely altered porphyry intrusion (potassic, sample SSD23LZ026, TTD-109, 1063m). In general, potassic alteration occurs in an irregular pattern in the core of the main zone and appears as a halo in veins overprinting all earlier alteration phases.

Propylitic alteration is characterized by secondary epidote, chlorite, and calcite (Fig. 4.4), whereas calcite typically occurs in veinlets. This alteration is widespread but variably developed in the mafic volcanic rocks and is locally present in the diorite (Fig. 4.5). Sericite (clay)-chlorite-pyrite alteration is locally moderately to intensely overprinted by potassic and illite alteration (Fig. 4.6). Chlorite replaces primary hornblende and biotite. Pyrite occurs as minor, fine-grained clots and with very fine-grained trace chalcopyrite within the groundmass, locally in clots and along vein margins (Fig. 4.5).

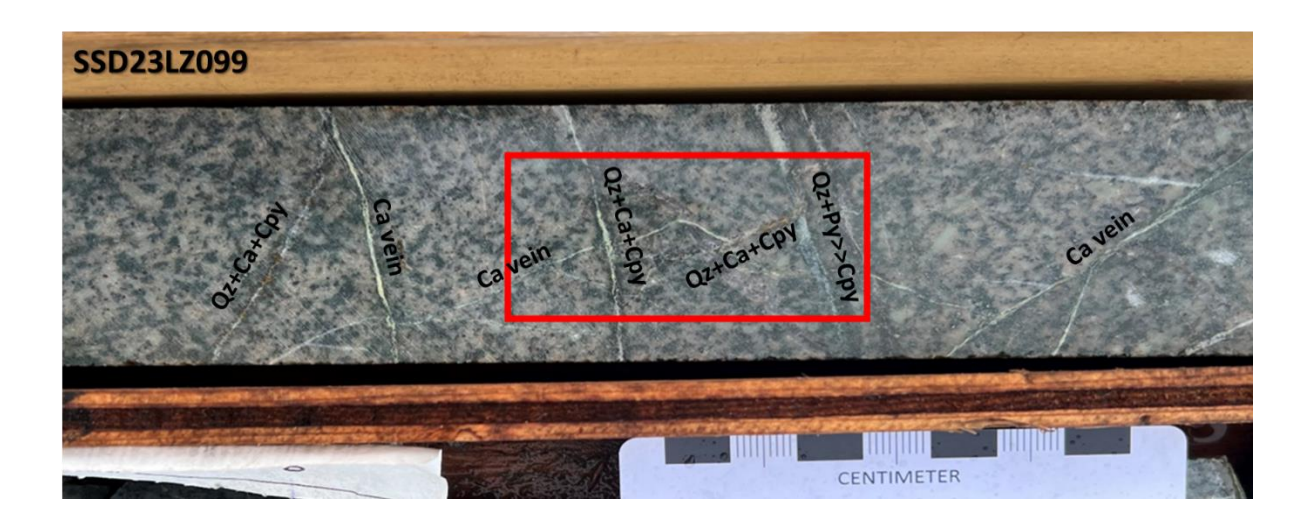


Figure 4.5. Weak sericite alteration overprinting potassic and cut by quartz, calcite and sulphide veins, calcite veins, and disseminated magnetite (Sample SSD23LZ099, TTD-128, 1428.45m).

Phyllic alteration is not extensively developed and was only observed locally in the quartz-feldspar porphyry and feldspar-quartz-hornblende porphyry where it overprints the quartz-sericite alteration (Fig. 4.5). It is characterized by clay minerals (kaolinite?), sericite and carbonates, which partially or completely replace plagioclase phenocrysts. This alteration style is also associated with disseminated pyrite (Fig. 4.6).



Figure 4.6. Phyllic alteration cut by quartz and carbonate veins, with disseminated coarse-grained pyrite + magnetite. (Sample SSD23LZ044, TTD-093 883.8m)

4.3. Vein Relationships

Eight major vein types have been recognized (A. Qz+Mag+Py+Cpy, B. Qz+Cpy>Bn (A-vein) C. Qz+Mo+Cpy+Py (B-vein), D. Qz+K-Fsp>Py, E. Py vein, F. Qz+Py+Cpy (D-vein), G. Ca+Py (Sulphides) vein, and H. Ca vein) at Saddle North (Table 4.1). These veins are recognized in the alteration zone, with quartz-pyrite veins being the most abundant. The veins have been listed from oldest to youngest and

divided into four paragenetic stages as early, main, late and post-mineralization veins based on mineralogy and similarities in timing, mineral assemblage, related alteration assemblages, and their cross-cutting relationship. However, due to their distribution, not all veins were observed as individual veins in each intrusive stage, but there is generally enough evidence to interpret the relative timing and sequence of the veins as part of the hydrothermal evolution of the mineralization in the porphyry deposit.

Table 4.1 Vein sets at the Saddle North porphyry deposit. Potassic alteration is pervasive and crosscut by quartz-dominated vein types: A. Qz+Mag+Py+Cpy, B. Qz+Cpy>Bn (A-vein) C. Qz+Mo+Cpy+Py (B-vein), D. Qz+K-Fsp>Py, E. Py vein, F. Qz+Py+Cpy (Dvein), G. Ca+Py (Sulphides) vein, and H. Ca vein.

	Veins	Early	Main	Late	Post-Min
A.	Qz+Mg+Py+Cpy				
В.	Qz+Cpy>Bn (A-vein)				
C.	Qz+Mo+Cpy+Py (B-vein)				
D.	Qz+K-Fsp>Py				
E.	Py vein				
F.	Qz+Py+Cpy (D-vein)				
G.	Ca+Py (sulphides) vein	_			
Н.	Ca vein				

Early-stage veins represent the earliest mineralizing events within the Saddle North porphyry system and are characterized by a diverse mineral assemblage that includes quartz-only veins, quartz-sulphide combinations (Fig. 4.7A), as well as sulphide-magnetite veinlets comprising chalcopyrite, pyrite, molybdenite, and lesser amounts of bornite. These early veins are particularly abundant within zones of intense K-feldspar alteration, consistent with the high-temperature potassic core typically observed in porphyry systems (Table 4.1 A–D). The mineralogical association of magnetite and early chalcopyrite, in conjunction with K-feldspar, suggests that these veins formed under relatively oxidized and high-temperature conditions, commonly interpreted as proximal to the main magmatic-hydrothermal source in similar porphyry deposits across the Golden Triangle region (e.g., Red Chris, Galore Creek, and KSM deposits).

Main-stage veins are characterized by a distinct assemblage of sulphides and iron oxides, notably chalcopyrite, magnetite, bornite, hematite, and pyrite (Fig. 4.7F). These are commonly hosted in quartz veins that may contain minor to moderate carbonate infill (Table 4.1 C–G), potentially indicating localized neutralization processes or fluid evolution during vein formation. Quartz within these veins is often recrystallized and fine-grained, particularly along the margins, indicative of dynamic recrystallization and fluid-rock interaction during vein emplacement (Fig. 4.7A). Magnetite in these veins is typically concentrated along the vein margins and is also found as disseminations in the adjacent wall rock (Fig. 4.7, red rectangle; Fig. 4.8A), suggesting a continuation of oxidizing conditions during this mineralizing pulse. This style of mineralization and alteration is consistent with transitional zones observed in other porphyry Cu-Au systems of the Golden Triangle, reflecting temporal and spatial evolution of the hydrothermal system from early potassic to later more sulphide-rich stages.

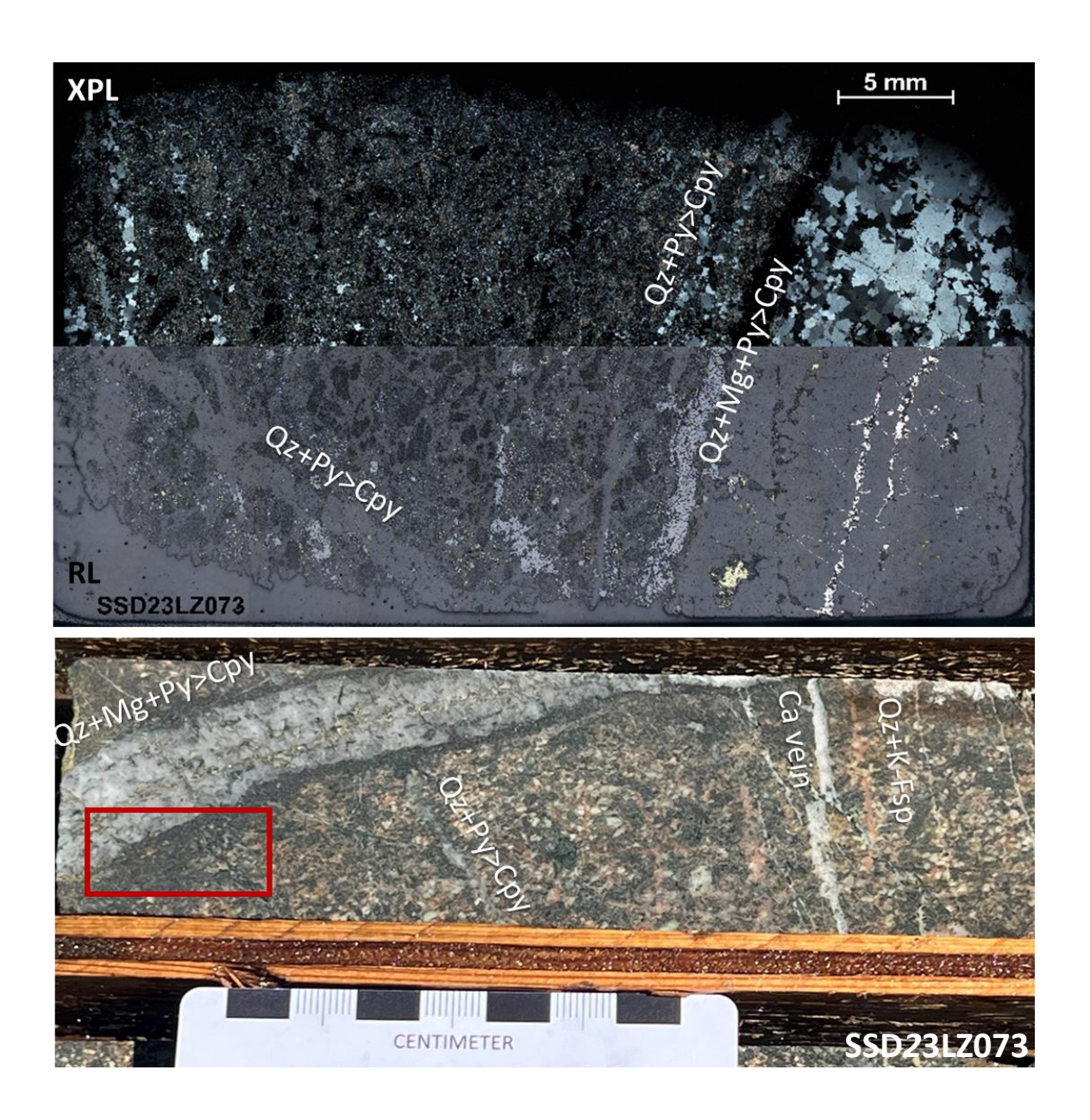


Figure 4.7. Vein A. Qz+Mg+Py>Cpy (A vein set), B. Qz+Py>Cpy (F vein set), C. Qz+K-Fsp (D vein set), and D. Ca vein (H vein set), sets classified according to Table 4.1. Magnetite in clusters, and halo in the quartz veins, sample SSD23LZ073 (the red box corresponds to the thin section and core sample. TTD-134, 930.4m).

Late-stage veins are represented by a diverse suite of mineral assemblages, including quartz + pyrite ± chalcopyrite (Fig. 4.8B), quartz-magnetite ± chalcopyrite (Fig. 4.8A), carbonate + pyrite-chalcopyrite (Fig. 4.9A), as well as barren to weakly mineralized calcite veins (Fig. 4.8B; Table 4.1 E-G). These veins are consistently associated with pervasive quartz-sericite-pyrite (QSP) alteration,

characteristic of the phyllic alteration zone, and typically form a later overprint on earlier potassic and main-stage assemblages.

Texturally, late-stage veins tend to be narrower and more irregular compared to the earlier quartz-sulphide and magnetite-bearing veins. Their spatial distribution and paragenetic relationships—often crosscutting K-feldspar-altered domains and main-stage veins—indicate their formation during the waning stages of the hydrothermal system. Notably, calcite veins are particularly abundant in this stage and frequently dominate the later vein set, clearly crosscutting earlier quartz-rich and sulphidebearing veins (Fig. 4.8A and B).

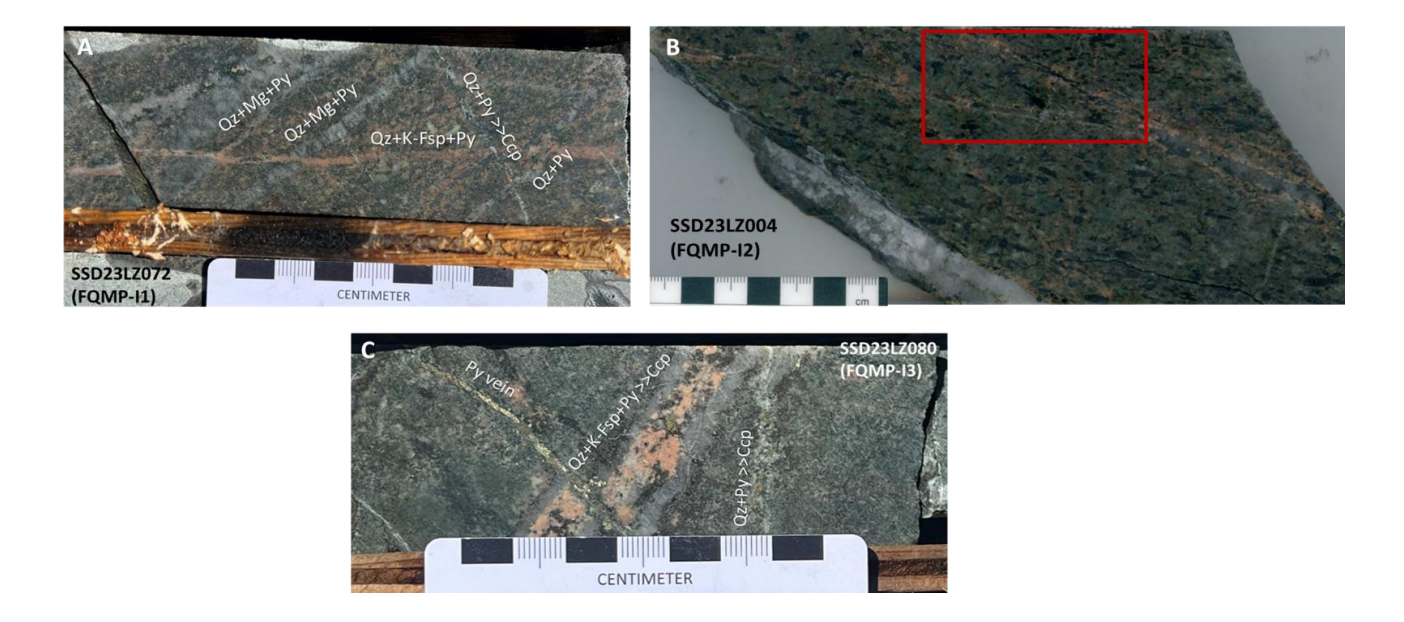
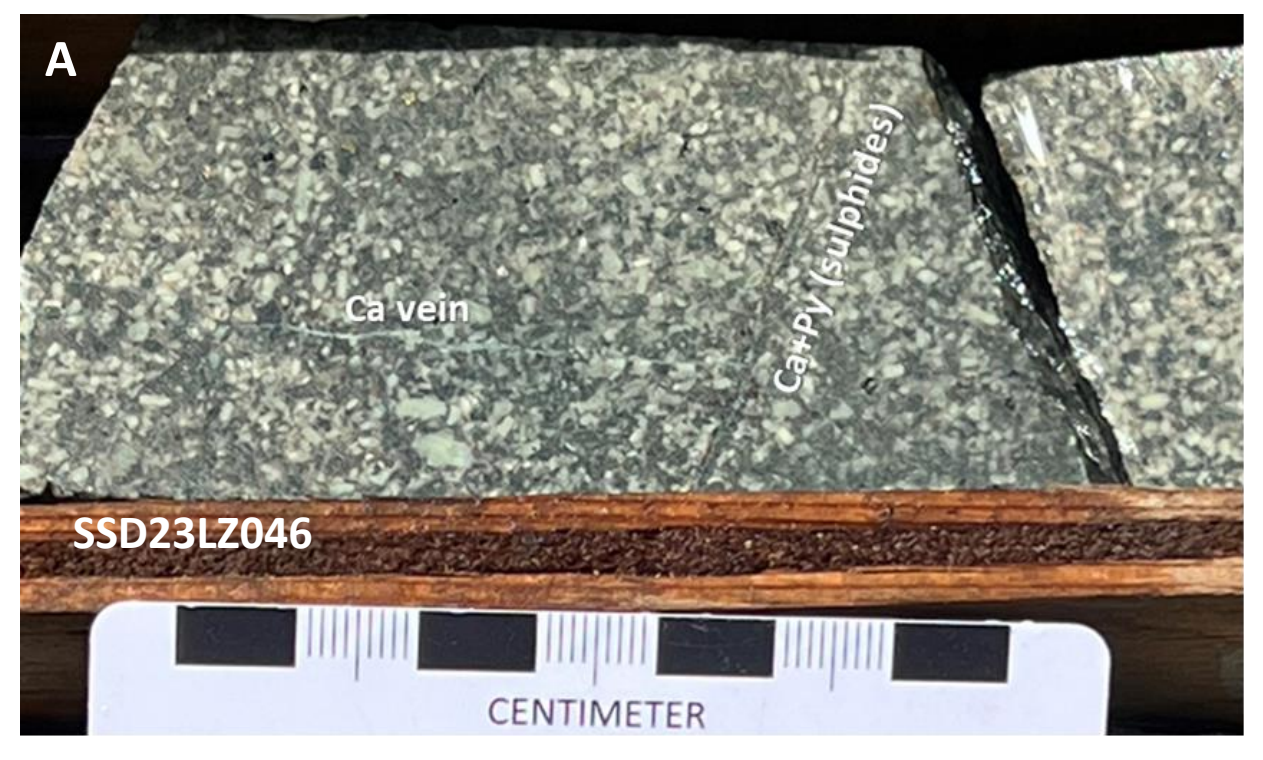


Figure 4.8. A. FQMP-I1 Stock work cross-cutting Qz+Mg+Py, Qz+K-Fsp+Py >>Ccp, Qz+Py, Qz+Py >>Ccp (Early Stage, sample SSD23LZ072, TTD-134, 914.3m). B. FQMP-I2 stock work Qz+Ccp>Bn (K-feldspar more or less developed in most veins), Carbonate vein, Qz+Py (Main Stage, sample SSD23LZ004, TTD-109 942.7m), and C. FQMP-I3 stock work crosscutting Qz+Mg+Py, Qz+K-Fsp+Py >>Ccp, Qz+Py >>Ccp. Magnetite is disseminated and forms a halo in the quartz veins (Late Stage, sample SSD23LZ080, TTD-134 1027m).

Post-mineralization veins cross-cut all rock and vein types. The veins consist of carbonate, quartz-carbonate-bearing, quartz, pyrite, and occasional minor chalcopyrite veins (Fig. 4.9.A; Table 4.1. F-H), and cross-cut quartz-sulphide-iron oxide (molybdenite, Fig. 4.9.B) veins.



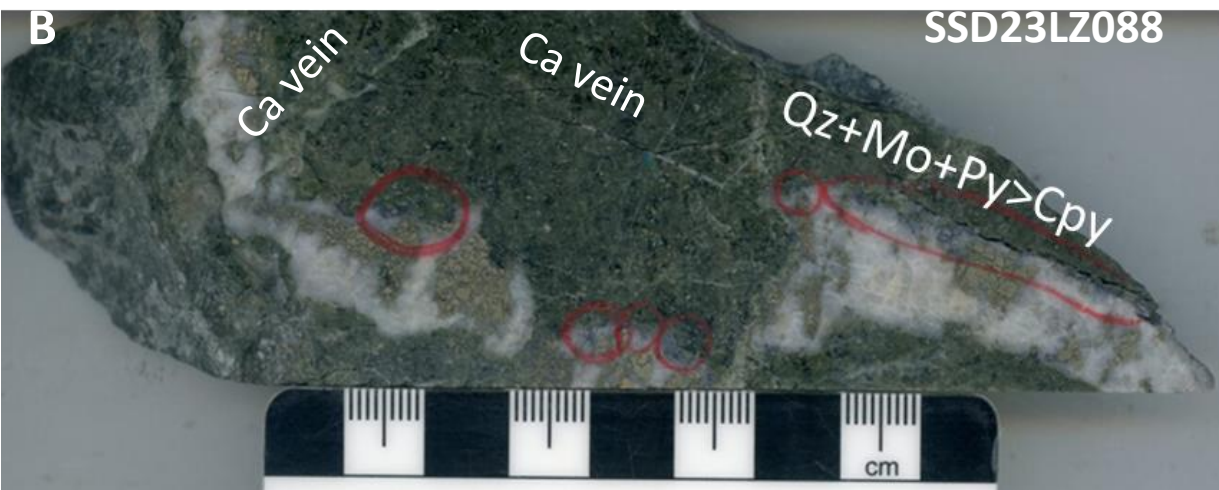


Figure 4.9. A. FQMP-I4 (Sample SSD23LZ046, TTD-093 891m) cross-cut by Ca+Py veins, and Carbonate vein (Post-mineralization. H). B. Stuhini group (Volcanoclastic, sample SSD23LZ088, TTD-128 1350.67m) veins Qz+Mo+Py+Cpy (Early Stage. C), Ca vein (in fill. G). The red circles are molybdenite. Cross-cutting by Ca vein sets, where seen, represents the youngest vein stage.

The four main intrusion stages show diffuse boundaries of K-feldspar alteration in the mineralization zone. In the areas of potassic alteration, disseminations and vein mineralization types contain a variety of magnetite, pyrite, chalcopyrite, bornite, molybdenite and calcite, and secondary minerals such as chlorite, epidote and rarely hematite, which are related to the mineralization within progressive events that are responsible for the majority of veins in the deposit. Micro-XRF chemical maps were used for the identification and distribution of various primary and secondary mineral assemblages of Si, Al, K, Ca, Fe, Mg and P in some samples, especially those related to alteration zone (Fig. 4.10). These elements are controlled by the distribution and composition of minerals in the samples and can be used to determine the mineralogy and hydrothermal alteration (Fig. 4.10 A, B, C and B), and minerals such as chalcopyrite, pyrite, hornblende, apatite, quartz and aluminosilicate-quartz matrix. The veins are associated with the distribution of four porphyry intrusions and temporally with early to later potassic alteration assemblages (Fig. 4.10 C and D) and post-mineralization (phyllic) alteration.

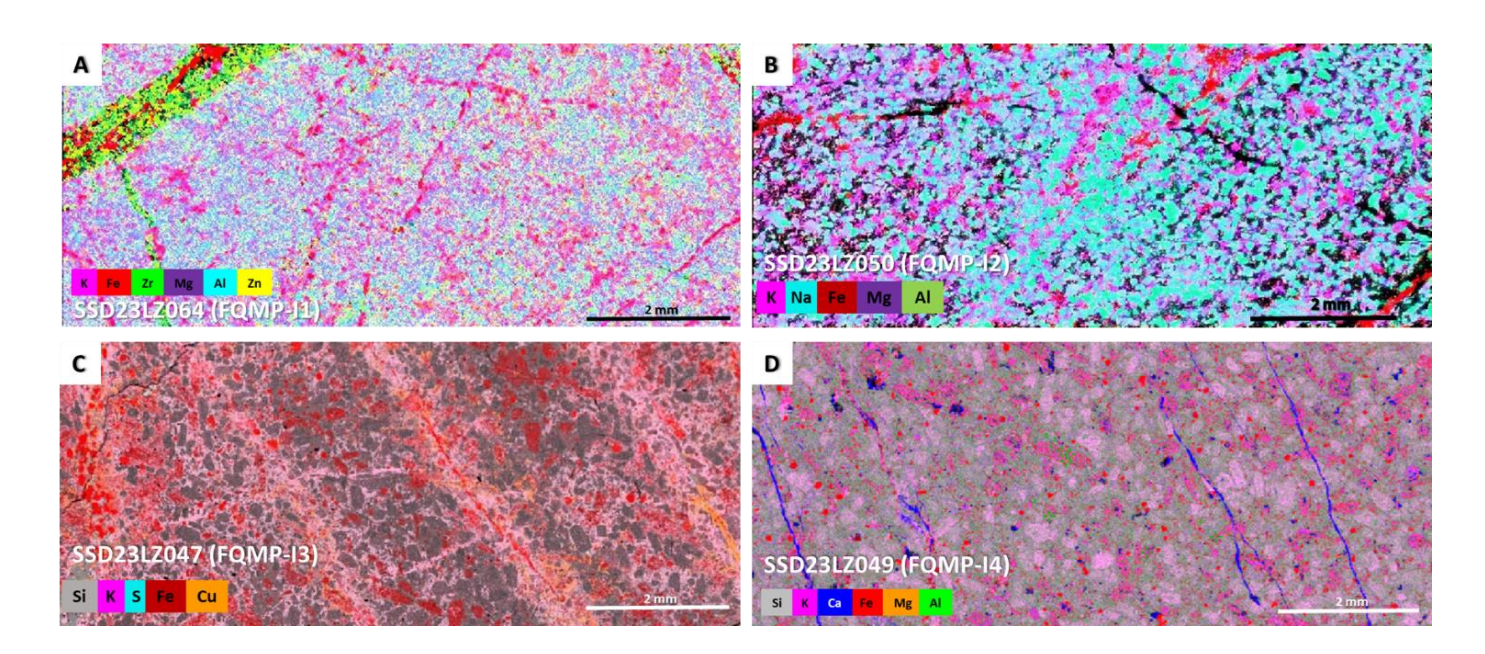


Figure 4.10. Micro XRF elemental maps. A. FQMP-I1 (Sample SSD23LZ064, TTD-134 852m) High-K alteration. C. FQMP-I2 (Sample SSD23LZ050, TTD-134 656m) high to moderate K-alteration intensity, pervasive and distributed. C. FQMP-I3 (Sample SSD23LZ047, TTD-093 844.44m) cross-cut vein distribution in the moderate-K alteration. D. FQMP-I4 (Sample SSD23LZ046, TTD-093 890m) carbonate (Ca) vein sets distribution in weak alteration characterizes the youngest vein stage.

The resolution of this technique enables the distinction of minerals present in the units, allowing for the visualization of both large and small minerals with contrasting chemical components. The presence of pink K-feldspar (Fig. 4.10A) marks zones of potassic alteration, including vein halos, and is spatially associated with a broad area exhibiting high Na-Al composition at relatively constant intensity, represented by light blue in the geochemical map (Fig. 4.10B), with Fe (red color; Fig 4.10.C), that represent a large proportion of the rock and groundmass indicating a correlation between the most common alkaline elements (Na, Ca; Fig. 4.10). The occurrence of biotite, hornblende, and magnetite shows a strong correlation with elevated concentrations of aluminum (AI), titanium (Ti), and iron (Fe), and is associated with relatively low levels of manganese (Mn) and magnesium (Mg), reflecting their typical compositions and stability in porphyry magmatic-hydrothermal environments (Seedorff et al., 2005). Trace elements such as zinc (Zn), phosphorus (P), titanium (Ti), and zirconium (Zr) also appear to be enriched in these areas. In contrast, quartz is notably depleted relative to these elements, suggesting its limited association with the mineralized groundmass (Fig. 4.10). Similarly, elevated phosphorus (P) intensities were observed to spatially correlate with localized zones of high calcium (Ca) concentrations, particularly in small, disseminated areas. This geochemical association is consistent with the presence of finely disseminated apatite crystals, which are a common accessory phase in both igneous and hydrothermal environments. The apatite occurs as small grains within the groundmass or associated with alteration assemblages and is most clearly expressed in the elemental maps as overlapping Ca-P anomalies (Fig. 4.11).

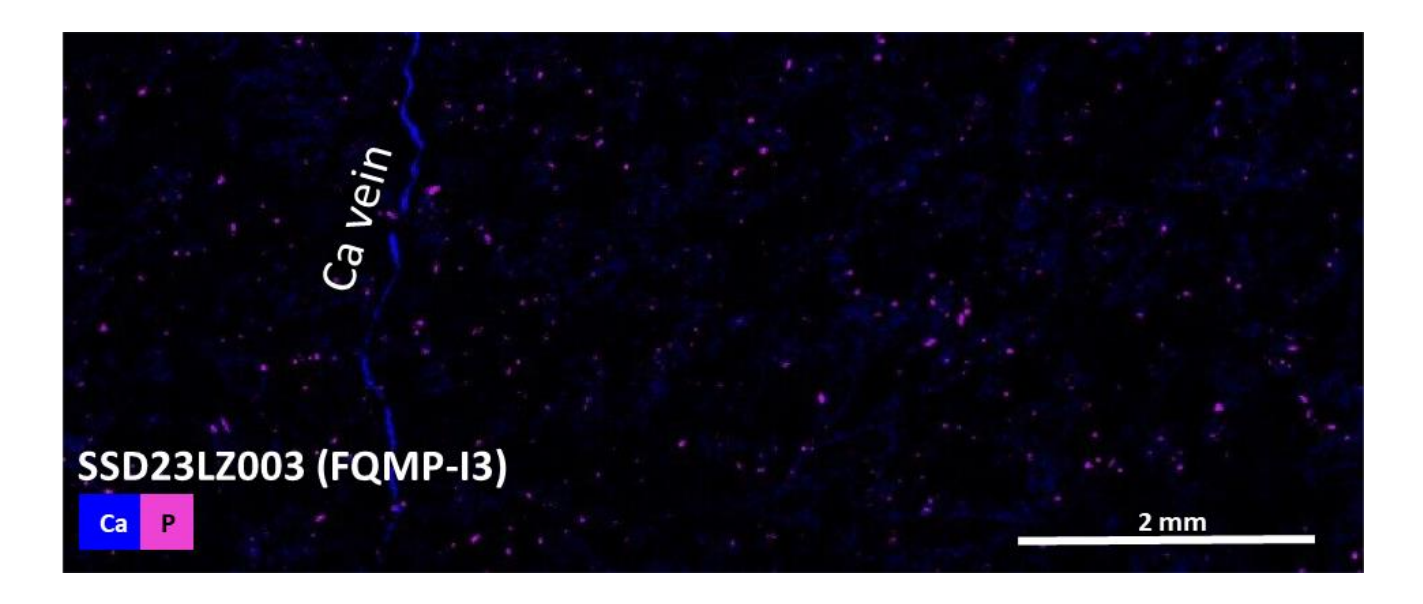


Figure 4.11. Micro XRF elemental maps of sample FQMP-I3 (Sample SSD23LZ003, TTD-109 619.33m) showing the distribution of phosphorus (P) and calcium (Ca) within a high to moderately altered intrusion. The spatial correlation of P and Ca reflects the presence of small, disseminated apatite crystals, which commonly incorporate both elements. These apatite grains are key accessory minerals that can provide insights into the petrogenetic and hydrothermal history of the intrusion.

4.4. Whole-rock Geochemistry

Samples for whole-rock geochemical analysis were selected to represent various rock types, textures and alteration types. Whole-rock geochemical analyses were obtained for thirty-five samples, including ore-bearing quartz monzonite porphyry and host rock samples from the Saddle North porphyry deposit. The rocks at Saddle North have SiO_2 contents between 52.3-60.8% (Fig. 4.12 A) and have been classified into monzonite to monzodiorite intrusive rocks (feldspar-quartz-monzodiorite-porphyry, FQMP) with an alkalic and calc-alkalic affinity (Nb/Y = 0.1-0.6; Fig. 4.12 B). Potassic alteration can affect the Na_2O and K_2O concentrations, which means that discrimination diagrams that use mobile major elements tools cannot be used (Fig. 4.12 A, $Na_2O + K_2O$ versus SiO_2 diagram of Middlemost, 1985). Representative rock types were plotted on the Zr/TiO_2 versus Nb/Y diagram (Pearce, 1996 modified after Winchester and Floyd, 1977; Fig. 4.12 B) with the samples from Saddle North plotting on the boundary between the basalt, and

andesitic-basaltic andesite fields with a modal distribution of Zr/Ti ratios that clearly distinguish higher (0.003-0.005) and lower Zr/Ti groups (0.001-0.003; Fig. 4.12 B).

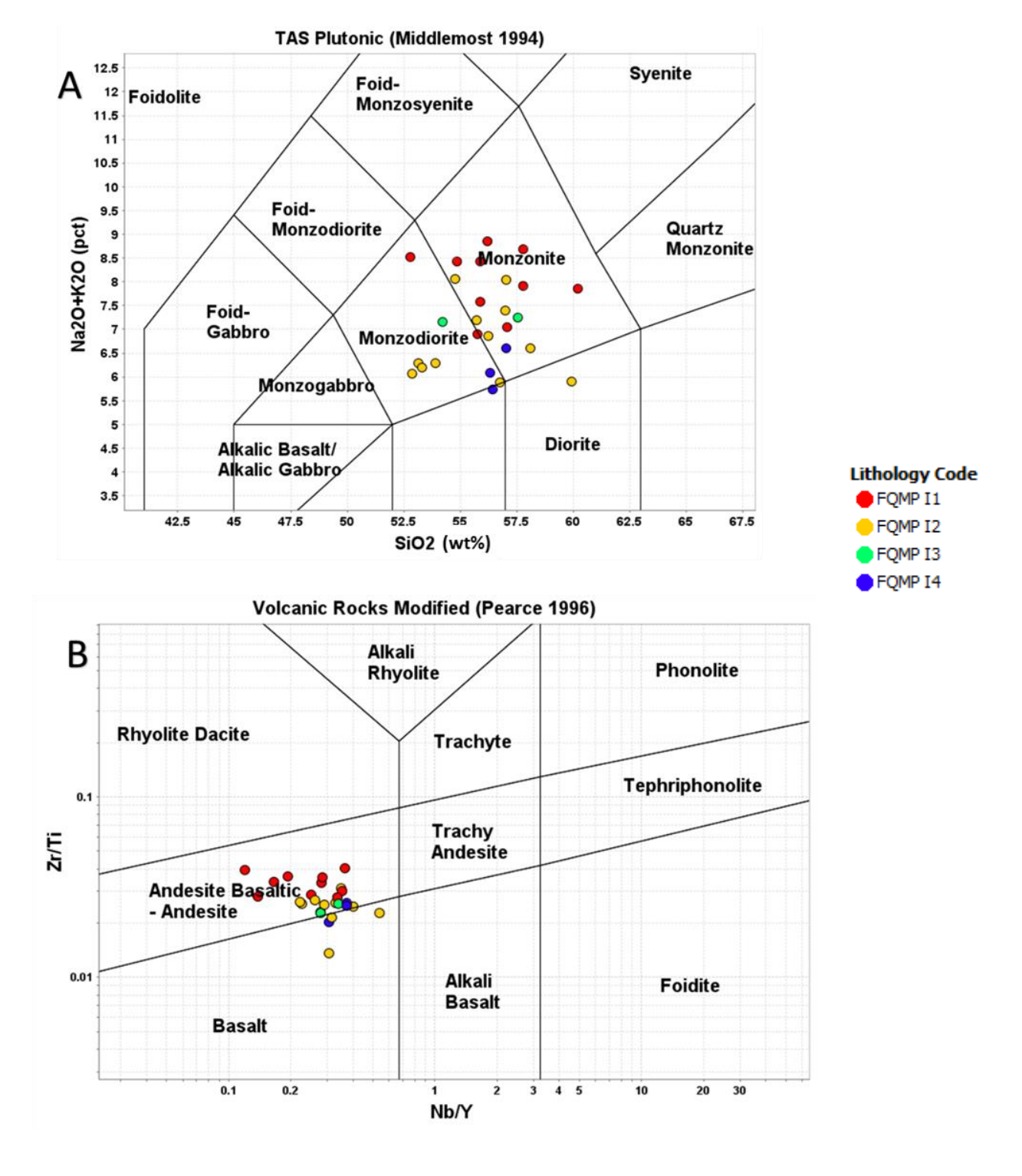


Figure 4.12. A. TAS diagram for plutonic rocks (Middlemost 1994) and B. Zr/Ti vs Nb/Y diagram for volcanic rocks (Pearce, 1996 modified after Winchester and Floyd, 1977).

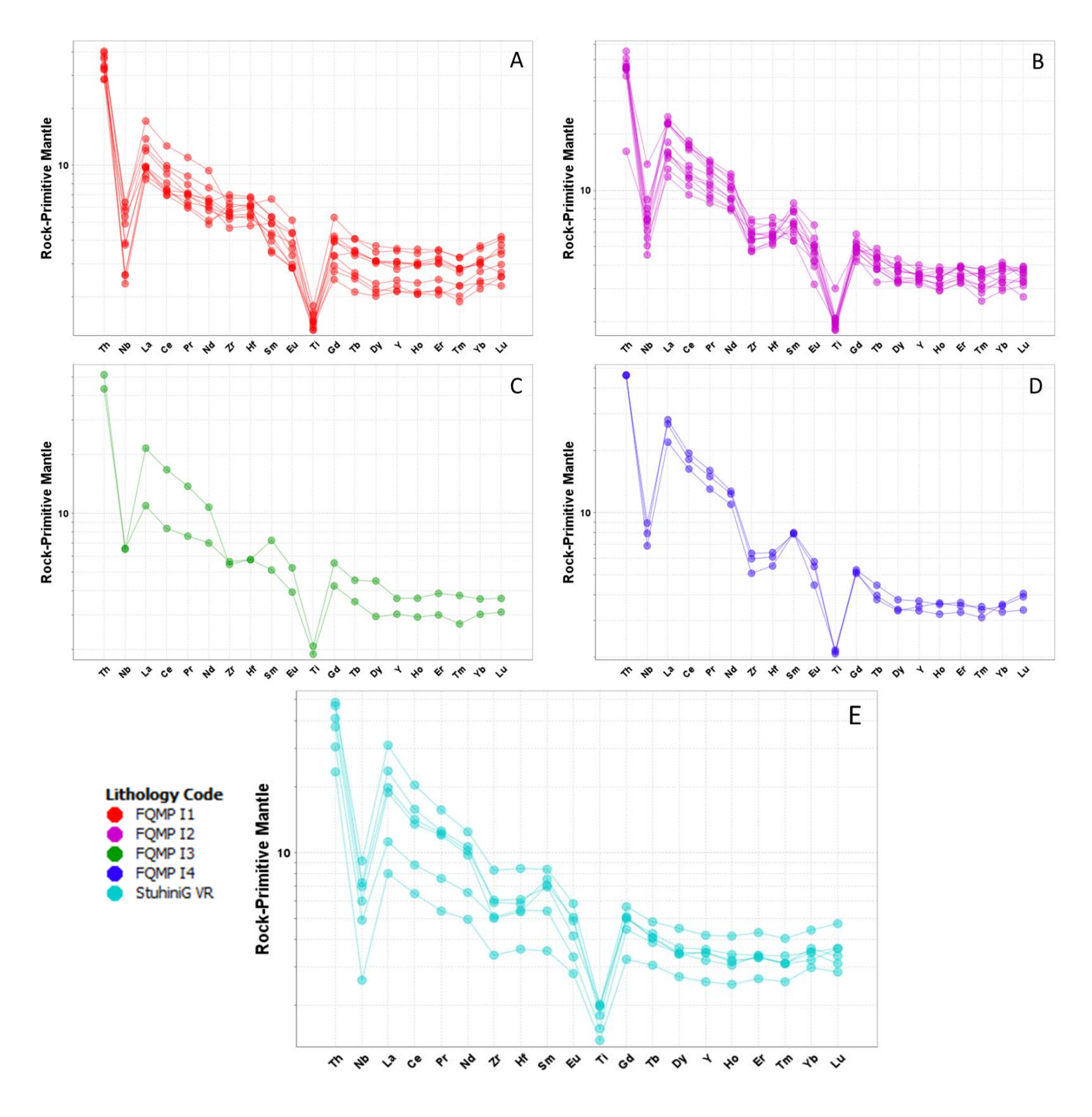


Figure 4.13. Primitive mantle-normalized trace elements diagram of the Saddle North Intrusive rock (monzodiorite) A. FQMP-I1, B. FQMP-I2, C. FQMP-I3, D. FQMP-I4 and host rock (volcanic rock – E. Stuhini group volcanic rocks from the Saddle North Project (Normalizing values from Sun and McDonough, 1989).

The Saddle North intrusions all display moderate to strong negative Nb and Ti anomalies relative to REE, weak negative to positive Zr and Hf anomalies and small negative for Eu anomalies (Fig. 4.13). The intrusive units display little variation among samples in terms of trace element patterns or total trace element abundances, within almost identical REE patterns with a listric-shape (steep slopes from light REE (LREE) to MREE), and shallow slopes from MREE to HREE. Those patterns are consistent with subduction-related igneous rocks (Fig. 4.13).

All the feldspar—quartz—monzodiorite porphyry (FQMP) intrusions associated with the Cu—Mo deposits at Saddle North share similar chemical and petrographic characteristics and have similar shapes on primitive mantle-normalized diagrams (Fig. 4.13). These criteria are consistent with observations from other British Columbia porphyry systems, such as Red Chris (Rees, 2015) and Galore Creek (Micko et al., 2014), where multiple intrusive events are temporally and chemically linked to mineralization pulses.

4.5. Geochronology

Laser ablation inductively coupled plasma mass spectrometry (LA-ICP-MS) dating was completed on 10 samples from the intrusions and host rocks at Saddle North. The calculated of U-Pb dating results for zircon grains from the feldspar-quartz-mozodiorite porphyry and diorite are listed in Appendix 3 and plotted on Concordia plots in Figures 4. 14 and 4. 15 zircons were found (modeled in IsoplotR; Vermeesch, 2018). The results yield crystallization ages that range between approximately 205 and 209 Ma, displaying a range of ages from Upper Triassic to Early Jurassic. The feldspar-quartz-hornblende porphyry intrusion samples contains a relatively homogeneous population of zircons characterized by subtle age dispersion and minor discordance (Fig. 4. 14 A-F and Fig. 15 A-C), in contrast diorite sample contains a slightly more complex population, with minor discordance and a slightly broader age spread (Fig. 4. 15 D).

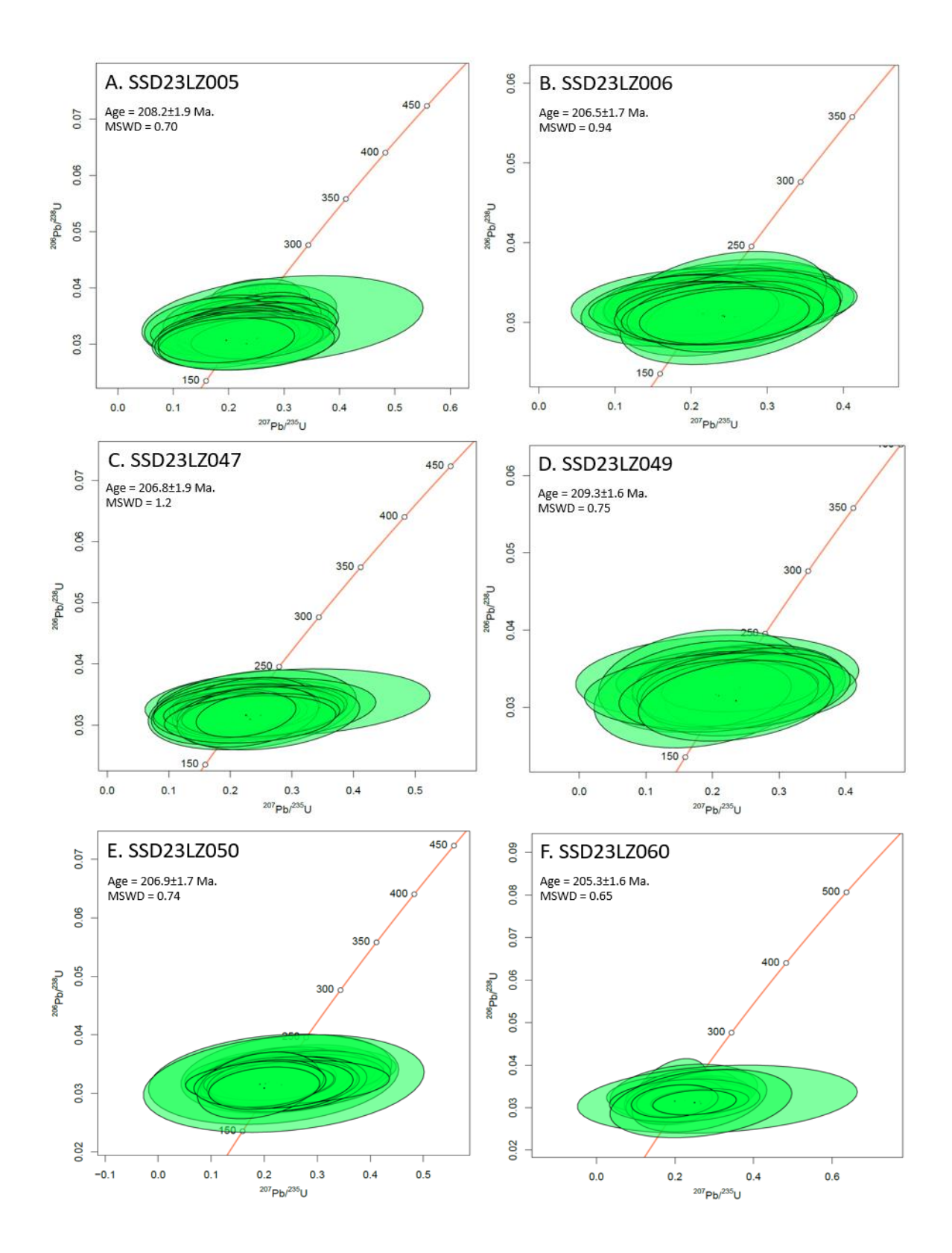


Figure 4.14. Concordia plots for zircon grains from dated samples (A. SSD23LZ005, B. SSD23LD006, C. SSD23LZ047, D. SSD23LZ049, E. SSD23LZ050, and F. SSD23LZ060; model in IsoplotR (Vermeesch, 2018)).

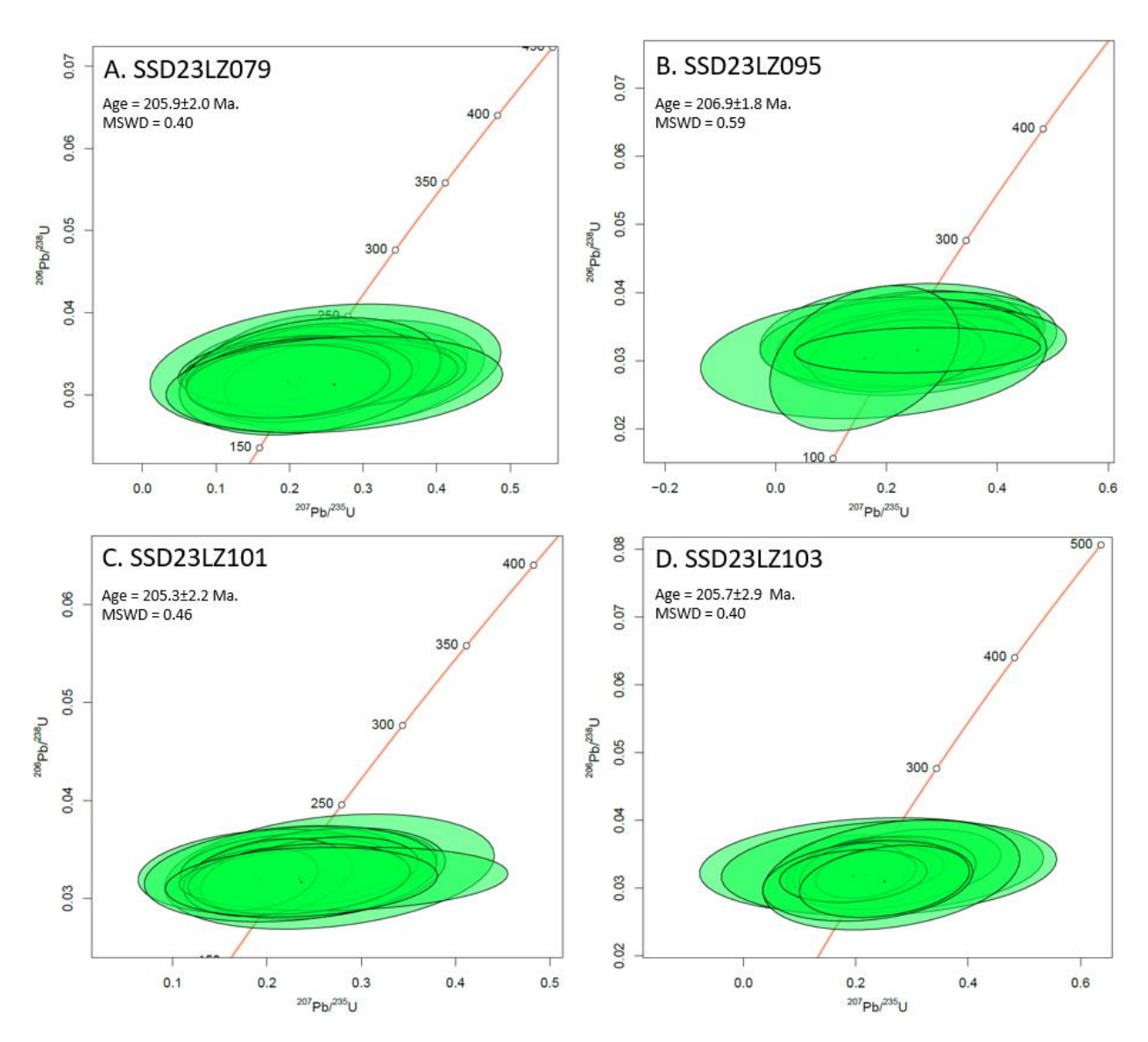


Figure 4.15. Concordia plots for zircon grains from dated samples (A. SSD23LZ079, B. SSD23LD095, C. SSD23LZ101, and D. SSD23LZ103; model in IsoplotR (Vermeesch, 2018)).

In general, results show a relatively homogeneous average crystallization age of 206 \pm 2 Ma with some differences in the populations. The volcanoclastic host rock (Diorite, Fig. 4.16) and the monzodiorite intrusions (Fig. 4.17, A-H). Sample (SSD23LZ103) is a fine to medium-grained diorite (host rock), chlorite and phyllic altered diorite with 206 Pb/ 238 U ages ranging from 229.7 \pm 20.1 Ma to 198.9 \pm 12.3 Ma with all 16 grains yielding a concordant age of 205.7 \pm 2.9 Ma (MSWD=0.40; Fig. 4.16).

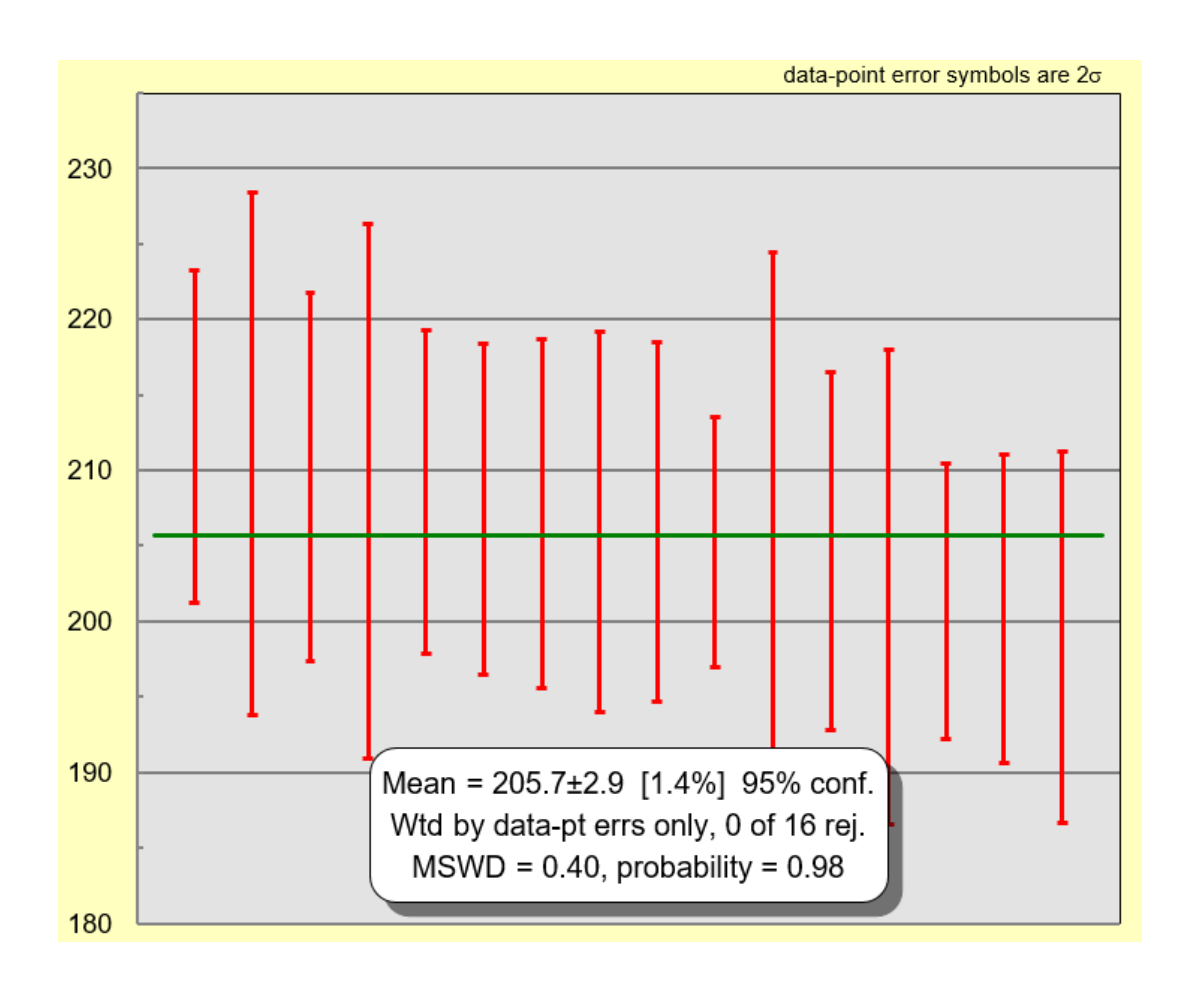


Figure 4.16. Diagram for the age of host rock samples SSD23LZ103 (16 Zr spots; Stuhini group).

Sample SSD23LZ060 corresponds to a monzodioritic phase of the FQMP-I1 intrusion, characterized by plagioclase, K-feldspar, hornblende, and biotite phenocrysts embedded within a fine-grained groundmass composed of K-feldspar and minor quartz, and exhibiting intense potassic alteration. U–Pb zircon dating yielded 206 Pb/ 238 U ages ranging from 214.8 ± 11.1 Ma to 198.8 ± 8.2 Ma, with all 62 analyses defining a weighted mean age of 205.3 ± 1.7 Ma (MSWD = 1.19; Fig. 4.17F). This age likely represents the timing of crystallization and emplacement of the FQMP-I1 phase. Multiple samples were analyzed from the FQMP-I2 monzonite—monzodiorite phase, which is texturally characterized by abundant plagioclase and hornblende phenocrysts, a fine-grained K-feldspar-dominant groundmass, and variable but generally moderate to strong potassic alteration (Table 4.2).

Table 4.2. Summary of LA–ICP–MS U–Pb zircon ages from selected Saddle North samples.

Sample ID	Age Range (Ma)	No. of Spots	Weighted Mean Age (Ma) ± 2σ	MSWD	Figure Ref.
SSD23LZ005	250.1 ± 7.8 – 199.2 ± 7.8	67	208.2 ± 1.8	0.70	Fig. 4.17A
SSD23LZ006	212.7 ± 9.7 – 197.2 ± 8.8	80	206.5 ± 1.7	0.94	Fig. 4.17B
SSD23LZ050	215.7 ± 10.4 – 199.2 ± 7.8	72	206.9 ± 1.7	0.74	Fig. 4.17E
SSD23LZ079	212.6 ± 12.7 – 197.5 ± 13.4	62	205.9 ± 2.0	0.40	Fig. 4.17G
SSD23LZ095	213.4 ± 20.3 – 197.3 ± 8.9	63	206.9 ± 1.9	0.59	Fig. 4.17H

A representative sample of the FQMP-I3 phase (SSD23LZ047), also a monzonite—monzodiorite, shares similar petrography—plagioclase and hornblende phenocrysts with a fine-grained K-feldspar—rich groundmass and moderate to intense potassic alteration. It produced $^206Pb/^238U$ ages ranging from $^216.7 \pm 14.2$ Ma to $^219.5 \pm 7.9$ Ma, with all 70 grains yielding a mean age of $^2206.8 \pm 1.9$ Ma (MSWD = $^21.2$; Fig. 4.17C). Sample SSD23LZ101 from the FQMP-I4 monzodiorite phase, petrographically similar to FQMP-I1, contains coarse to medium-grained plagioclase and hornblende phenocrysts in a fine-grained groundmass, and is affected by moderate to weak potassic and phyllic alteration. The zircon population yielded ages ranging from $^211.2 \pm 16.5$ Ma to $^2201.2 \pm 9.0$ Ma, with a weighted mean age of $^2205.3 \pm 2.2$ Ma (MSWD = $^220.46$; Fig. 4.17I, Appendix A).

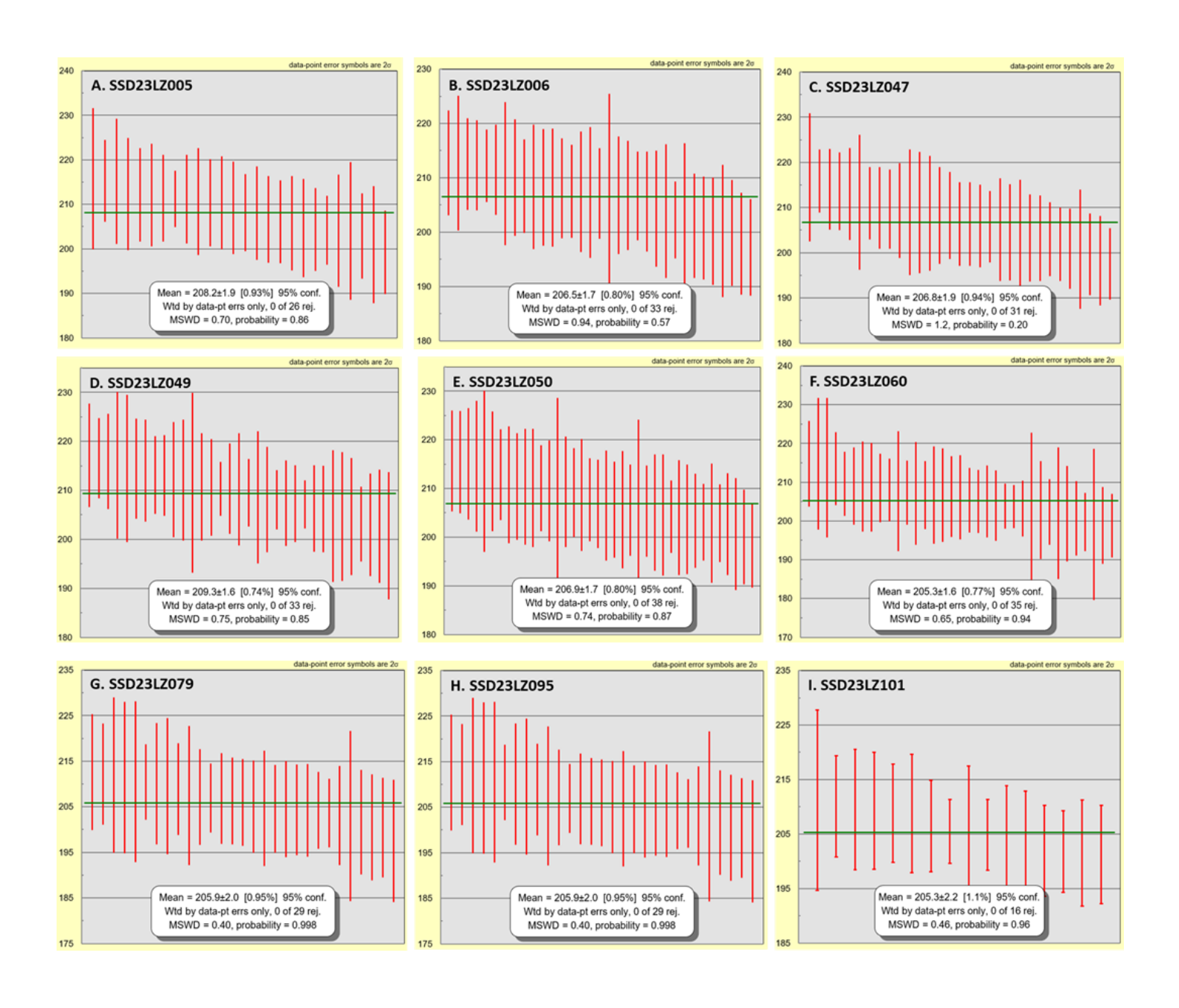


Figure 4.17. Diagram for the age of intrusions samples A. SSD23LZ005 (26 Zr spots; FQMP-I2), B. SSD23LZ006 (33 Zr spots; FQMP-I2), C. SSD23LZ047 (31 Zr spots; FQMP-I3), D. SSD23LZ049 (33 Zr spots; FQMP-I4), E. SSD23LZ050 (38 Zr spots; FQMP-I2), F. SSD23LZ060 (35 Zr spots; FQMP-I1), G. SSD23LZ079 (29 Zr spots, FQMP-I2), H. SSD23LZ095 (29 Zr spots; FQMP-I2) and I. SSD23LZ101(16 Zr spots; FQMP-I4), Saddle North deposit.

Molybdenite at Saddle North occurs as very fine to fine-grained crystals in quartz-molybdenite veins commonly associated with pyrite (Fig. 4.16). The Re-Os age technique was used to date the molybdenite-bearing quartz vein in the sample (SSD23LZ088). The veins are hosted by altered plagioclase-hornblende-biotite porphyry, which is probably overprints earlier potassic alteration. The sample was collected from drill hole TTD-128 at a depth of 1350.67 m and yielded a Re-Os age of 205.6 \pm 0.8 Ma (Table 4.3).

Table 4.3. Molybdenite Re-Os data from Saddle North Project.

SAMPLE	Re ppm	± 2s	¹⁸⁷ Re ppm	± 2s	¹⁸⁷ Os ppb	± 2s	Model Age (Ma)	± 2s (Ma)
SSD23LZ088	110.6	0.3	69.53	0.18	238.58	0.01	205.6	0.8



Figure 4.18. Sample SSD23LZ088, from the Saddle North Intrusion complex with molybdenite + quartz veins (red circles).

Chapter 5. Discussion

Porphyry deposits are major sources of global copper, gold, and molybdenum (Kesler, 2002). As exploration continues in well-known porphyry districts, the challenge arises of detecting and uncovering buried deposits (Sillitoe, 2010). Porphyry copper-related intrusions typically consist of several phases, including early porphyries, inter-mineralization porphyries, late-mineralization porphyries, and post-mineralization porphyries, which intrude after the cessation of ore-forming processes and typically lack significant hydrothermal alteration or sulphide mineralization (Gustafson, 1978).

The porphyry deposits of northern Stikinia occur in a similar regional geological framework formed as part of the Paleozoic Stikine terrane assemblage. The Saddle North deposit is hosted in the Stuhini and Hazelton Group volcanic rocks along with associated sedimentary rocks formed within the arc-back terrane during the Late Devonian and Early Jurassic (Nelson & van Straaten, 2021). The composition of the Saddle North intrusions varies widely, ranging from medium- to fine-grained hornblende biotite granodiorite to quartz monzonite to monzodiorite, with differing amounts of primary quartz as well as phenocryst mineralogy and texture. These intrusions are categorized based on modal mineralogy, crosscutting relationships, and the degree of alteration and presence of mineralization. They have been divided into four distinct intrusive phases (FQMP-I1, FQMP-I2, FQMP-I3, and FQMP-I4; Table 5.1). The intrusive phases are intercalated throughout the core, displaying complex cross-cutting relationships. The intrusions are characterized by strong hydrothermal alteration consistent with visual observations of the drill core (potassic, phyllic, propylitic, and argillic; Table 5.2). The presence of K-feldspar defining zones of potassic alteration where the mineral has been identified in the geochemical map (by μXRD scan; Fig. 5.1), were compared with the intrusion types observed and documented on the Saddle North property by the Saddle Project exploration team (Newmont Mining Corporation, 2023). The results of this study are consistent with Newmont's exploration team nomenclature for the intrusive units and alteration styles,

given the similarities in petrographic assemblages to the compositionally variable, texturally equigranular to inequigranular porphyritic intrusions, geochemical affinities, and spatial relationships. The correlation between the intrusive chronology and hydrothermal alteration patterns at Saddle North reinforces a strong genetic link between magmatism and mineralization. Geochronological data (e.g., U–Pb zircon and Re–Os molybdenite ages) indicate that the emplacement of multiple intrusive phases temporally overlaps with key alteration events, particularly potassic and quartz–sericite alteration, which are spatially and mineralogically associated with copper and gold mineralization. This temporal and spatial overlap suggests that metal-bearing hydrothermal fluids were derived directly or indirectly from evolving magmatic sources. Such relationships are characteristic of well-developed porphyry systems, where episodic intrusive activity provides the heat and fluid flux necessary to drive long-lived hydrothermal systems (Sillitoe, 2010; Richards, 2011). At Saddle North, the alignment of mineralization with early to syn-mineral intrusions, coupled with alteration zoning and crosscutting relationships, supports a magmatic-hydrothermal continuum similar to other porphyry Cu–Au systems in the Golden Triangle and globally (Bouzari et al., 2020).

Table 5.1. Intrusion paragenesis. Saddle North feldspar quartz monzodiorite porphyry (FQMP) intrusive phases. This classification is based on cross-cutting relationships and a gradual decrease in pervasive potassic alteration.

STAGE	EARLY	MAIN	LATE	POST-MIN.
Intrusion 1				
(FQMP-I1)				
Intrusion 2				
(FQMP-I2)				
Intrusion 3				
(FQMP-I3)				
Intrusion 4				
(FQMP-I4)				

The distribution and intensity of the hydrothermal alteration assemblages, crosscutting relationships, textural characteristics, and their relation to intrusive units were used to establish a paragenetic sequence for the mineralization and alteration divided into early, main, late, and post-mineral stages, each featuring

several distinct mineral assemblages and various vein types (Tables 4.1 and 5.2). The primary alteration and Au-Cu mineralization stage was associated with eight vein types, categorized based on cross-cutting relationships (Table 4.1) and linked to the intensity of potassic alteration, including an early to late stage of K-feldspar quartz monzodiorite porphyry. The widespread potassic alteration assemblage, which includes biotite, magnetite, and K-feldspar, along with minor quantities of quartz and disseminated magnetite, chalcopyrite, and pyrite, is concentrated in FQMP-I1 to I4 (sulphide veins and pyrite veins; Figs. 5.1 and 5.2). This suggests a genetic and temporal relationship between the intrusive phases and the mineralizing hydrothermal fluids, indicating that magmatic activity played a direct role in driving hydrothermal alteration and metal deposition. Micro-XRF elemental mapping reveals widespread potassium enrichment—especially concentrated within the intrusive phases—which underscores the intensity and extent of potassic alteration affecting these rocks (Fig. 5.1). Such K-enrichment is consistent with high-temperature hydrothermal fluids characteristic of the potassic core zones in porphyry systems.

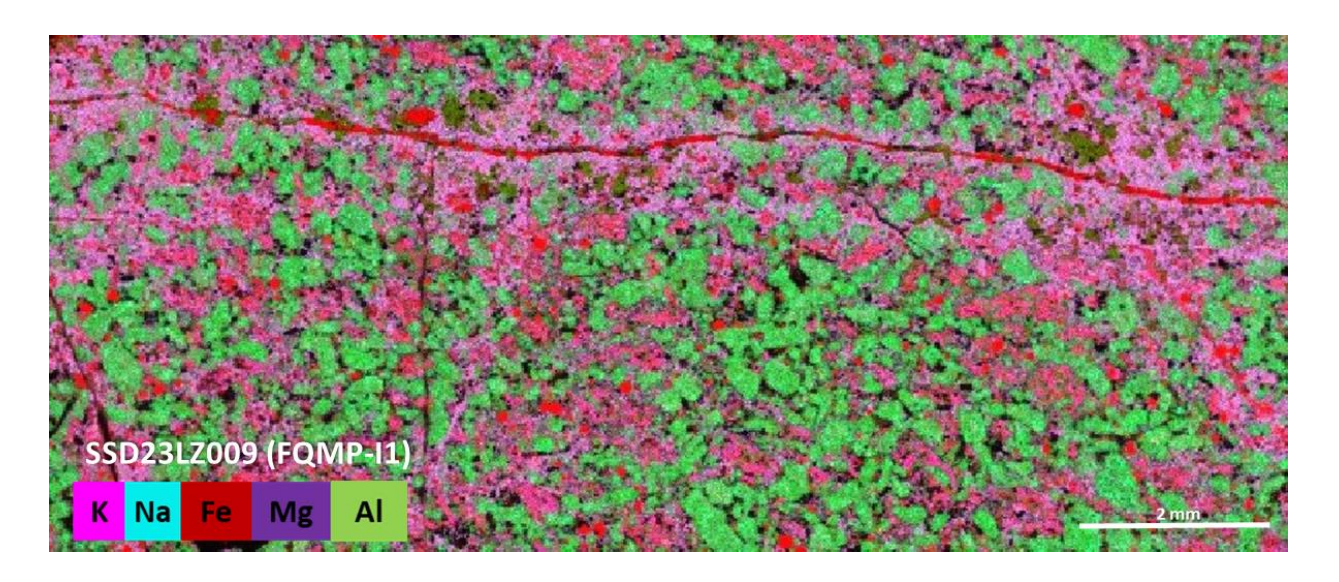


Figure 5.1. Sample SSD23LZ009 (TTD-109. 1104 m; FQMP-I1), development of alteration halos, particularly K-feldspar (secondary) and biotite and disseminated magnetite (µXRF image).

The hydrothermal alteration closely relates to the formation of secondary K-feldspar, resulting from the replacement of primary minerals, which occurs alongside the development of biotite and magnetite. The

presence of secondary K-feldspar represents a key feature of potassic alteration, formed through hydrothermal replacement of primary plagioclase and groundmass feldspars by K-silicate fluids (Sillitoe, 2010; Seedorff et al., 2005). Hydrothermal halos formed by fluid rock interaction along vein margins, often accompanied by pyrite and other sulfides related to the emplacement of different porphyritic intrusive phases, due to cross-cutting relationships and the gradual decrease in intensity of the K-feldspar abundance (Fig. 4.10). The intrusions at Saddle North are texturally diverse porphyritic units, predominantly monzodiorite with minor monzonite and serve as the primary host for copper-gold mineralization associated with intense potassic alteration (Allen et al., 1976; Enns et al., 1995). Micko (2014) proposed that they were emplaced over a relatively short period from a single magmatic event during the evolution of the intrusive phases. Moreover, Redmond and Einaudi (2022) described how, in porphyry deposits, the most intense potassic alteration correlates with the highest metal grades. In contrast, less intense potassic alteration correlates with the lowest metal grades. The variations in coppergold mineralization and the intensity of potassic alteration across different intrusive phases at Saddle North align with the spatial distribution patterns described by Brodbeck (2022). These patterns highlight the relationship between alteration intensity and mineralization within the porphyry system (Fig. 5.2).

Seedorf et al. (2005) and Flynn and Kelly (2020) argued that the spatial and temporal association between intrusive phases, porphyry-style stockwork veining, potassic alteration, and elevated Cu–Au grades reflects a fundamental genetic link between magmatism and hydrothermal mineralization in porphyry systems. Seedorf et al. (2005) described how potassic alteration—typically characterized by secondary biotite, K-feldspar, and magnetite—is intimately associated with early-stage quartz—sulphide stockwork veining, forming within or near the apical parts of porphyry intrusions. This assemblage commonly marks the highest-temperature and most Cu-Au-fertile part of the system. Similarly, Flynn and Kelly (2020) demonstrated that intrusive phases temporally associated with potassic alteration and veining not only act as sources of heat and metal-bearing fluids but also control the geometry and distribution of

mineralization zones. At Saddle North, this relationship is evident in the spatial overlap between strongly potassic-altered intrusions, well-developed A-type quartz-magnetite-chalcopyrite veins, and zones of high copper and gold grades, supporting a coherent magmatic-hydrothermal model for deposit formation.

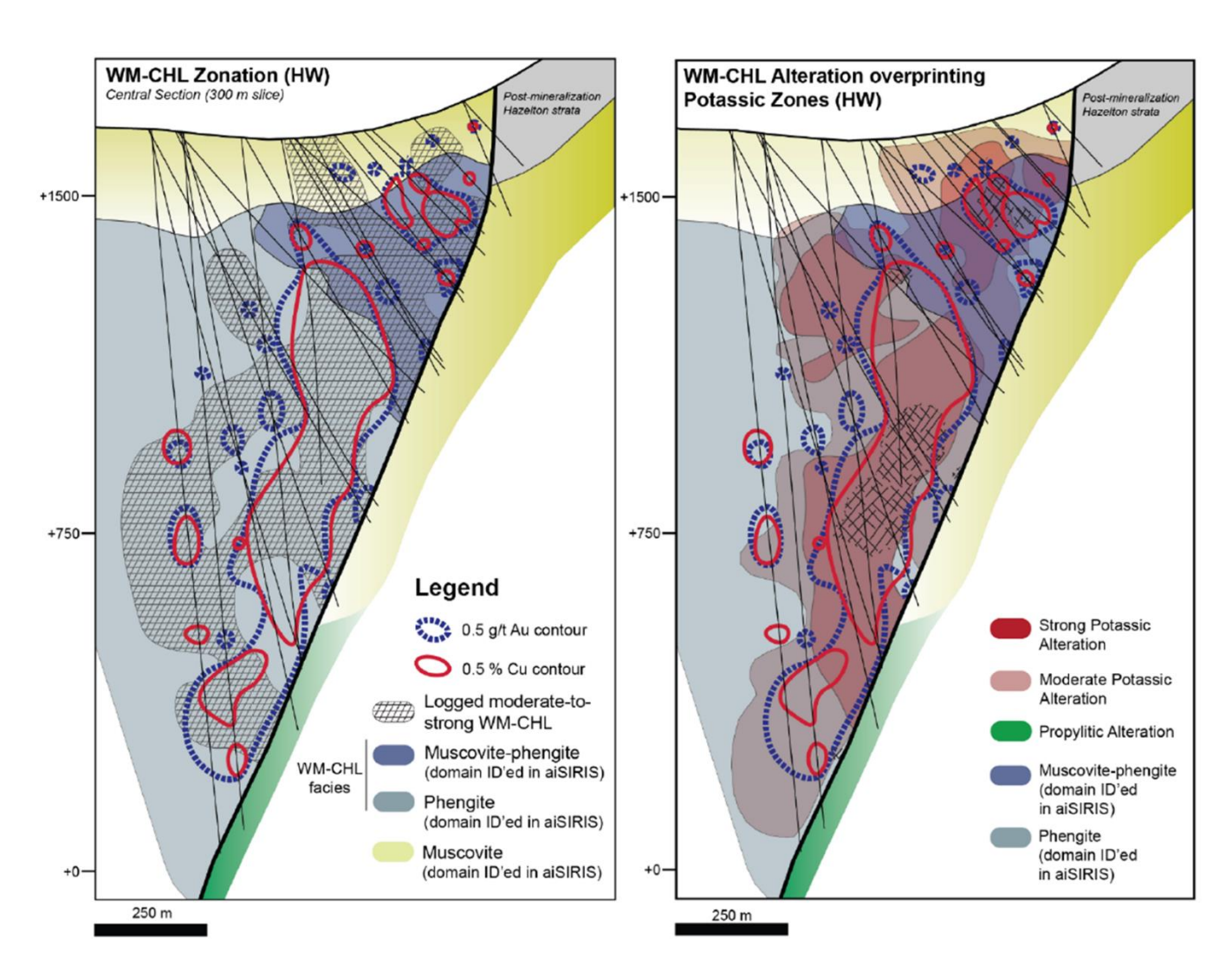


Figure 5.2. The Saddle North porphyry system's conceptual cross-section illustrates the spatial distribution of Cu-Au mineralization and alteration intensity across distinct intrusive phases—Modified from Geology, Au-Cu mineralization, hydrothermal alteration and structural features | Saddle North Rock Atlas internal report. Courtesy of Newmont's Saddle Exploration team.

Petrographic observations across the four intrusive phases at Saddle North reveal relatively consistent hypidiomorphic textures and comparable mineral assemblages, indicating minimal textural variation despite differences in alteration and modal mineralogy. These similarities suggest a closely related

magmatic evolution. The observed increase in modal quartz content—from rare or absent in the earliest intrusive phase (FQMP-I1) to more abundant in FQMP-I2 and subsequent phases—alongside whole-rock SiO₂ concentrations ranging from 52.3 wt.% to 60.8 wt.%, suggests a progressive evolution of the magmas from silica-undersaturated to silica-saturated compositions. This trend is consistent with fractional crystallization processes in arc-related calc-alkaline systems, where early mafic intrusions gradually evolve toward more felsic, quartz-bearing compositions (Gill, 1981; Richards, 2005). However, the interpretation of primary magmatic silica saturation must be treated with caution, as the observed SiO₂ increase may have also been locally boosted by secondary quartz through hydrothermal veining. Quartz veining can significantly increase bulk-rock silica content through passive infilling of fractures, thereby overprinting primary geochemical signatures (Lowell & Guilbert, 1970; Corbett & Leach, 1998; Sillitoe, 2010). Thus, distinguishing between primary igneous quartz and hydrothermal quartz is essential for accurately interpreting the magmatic evolution of the system.

Furthemore, this trend aligns with typical subduction-related arc magmatism, where processes such as fractional crystallization promote silica enrichment in successive intrusive pulses (Winter, 2010; Rollinson, 1993). Additionally, the minor negative Eu anomalies and nearly parallel REE patterns among the phases suggest a shared magma source with progressive geochemical evolution rather than discrete, unrelated magmatic events. The potassic alteration within the deposit contain vein systems that generally form quartz stockwork vein sets (Fig. 5.2 A) and are also associated with hydrothermal breccia (Fig. 4.3). This is similar to other porphyry districts such as Galore Creek and Red Chris in British Columbia (Micko et al., 2014 and Rees, 2015; Table 5.2). Both deposits exhibit a geochemical signature that is similar to the Saddle North system. This similarity is attributed to the presence of multiple intrusive phases and overprinting hydrothermal alteration events, which are closely associated with the stages of mineralization. The four intrusion and complex alteration phases tend to produce geochemical variations even within a single deposit. Such variations reflect differences in the composition and evolution of the magmatic sources. In

the case of porphyry systems like Saddle North, these magmas are typically derived from subduction-related tectonic settings, where fluids and melts from the subducting slab contribute to the generation of arc magmas enriched in volatiles and metals (Richards, 2009). Therefore, the shared geochemical features among these deposits support a common geodynamic origin in subduction zone environments.

Table 5.2. Vein paragenesis and alteration association at Saddle North.

Stage	Vein Types	Common Minerals	Host Phases	Associated Alteration
Early	A, B, C, D	Qz, Mag, Py, Cpy, Mo	FQMP-I1, I2	Potassic
Main	C, F, G	Qz, Cpy, Bn, Py	FQMP-I2, I3	Potassic to weak phyllic
Late	E, F, G	Qz, Py, Cpy, Ca	FQMP-I3, I4	Phyllic (sericite–chlorite)
Post Min	G, H	Ca, Py, minor Qz	All units	Carbonate-chlorite, no mineralization.

Table 5.2 summarizes the observed relationships between vein types and intrusive phases within the Saddle North porphyry deposit. These observations provide critical insight into the temporal and spatial distribution of vein types across intrusive phases, defining a clear paragenetic sequence. The presence or absence of specific vein types in individual units serves as a proxy for the relative timing of hydrothermal events. These observations support a multi-phase magmatic-hydrothermal model, where successive intrusive events and associated fluid pulses controlled the style, distribution, and metal content of mineralization. This paragenetic evolution is consistent with well-established porphyry copper system models (Seedorff et al., 2005; Sillitoe, 2010). Eight vein types are recognized in the four porphyry intrusions at Saddle North, categorized into early-, main, late-, and post-mineralization-stage veins (Tables 4.1 and 5.2). These veins are mostly irregular and discontinuous, composed of varying amounts of chalcopyrite, pyrite, magnetite, molybdenite, and quartz, often featuring local K-feldspar halos (Figs. 5.1 and 5.3A). This sequence, along with cross-cutting relations and vein distribution at Saddle North, is

interpreted to reflect progressive intrusion-related alteration zonation. Four vein types constitute the early-stage veins (Table 5.3 A–D; Figs. 4.7 A, 4.7 C, 4.8 A), primarily hosted in FQMP-I1 and I2, and associated with strong potassic alteration (Fig. 5.3 A). These veins are associated with the main Cu-Au-Mo mineralization and typically contain magnetite, chalcopyrite, and molybdenite.

The development of crystal \pm sulphide veins illustrates the dynamic changes in a high-temperature, saline magmatic-hydrothermal system. The solubility of crystals in the H₂O-NaCl solution is influenced by variations in pressure, temperature, and salinity (Lowenstern, 2015). As the magmatic fluid exsolves from the feldspar-quartz monzodiorite porphyry (FQMP), a rise and subsequent cooling occur, resulting in decreased pressure and temperature that lead to an oversaturation of silica and the precipitation of crystals. This mechanism, which is governed by solubility, creates a thermodynamic framework that enables the understanding of the spatial and paragenetic distribution of quartz-bearing veins at Burden Union. The structure of the veins is characterized by a progression that begins with early A-type veins (Qz + Mag + Py \pm Cpy), transitioning through B-type quartz-molybdenite-chalcopyrite \pm pyrite veins, and eventually leading to the later-stage D-type crystal \pm pyrite veins. These formations represent episodic fluid exsolution, evolving fluid characteristics, and the incomplete cooling of the hydrothermal system.

The A-type veins are characterized by the presence of chalcopyrite, bornite, and minor amounts of pyrite, aligning with the specific characteristics of potassic-stage veins (Sillitoe, 2010). Typically, these veins are hosted within a monzonitic setting and are identified by a medium to coarse-grained groundmass that predominantly features oligoclase and K-feldspar, along with subordinate hornblende and biotite phenocrysts. In contrast, the monzodioritic phase usually reveals a slightly more mafic composition, with a significant presence of mafic minerals like hornblende and biotite, and a relatively fractured arrangement of K-feldspar. Both stages, however, exhibit strong potassic alteration, evidenced by pervasive minor K-feldspar replacing oligoclase, the enlargement of biotite, and the distribution of

magnetite—characteristics typically associated with the potassic core of porphyry systems (Sillitoe, 2010). The B-type veins notably emerge predominantly in the northern charge and can be reliably recognized based on their mineral composition and crosscutting relationships. These veins consist of crystals, molybdenite, and chalcopyrite, with trace amounts of bornite and pyrite (see Fig. 5.3D and Table 5.2). This assemblage is indicative of typical B-veins formed during the initial mineralization phase in porphyry systems (Gustafson & Hunt, 1975; Sillitoe, 2010). They often cut across the potassically altered intrusive stage and are believed to represent the initial hydrothermal pulse responsible for Cu–Au–Mo mineralization. The occurrence of molybdenite in fine quantities suggests the involvement of high-temperature, metal-rich magmatic fluids (Selby & McGeehan, 2000).

Furthermore, geochronological evidence obtained from LA-ICP-MS U-Pb zircon dating suggests that multiple phases of FQMP intrusion occurred between approximately 205 and 208 million years ago. This timing coincides with Re-Os molybdenite ages from B-type veins, which range from 204.2 ± 0.9 million years to 207.8 ± 0.9 million years (Greig, 2021). This overlap highlights a significant relationship between intrusive activities and the hydrothermal processes that lead to ore formation. Additionally, the whole-rock geochemistry derived from altered rocks supports this interpretation, showing major element enrichment (for instance, K_2O and Fe_2O_3) associated with intense vein development and alteration, consistent with fluid-driven metasomatism. Moreover, the observed paragenetic sequences and vein mineralogy at Burden Union align with experimental and thermodynamic models of porphyry formation, where fluctuations in pressure, liquid phase separation, and the solubility of silica facilitate the deposition of quartz and metal-bearing phases (Audétat, 2010; Reed, 1997; Lowenstern, 2015). Collectively, these findings underscore the importance of structurally controlled fluid flow and the evolution of magmatic-hydrothermal environments in influencing metal zoning and vein development within the base porphyry Cu-Au system of the Stikine Terrane (Richards, 2005).

The two styles of early-stage veins at Saddle North resemble the El Salvador veins (type A and B) described by Gustafson and Hunt (1975). Three vein types comprise the main-stage veins, cross-cut early structures, dominate FQMP-I2 and I3, and are associated with potassic to phyllic alteration (Table 5.2 C, F, G; Figs. 4.7 B and 4.8 B). The late-stage includes two vein types (Table 5.2 E, F, G; Fig. 4.8 C) that cut all previous structures and are associated with waning hydrothermal fluid flow and sericite—chlorite alteration. These veins (type F; Table 4.1) are similar to "D" veins of Gustafson and Hunt (1975). Post-mineral veins (Table 5.2 H; Figs. 4.7 D and 4.9 A, 4.9 B) truncate all earlier features and are barren, consisting of carbonate and minor pyrite (Fig. 5.3 C, D, E). These eight vein assemblages at Saddle North are similar to those described (Micko et al., 2014) in other porphyry deposits where early-stage veins are closely associated with potassic alteration (Sillitoe, 2010) with alteration transitioning from early potassic to later-stage, lower-temperature, carbonate-rich veins as documented by Barr (1976), Gustafson & Hunt (1980), Lang (1995), and Sillitoe (2000, 2002, 2010). This temporal evolution also shares many similarities with other porphyry systems, such as Cerro Colorado (Sillitoe, 1985) and Cadia (Wilson et al., 2003), where vein overprinting reflects progressive cooling and depressurization of the magmatic-hydrothermal system.

The mineralization at Saddle North is interpreted to have evolved through four main hydrothermal stages, each marked by distinct variations in vein density and alteration (Fig. 5.3). These stages, from youngest to oldest, are spatially associated with the intense potassic alteration and vein density (Table 5.3 A-E). For example, the early-stage mineralization at Saddle North corresponds to the emplacement of the FQMP-I1 and I2 intrusive phases (Table 5.2), which are characterized by intense potassic alteration and the development of quartz—magnetite—chalcopyrite ± bornite veins. These veins display mineralogical and textural features consistent with A-type veins, associated with high-temperature alteration assemblages including secondary K-feldspar, biotite, and magnetite, commonly found in porphyry copper—gold systems during the initial stages of hydrothermal activity (Gustafson & Hunt, 1975; Sillitoe, 2010). As the hydrothermal system evolved at Saddle North, subsequent intrusive and alteration phases were

associated with progressively lower-temperature fluid regimes. This evolution is supported by the diminishing presence or complete absence of high-temperature mineral assemblages such as magnetite, chalcopyrite, bornite, and molybdenite in later-stage veins and intrusions. These younger stages are characterized by weak potassic to phyllic alteration, the development of carbonate-rich and pyrite-only vein assemblages, and a notable reduction in copper and gold grades. This pattern closely reflects the paragenetic and metallogenic framework proposed by Flynn and Kelley (2020), wherein the later intrusions at Saddle North are less mineralized due to declining metal-bearing capacity of the fluids, that coincides with a transition in alteration style observed in the core, from early K- and Ca-silicate alteration (characterized by secondary biotite, K-feldspar, and magnetite) to later-stage assemblages dominated by phyllic and propylitic alteration (including sericite, chlorite, and carbonate).

This mineralogical transition reflects a decrease in temperature and fluid salinity over time, consistent with a more evolved hydrothermal system and a decline in metal-bearing capacity (Lowell & Guilbert, 1970; Seedorff et al., 2005; Sillitoe, 2010). Such alteration zoning is typical of porphyry systems where fluid composition, temperature, and permeability evolve over time (Sillitoe, 2010; Seedorff et al., 2005; Cooke et al., 2005). The progressive disappearance of magnetite and copper-bearing sulphides in latestage veins at Saddle North, coupled with a dominance of pyrite and carbonate, supports this interpretation (post-mineralization; Table 5.2). This progressive trend reflects the decreasing metal fertility of the fluid source and the progressive dilution by externally derived or evolved fluids, leading to less efficient transport and precipitation of copper and gold. The mineralogical, textural, and alteration changes observed at Saddle North—specifically, the decreasing of magnetite and copper-rich sulphides in later intrusions, and the emergence of pyrite-dominated, carbonate-rich veins—are consistent with this fluid evolution model (Candela & Holland, 1986; Audétat et al., 2000). Additionally, vein density also decreases through the four porphyry intrusions and coincides with the transition from potassic to phyllic and propylitic alteration zones (Fig. 4.10). At Saddle these later stages are marked by B-type quartz—

chalcopyrite veins (Fig. 5.3 A), and eventually by pyrite-rich D-type veins associated with sericitic alteration (Fig. 5.3 D), suggesting a shift to more acidic and oxidized fluid conditions (Lowell & Guilbert, 1970; Corbett & Leach, 1998). Overall, the relationships and spatial pattern of mineralization, vein intensity, and alteration zonation at Saddle North are consistent with global porphyry systems, where early, metal-rich potassic alteration is overprinted by progressively lower-temperature assemblages during the continued evolution of the hydrothermal system (Sillitoe, 2010; Richards, 2011).

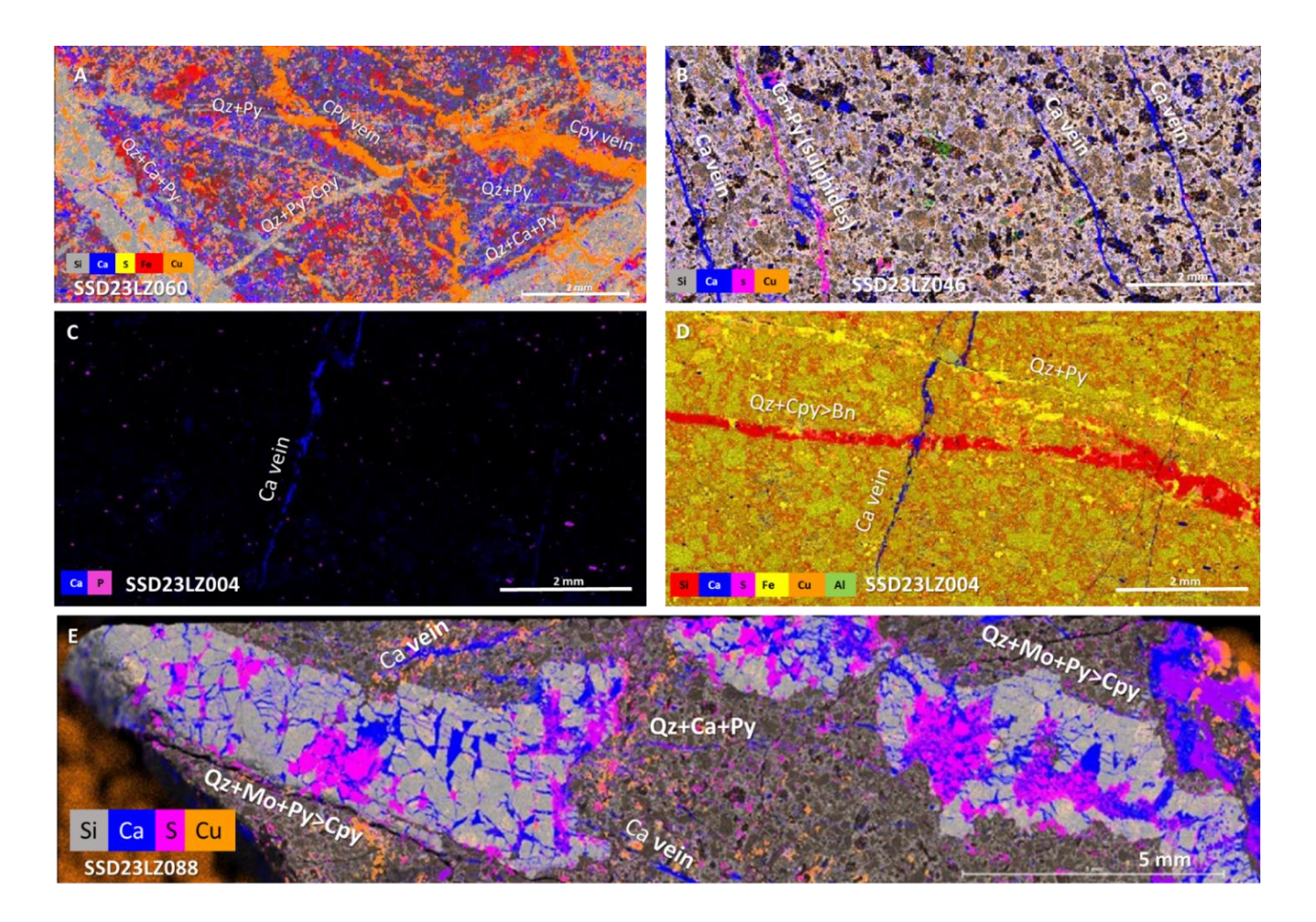


Figure 5.3. Vein-style mineralization at Saddle North associated with the FQMP intrusion phases cross-cutting vein paragenesis (μXRF image): A. FQMP-I1 intrusion Qz+Ca+Py→Qz+Py>>Cpy→Sulphide vein (Cpy) → Qz+Py (Sample SSD23LZ060, TTD-134, 826.08 m), B. FQMP-I4 intrusion carbonate+Py, carbonate vein (SSD23LZ046, TTD-093, 891 m), C and D (SSD23LZ004, TTD-109, 942.7 m). FQMP-I2 intrusion Qz+Ccp>Bn (K-feldspar more or less developed in most veins), carbonate vein, Qz+Py, and E. Stuhini group (volcanoclastic, (SSD23LZ088, TTD-128, 1350.67m) late carbonate infill quart − pyrite ± chalcopyrite (Ca vein → Qz+Ca+Oy→ Qz+PyQz+Mo+Py>>Cpy).

The feldspar quartz monzodiorite porphyry samples at Saddle (FQMP: I, II, and IV; Table 5.1) are geochemically similar to alkalic and calc-alkalic porphyry deposits in British Columbia and other regions around the world (Fig. 4.12 A). Most samples show increasing K₂O and Na₂O with SiO₂ but exhibit considerable scatter, likely the result of hydrothermal alteration (Lentz, 1996) making it challenging to use them in rock classification diagrams (i.e., total alkali-silica (TAS) diagrams). Therefore, immobile high-field strength elements (REE, Sc, Hf, Ti, Zr, Nb, Y, Ta, and Hf) have been used to determine magmatic affinities and fractionation trends for units affected by hydrothermal alteration, where the primary minerals and textures have been overprinted (MacLean and Barrett, 1993; Pearce, 1986; Gale et al., 2002; Ciftci et al., 2005; Fig. 4.12 B). According to Pearce & Cann (1973) and Wood et al. (1992), the immobile elements (e.g., Nb, Hf, Nd, Ti, Y, Zr, and REEs) exhibit low solubility during hydrothermal alteration and do not readily form mobile aqueous complexes; consequently, they are considered resistant to alteration because they are typically hosted in accessory minerals like zircon, monazite, titanite, and rutile, which are highly stable under a wide range of geological conditions (Foley et al., 2000; Klemme et al., 2006).

The intrusive rocks at Saddle North, represented by four temporally and compositionally distinct feldspar quartz monzodiorite porphyry (FQMP) phases, exhibit trace element systematics that are consistent with their origin in a subduction-related magmatic arc. Trace element patterns are characterized by systematic depletion in high field strength elements (HFSEs; Nb, Zr, and Ti) and enrichment in large-ion lithophile elements (LILEs) and light rare earth elements (LREEs), features that typify magmas derived from partial melting of a mantle wedge metasomatized by fluids released from a subducting oceanic slab (Briqueu et al., 1984; McKenzie & O'Nions, 1991; Hastie et al., 2007). These signatures are further corroborated by the presence of negative Nb anomalies and steeply fractionated REE profiles, particularly in the more evolved phases. Discrimination diagrams such as Zr/Ti vs. Nb/Y (Fig. 4.12B) place the FQMP samples within the field of subduction zone-related volcanic arc magmas, exhibiting notably low Nb/Y ratios (<0.5; Pearce & Norry, 1979; Pearce, 1996), indicative of a depleted mantle source. The trace element compositions are

also consistent with geochemical data reported for Late Triassic to Early Jurassic arc-related intrusive rocks across the Stikine terrane and adjacent regions of the Canadian Cordillera (Tatsumi et al., 1986; Wilson, 1989; Norkleberg et al., 2000; Tombe, 2016), reinforcing the interpretation that Saddle North formed within a long-lived, convergent margin setting. Additionally, the geochemical evolution within the intrusive suite reflects a progression from intermediate to more felsic compositions, characterized by increasing SiO₂ and alkali contents, and decreasing MgO, TiO₂, and compatible trace elements (e.g., V, Sc), indicating magmatic differentiation through fractional crystallization. This compositional trend is consistent with the generation of high-K calc-alkaline magmas commonly associated with fertile porphyry Cu-Au systems (Richards, 2005; Loucks, 2014). Such magmas are known to form under oxidized conditions, favourable for the transport and deposition of chalcophile metals during magmatic-hydrothermal evolution.

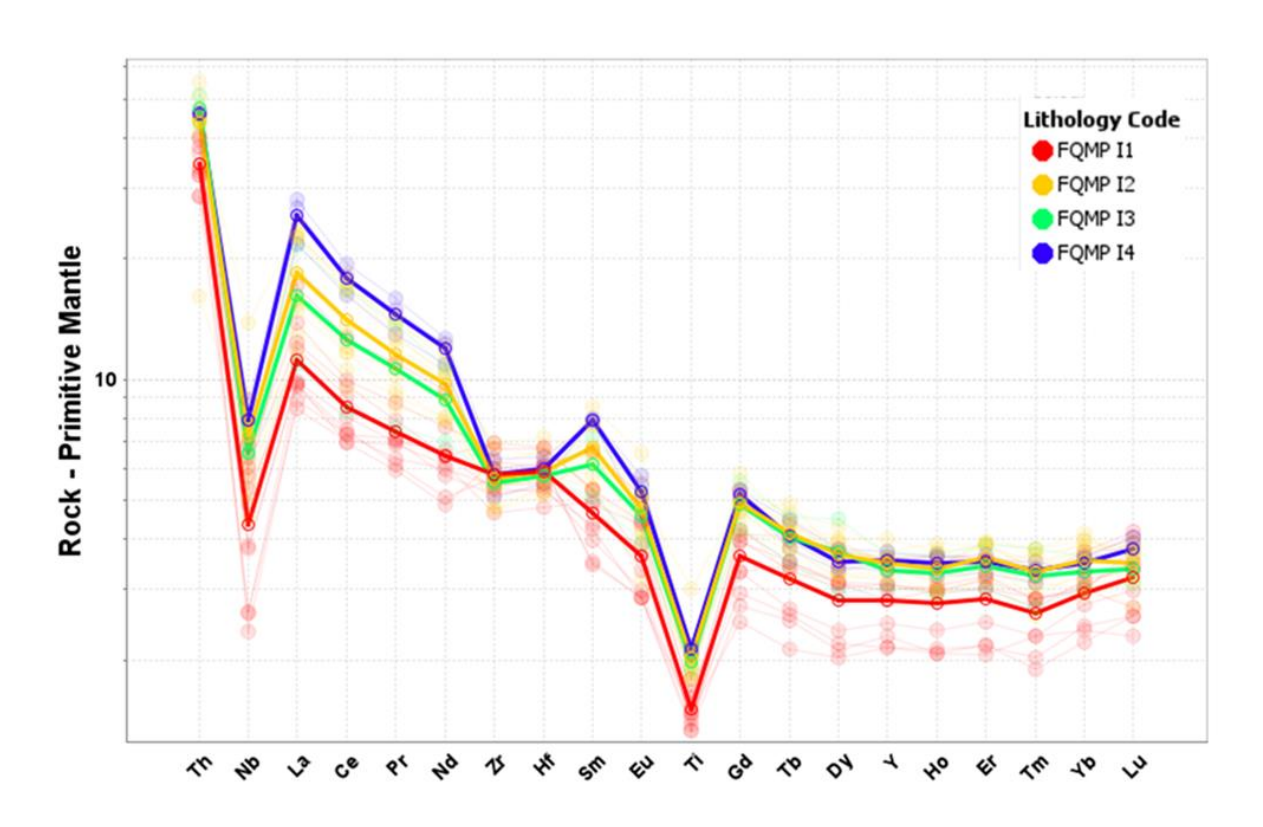


Figure 5.4. Average compositions of the four porphyry intrusion rocks from the Saddle North Project spider diagram.

Normalizing values from Sun and McDonough (1989).

Despite some overlap in major and trace element contents, particularly within discrimination diagrams, closer inspection reveals compositional variability among the FQMP phases that carries important implications for the petrogenesis and temporal evolution of the system. The geochemical differences support the interpretation that each intrusive phase represents a discrete magmatic pulse, genetically related yet emplaced at different times, each reflecting shifts in source characteristics, degrees of fractionation, and levels of crustal interaction (Fig. 5.4).

The trace element patterns observed on chondrite-normalized REE plots (Figs. 4.12; 5.4) indicate that the Saddle North intrusions are moderately enriched in LREE with weakly fractionated HREE. Samples from Saddle North, including those from the four porphyry intrusions and the volcaniclastic host rock, show high La/Sm_n ratios (1.70 – 3.95), consistent with magmas formed in a subduction zone. The Dy/Yb_n ratio can be used to assess the role of garnet in the source of melts, with depletion of heavy rare earth elements (HREEs) relative to MREEs suggesting a deeper source (Davidson et al., 2007), while lower (Dy/Yb)_n ratios (<1.5) imply a shallower source. The data for Saddle North ranges from 0.83 to 1.25, indicating a shallower mantle source (Fig. 5.5). There is a weak trend of FQMPI1 exhibiting lower values than FQMPI2, but overall the data is scattered, suggesting little variation in the source region of the four intrusive phases. Samples from the Saddle North plot in the normal andesite-dacite-rhyolite field in Figure 5.5, consistent with a mantle wedge origin rather than slab melts (Moore and Carmichael, 1998; Müntener et al., 2001; Richards and Kerrich, 2007; Richards et al., 2012; Loucks, 2014).

In addition, the REE ratios La/Sm and Gd/Yb provide insights into the petrogenetic processes that differentiate each intrusive phase and better support the comparison section between FQMP-I1 through FQMP-I4 (Fig. 5.5; Table 5.3), the geochemical distinction between intrusive phases becomes clearer. For instance, the four intrusions show similar La/Sm values but differ in Gd/Yb, which may reflect different

pressure conditions or source mineralogy during melt fractionation often associated with mineralizing intrusions (Richards & Mumin, 2013). While intermediate in both ratios, FQMP-I3 displays a flatter REE profile and lower Gd/Yb, pointing to comparatively shallower crystallization and less amphibole influence (Lee et al., 2005). Therefore, on primitive mantle-normalized incompatible element spider diagrams (Fig. 5.4), porphyry intrusion and volcanic rock at Saddle North display increasingly negative slopes between Th and La, Th and Sm, along with significant negative Nb and Ti anomalies. This suggests that geochemical variations within the rocks are primarily a result of subduction-related enrichment rather than source enrichment or crustal contamination (Fig. 5.6; Pearce & Peate, 1995; Pearce, 2008).

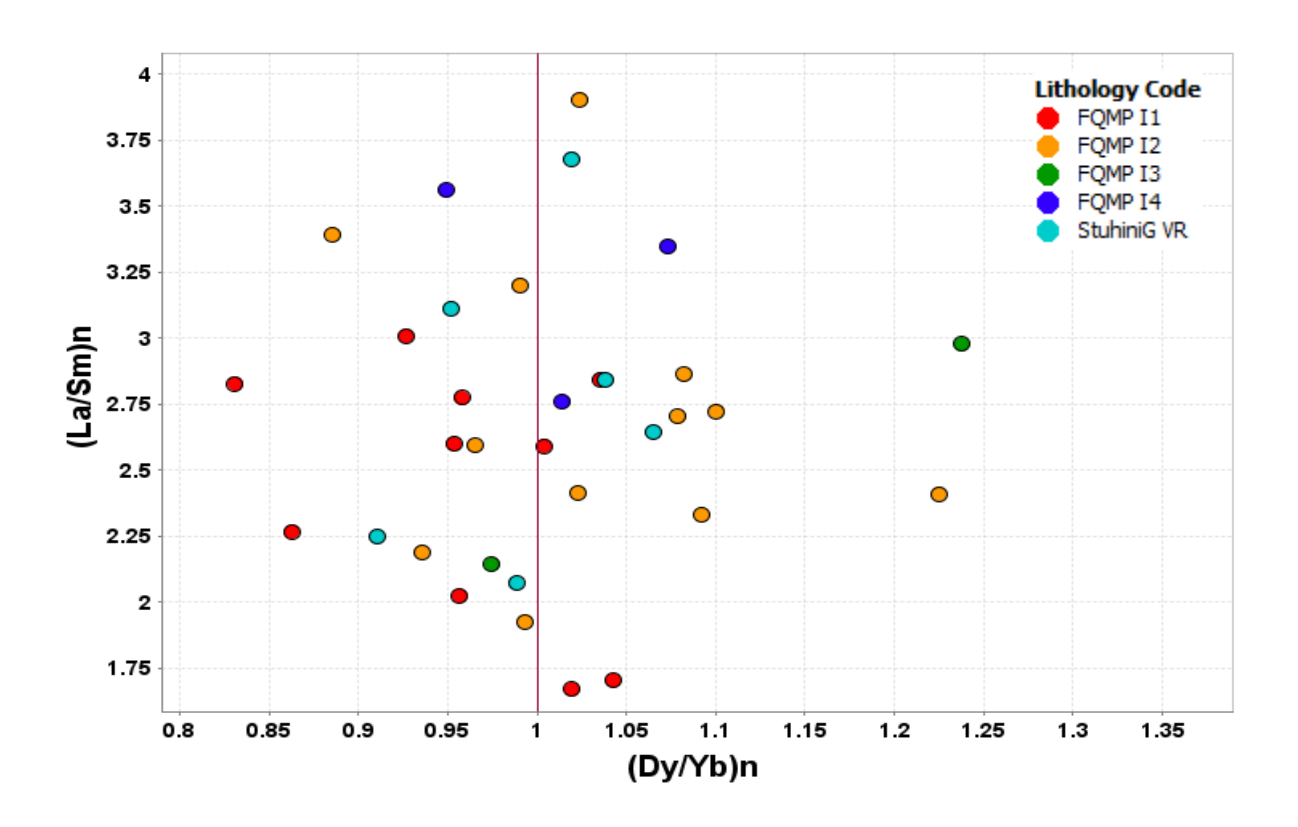


Figure 5.5. Comparison of ratios of normalized LREE/MREE (La/Sm)_n to normalized MREE/HREE (Dy/Yb)_n. The line at the value of 1 indicates a state where there is no fractionation or change in the relative abundance of these elements. Normalization values for the Saddle North porphyry deposit are sourced from Sun and McDonough (1989).

FQMP-I1 is the most geochemically evolved of the suite, characterized by high Nb/Y and Zr/TiO₂ ratios (Table 5.3), elevated LREE concentrations, and pervasive potassic alteration is predominantly associated with alkalic magma affinity. These features point to substantial fractional crystallization and likely assimilation of continental crustal components, processes typical of mature continental arcs (Richards, 2011; Bucholz & Jagoutz, 2017). In contrast, FQMP-I2 displays lower Nb/Y and Zr/TiO₂ ratios, a steep LREE profile (Table 5.3), and a subtle negative Eu anomaly. These traits suggest a relatively less evolved, mantlederived magma sourced from an oxidized sub-arc mantle wedge with limited plagioclase retention, consistent with fluid-fluxed melting beneath active subduction zones (Chiaradia, 2015; Lee et al., 2005). The FQMP-I3 exhibits the lowest Nb/Y and Zr/TiO₂ values, moderate LREE enrichment (Table 5.3), and a nearly flat HREE profile. These characteristics point to a mafic magma with minimal crustal contamination and lower degrees of differentiation, likely reflecting a direct contribution from a depleted mantle source and limited residence time in the crust. Subsequently, FQMP-I4, with an average content of SiO₂ (60.8 wt.%), probably increased by the occurrence of quartz veins, displays strong LREE enrichment coupled with a pronounced negative Eu anomaly (Table 5.3), suggesting advanced fractional crystallization in an oxidized magmatic environment. These features are often observed in late-stage, mineralizing intrusions within porphyry systems (Ballard et al., 2002; Loucks, 2021).

Table 5.3. Whole-rock geochemistry summary for the Saddle North feldspar quartz monzodiorite porphyry (FQMP) intrusion phases.

Intrusion Phase	SiO ₂ (%)	Nb/Y	Zr/TiO ₂	La/Sm	Gd/Yb	REE Pattern
FQMP-I1	58.4	0.30	0.0040	4.2	2.0	LREE-enriched
FQMP-I2	56.1	0.20	0.0035	5.1	1.9	Steep LREE, weak Eu anomaly
FQMP-I3	57.5	0.10	0.0025	3.3	1.4	Moderate LREE, flat HREE
FQMP-I4	60.8	0.25	0.0030	4.5	1.6	LREE-enriched, low Eu anomaly

Collectively, the chemical variability among the FQMP phases is indicative of a dynamic and evolving arc magmatic system, and possibly crustal assimilation (Table 5.3). These characteristics are comparable to other well-characterized Triassic–Jurassic porphyry systems within the Stikine terrane, such as GJ, Red Chris, and North Rok (Byrne, 2014; Greig, 2020), reinforcing the interpretation that Saddle North formed in a similar tectonomagmatic regime marked by arc maturation and episodic thermal pulses. Additional understanding is gained from tectonic discrimination plots such as Nb/Yb vs. Th/Yb (Pearce & Peate, 1995), which position the Saddle North samples between the oceanic and continental arc fields (Fig. 5.6). This transitional affinity is consistent with magmas derived from a lithospheric mantle source modified by slab-derived fluids, and potentially assimilating lower crustal material during ascent and storage (Logan, 2005; 2014; Richards, 2011). Enrichment in LILEs and moderate depletion in HFSEs and Ti provide additional support for subduction-related metasomatism as a key process influencing the source region.

Although geochemical differences among phases do exist, petrographic and hydrothermal alteration assemblages are broadly similar across the suite. This suggests that the subsequent thermal and fluid

regimes associated with the porphyry system overprinted magmatic heterogeneities to a significant degree. Such convergence in alteration styles implies that despite compositional differences among the magmas, the physicochemical conditions responsible for hydrothermal activity and mineralization were recurrent or overlapping in time, consistent with models of sustained magmatic-hydrothermal systems (Sillitoe, 2010; Seedorff et al., 2005). Even though similar alteration styles suggest that mineralization was not tied to a single intrusion but rather to a composite magmatic system characterized by multiple fertile pulses, this aligns with models proposed for other porphyry Cu-Au deposits in the Stikine terrane, such as Red Chris and GJ-Donnelly property, where successive intrusion events and evolving magmatic conditions were critical to ore formation (Byrne, 2014; Greig, 2020). Thus, coincident with a regional metallogenic pulse documented throughout the northern Stikine arc (Mortensen et al., 1995; Logan & Mihalynuk, 2014). This timing reinforces the interpretation of Saddle North as part of a broader tectonomagmatic episode linked to subduction-driven arc magmatism, crustal thickening, and fluid-fluxed mantle melting. Together, the geochemical, petrographic, and temporal evidence support a model in which multiple intrusive events, derived from a variably evolved arc magma source, contributed to the formation of a fertile porphyry system within a dynamic accretionary arc framework.

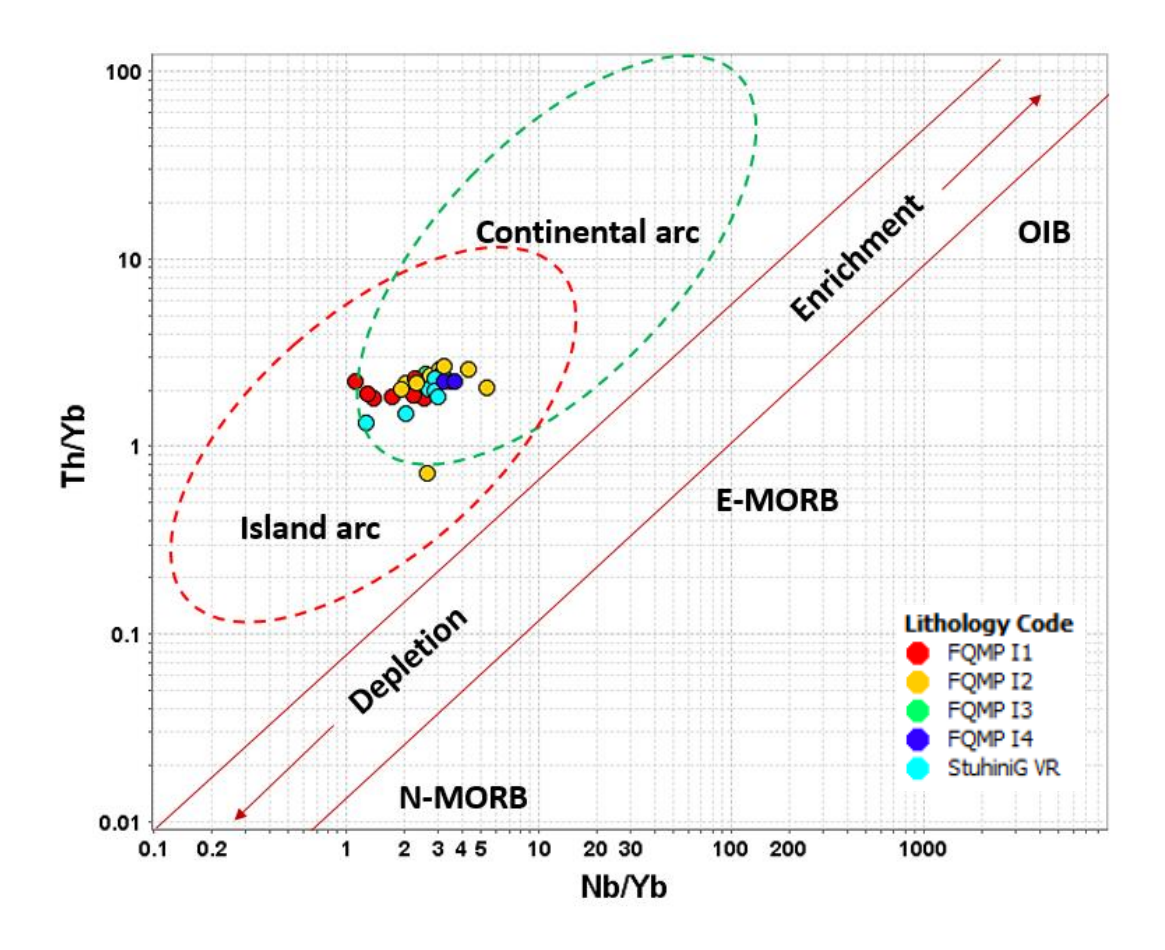


Figure 5.6. Plot of Nb/Yb-Th/Yb for intrusions of the Saddle North deposit (Pearce & Peate, 1995).

Given the compositional trends in Figure 5.7, the Saddle North porphyry intrusions align with the interpretations by Loucks (2014), showing a strong clustering of the samples within the "Normal andesite-dacite-rhyolite rocks" field, characterized by relatively low La/Yb ratios (generally below 15; Fig. 5.7) and Yb concentrations (ranging from approximately 1.0 to 2.25 ppm; Fig. 5.7), suggests that the parental magmas for this porphyry system were not predominantly adakitic. Nevertheless, the majority of samples fall within the "Normal andesite-dacite-rhyolite" field, it is important to note the presence of a few samples that trend towards the lower end of the "Adakite-like rocks" field, particularly FQMP I4 and StuiniG VR. Although these do not fully enter the adakitic field as defined by Loucks (2014), their slightly elevated La/Yb values compared to the bulk of the data might suggest minor contributions from processes

that could lead to adakite-like signatures, such as limited interaction with a garnet-bearing source or early fractional crystallization of amphibole (Mao et al., 2017). However, the dominant trend clearly indicates a non-adakitic affinity for the main magmatic suite. Furthermore, the occurrence of normal arc magmas in porphyry settings is well documented (e.g., Richards, 2011; Chiaradia et al., 2012). These magmas effectively transport metals and fluids from the mantle into the shallow crust, creating fertile environments for porphyry mineralization. The characteristics of the Saddle North samples, plotting firmly within the normal andesite-dacite-rhyolite field, are thus entirely consistent with a typical arc-related porphyry deposit.

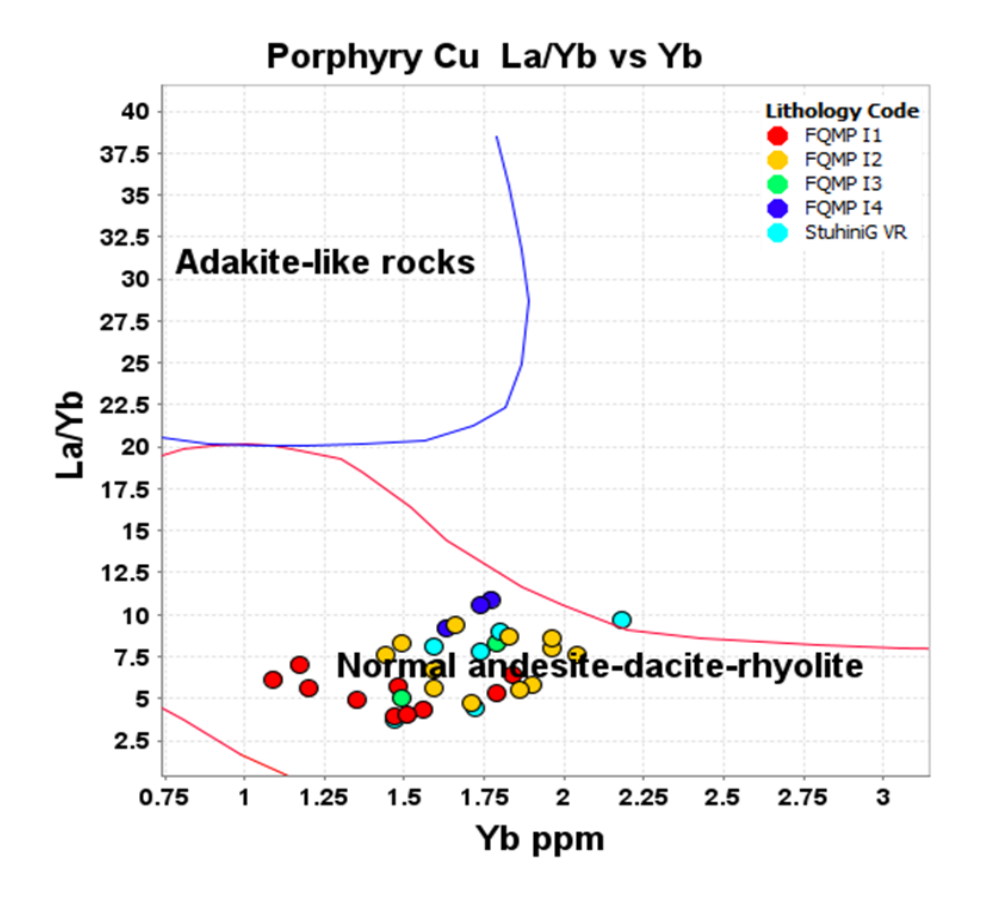


Figure 5.7. Binary diagrams showing the concentration variation of La/Yb against Yb. Composition of Adakite-like rocks and normal andesite-dacite-rhyolite rocks for the Saddle North porphyry deposit for the Saddle North porphyry deposit (Loucks, 2014).

The new U-Pb zircon geochronological results from Saddle North provide critical insight into the timing of emplacement and crystallization of the quartz-feldspar monzodiorite porphyry (FQMP) phases and their volcanic host rocks. LA-ICP-MS dating of the four FQMP intrusive phases yielded crystallization ages that cluster tightly between 205 and 208 Ma: FQMP-I1 (205.3 ± 1.7 Ma), FQMP-I2 (average 208.2 ± 1.8 Ma), FQMP-I3 (206.8 \pm 1.9 Ma), and FQMP-I4 (average 205.3 \pm 2.2 Ma) (Fig. 5.8). These overlapping ages, all within analytical error (Table 5.1), suggest that the intrusive activity at Saddle North occurred over a relatively short time span, consistent with a single, temporally focused magmatic-hydrothermal system. This brief magmatic duration supports a model in which the emplacement of porphyritic intrusions, hydrothermal fluid evolution, and ore formation occurred in close temporal proximity. This interpretation is further supported by a Re-Os molybdenite age of 205 ± 0.8 Ma (Table 4.2), obtained from pyritechalcopyrite-bearing quartz-carbonate veins (Fig. 5.3E), which aligns with the zircon ages of the FQMP intrusions, particularly FQMP-I1, albeit slightly younger within uncertainty. These results align well with numerous studies that document similarly short-lived magmatic-hydrothermal evolution in porphyry systems globally (e.g., Cathles et al., 1997; Masterman et al., 2004; von Quadt et al., 2011; Chiaradia et al., 2013; Rees et al., 2015; Correa et al., 2016; Li et al., 2017). Moreover, high-resolution ID-TIMS dating, currently in progress, may further refine the timing between intrusive pulses and hydrothermal mineralization and help resolve whether the FQMP phases represent a single evolving magma body or closely spaced, compositionally distinct intrusions.

The concordia plots (Fig. 4.14 A and B), show a tightly constrained population of concordant zircons in the feldspar-quartz-monzodiorite porphyry samples, suggesting rapid crystallization during a single magmatic event. In contrast, slightly greater age dispersion and minor discordance in the diorite sample may indicate a more complex magmatic history, potentially involving zircon inheritance or limited post-crystallization Pb loss, (Brodbeck, 2022). The new U-Pb zircon ages presented here are broadly consistent with previously published data from the Saddle North intrusive complex. Zircon ages in this study span from 206.2 ± 1.8

Ma (oldest phase, FQMP-I1) to 202.0 ± 1.5 Ma (youngest phase, FQMP-I4). These fall within the uncertainty of the previously reported U-Pb zircon age of 206.2 ± 1.8 Ma by Greig (2021), which represents a single age determination from samples collected across several monzonites to monzodiorite porphyry phases on the Tatogga property. Together, geochronological data confirm that mineralization at Saddle North was temporally associated with a relatively narrow magmatic window during the Late Triassic to Early Jurassic transition—a period also recognized as metallogenically fertile throughout the Stikine terrane (Logan & Mihalynuk, 2014; Nelson & Colpron, 2007).

Re-Os molybdenite dating conducted on two vein samples from the Saddle North deposit yielded ages of 207.8 \pm 0.9 Ma and 204.2 \pm 0.9 Ma (Greig, 2021). These ages overlap with the timing of intrusion emplacement, suggesting that mineralization occurred shortly after the crystallization of the host porphyritic phases and the overlapping timing of magmatic and hydrothermal events supports the interpretation of a genetically linked porphyry system active during the Late Triassic broadly consistent with Galore Creek deposit crystallization ages of 210.2 \pm 1.0 Ma (U-Pb, titanite; Mortensen et al., 1995) and Red Chris (U-Pb, zircon; 203.8 \pm 1.3 Ma; Friedman & Ash, 1997), suggesting that porphyry mineralization in the region was constrained to a relatively narrow window. The ages for Saddle North are also broadly consistent with the previously reported ages for porphyry Cu-Au deposits related to arc uplift and erosion across the northern Stikine arc that were formed through multiple distinct events between 210 and 200 million years ago during the late Triassic to early Jurassic (Mortimer 1987), Mortensen et al. (1995) and Logan et al. (2007).

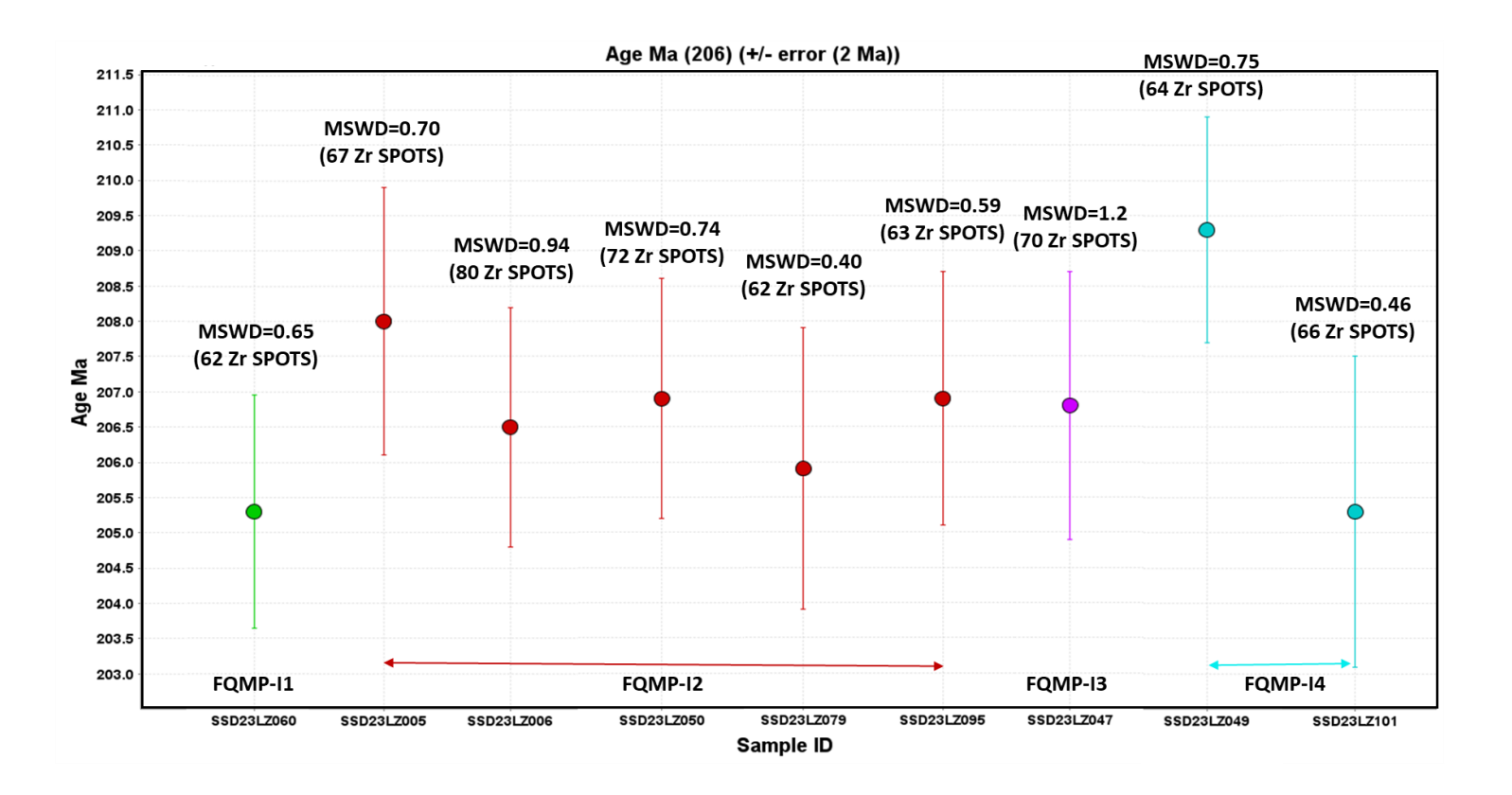


Figure 5.8. FQMP-I1 (green color), FQMP-I2 (red color), FQMP-I3 (magenta color), and FQMP-I4 (light blue color). Compilation of geochronology data from the Saddle North area.

Petrographic analysis reveals that the intrusive complex at Saddle North comprises at least four compositionally and texturally distinct porphyritic phases (FQMP-I1 to FQMP-I4). These phases range from monzodiorite to monzonite and are dominated by plagioclase, orthoclase, hornblende, biotite, and minor quartz, with textures ranging from hypidiomorphic to porphyritic. Each phase exhibits variable phenocryst assemblages and degrees of hydrothermal alteration, which provide valuable constraints on the magmatic evolution and timing of mineralization. FQMP-I1 is marked by abundant sericitized plagioclase and moderate K-feldspar content, suggesting early crystallization followed by intense sericitic overprinting. FQMP-I2 is characterized by well-developed hornblende and biotite, indicative of a more mafic, possibly volatile-rich pulse. FQMP-I3 has a finer-grained groundmass dominated by K-feldspar, consistent with rapid cooling or shallower emplacement. Finally, FQMP-I4 shows the least alteration and best

preservation of primary feldspars, pointing to a late, relatively unaltered phase. These mineralogical and textural differences are summarized in Table 5.1 and Appendix B. The intrusive phases are hosted by the volcanic and volcaniclastic rocks of the Stuhini Group, which are predominantly composed of basaltic to andesitic flows and fine-grained volcaniclastic rocks. The country rocks have undergone variable quartz-sericite and carbonate-clay alteration and commonly contain disseminated pyrite and chalcopyrite.

The spatial and temporal relationships between intrusive contacts, hydrothermal alteration zones, and vein generations at Saddle North provide critical insights into the evolution of the magmatic-hydrothermal system. The emplacement of successive intrusive phases (FQMP-I1 to FQMP-I4) was closely accompanied by distinct alteration styles, indicating dynamic fluid-rock interactions that evolved alongside the magmatic system (Table 5.2). Potassic alteration is the most extensive and mineralization-associated alteration style, characterized by secondary biotite, magnetite, and K-feldspar replacement in both intrusive rocks and adjacent volcanic host rocks (Fig. 5.3). This alteration is particularly well developed near the cores of FQMP-I1 and FQMP-I2 intrusions, consistent with models of early, high-temperature fluid exsolution from crystallizing arc magmas (e.g., Sillitoe, 2010). The strong spatial association between potassic zones and early-stage mineralized veins (e.g., quartz ± magnetite ± sulphide) further supports their genetic link to the most fertile magmatic pulses.

Subsequent overprinting by phyllic (quartz-sericite) and propylitic assemblages reflects the downward and lateral migration of lower-temperature, more oxidized fluids as the system cooled and evolved. Propylitic alteration, dominated by chlorite, epidote, and carbonates, is widespread in both intrusions and host volcanic rocks, suggesting peripheral and late-stage fluid pathways. In contrast, phyllic alteration is more localized and commonly developed around later-stage veins, particularly in structurally controlled zones, implying episodic reactivation and renewed fluid flow. This paragenetic evolution of vein types at Saddle North further supports a multi-stage hydrothermal system that evolved in concert with magmatic activity. Early-stage veins, containing quartz ± magnetite ± sulphide assemblages (chalcopyrite, pyrite,

molybdenite, bornite), are temporally associated with strong potassic alteration, indicating precipitation from high-temperature, metal-rich magmatic fluids. These veins are crosscut by main-stage assemblages of quartz ± chalcopyrite ± magnetite ± carbonate, in which recrystallized quartz and magnetite-rich margins suggest dynamic conditions of vein growth and fluid evolution, as well as late-stage veins, dominated by quartz-pyrite-chalcopyrite and carbonate-pyrite assemblages, are strongly associated with phyllic alteration halos and reflect a cooler, more oxidized fluid regime. Finally, post-mineralization carbonate veins with minor sulphide content crosscut all earlier vein types, marking the terminal phase of fluid activity. The relative timing and crosscutting relationships of these veins—observed in both core and thin sections—provide a robust framework for reconstructing the hydrothermal evolution and link each paragenetic stage to specific intrusive events (Table 5.2; Fig. 4.10). Collectively, these suggest that each intrusive phase contributed to the progressive evolution of the hydrothermal system.

Whole-rock geochemical data from 35 samples, including both intrusive and host rock types, reveal a consistent magmatic signature. The intrusive rocks exhibit SiO₂ contents ranging from 52 to 61 wt% and are classified as monzonite to monzodiorite (Fig. 4.11 A), with alkalic to calc-alkalic affinities (Table 5.3). Trace element discrimination diagrams show moderate to strong negative Nb and Ti anomalies, alongside minor anomalies in Zr, Hf, and Eu, signatures typical of subduction-related arc magmas (Fig. 4.12). The intrusions are enriched in light REEs (LREE) over heavy REEs (HREE), consistent with fractional crystallization and a mantle-derived, oxidized magmatic source (Fig. 4.12). The geochemical homogeneity across intrusive phases supports a genetic relationship and supports the single mineralizing system hypothesis. Significantly, the effects of alteration, particularly potassic, on mobile elements like Na and K are noted, indicating that major element-based discrimination diagrams must be interpreted cautiously in altered rocks. LA-ICP-MS U-Pb zircon dating and Re-Os molybdenite geochronology confirm a tightly constrained magmatic-hydrothermal evolution between 205.3 and 208.2 Ma (Fig. 5.8; Table 4.2). These data suggest that most magmatism and associated hydrothermal activity occurred over a relatively short

interval during the Late Triassic to Early Jurassic transition. The Re-Os molybdenite age from a mineralized quartz vein yielded an age of 205.6 ± 0.8 Ma, overlapping with the zircon crystallization ages and indicating that ore formation coincided with late-stage magmatism and K-feldspar alteration.

Even though the Saddle North porphyry deposit shares several key geological features with other major porphyry systems in British Columbia's Stikine Terrane, such as Galore Creek, Red Chris, GJ, and North Rok, it also displays distinct characteristics. All these deposits, including Saddle North, are associated with calc-alkaline to high-K calc-alkaline intrusive rocks emplaced during the Late Triassic to Early Jurassic, reflecting subduction-related magmatism (Grieg, 2020; Micko et al., 2014; Table 5.4). The intrusive complex at Saddle North consists of four distinct monzonitic to monzodioritic porphyry phases that have hypidiomorphic textures and exhibit strong potassic alteration overprinted by phyllic and propylitic assemblages. These features are comparable to those at Red Chris, where multiphase intrusions also experienced pervasive K-silica alteration and cross-cutting quartz–sulphide veining (Micko et al., 2014; Table 5.4). The key difference between assemblages and those observed at Red Chris is in the spatial distribution of mineralization and geometry. At Red Chris, ore zones form a vertically extensive, pipe-like body (Micko et al., 2014), whereas at Saddle North mineralization is concentrated within a stockwork, and the vein paragenesis shows a well-defined evolution, from early quartz–magnetite sulphide assemblages toward later carbonate-dominated veins, reflecting changes in fluid composition and temperature over the life of the hydrothermal system (Grieg, 2020).

The difference in geometry likely reflects contrasting structural and emplacement controls. At Saddle North, mineralization appears strongly influenced by pre-existing structural zones that localized intrusion emplacement and subsequent hydrothermal fluid flow. These structures helped mineralized zones rather than vertically continuous pipe-shaped bodies. In contrast, the Red Chris geometry may result from more centralized intrusion emplacement upward fluid flow. Such variations in geometry are important for

understanding ore distribution, exploration targeting, and potential mining methods in alkalic porphyry systems (Holliday & Cooke, 2007; Sillitoe, 2010).

Table 5.4. Comparison of major features of the Saddle North, the Galore Creek and Red Chris Porphyry Deposits. Modified after Micko et al. (2014) and GT Gold Corps (2020).

Feature	Saddle North	Red Chris	Galore Creek	GJ	North Rok
Location	NW British Columbia	NW British Columbia	NW British Columbia	NW British Columbia	NW British Columbia
Host Lithology	Monzonite– monzodiorite (FQMP-I1 to I4)	Quartz monzodiorite- monzonite	Syenite- monzonite	Quartz monzodiorite	Monzonite- monzodiorite
Intrusion Texture	Porphyriticto hypidiomorphic	Porphyritic	Coarse-grained to porphyritic	Porphyritic	Porphyritic
Age (U-Pb/Re- Os)	206–202 Ma (zircon); 208–204 Ma (Re-Os)	204–198 Ma (zircon & Re-Os)	~204–202 Ma (U- Pb zircon; Logan et al.)	~201 Ma (U-Pb zircon)	~204 Ma (U-Pb zircon)
Alteration Assemblages	Potassic → Phyllic → Propylitic	Potassic → Phyllic → Argillic	Strong potassic core with peripheral propylitic	Potassic → Phyllic → Propylitic	Potassic → Phyllic
Sulphide Minerals	Chalcopyrite, pyrite, bornite	Chalcopyrite, bornite, magnetite, pyrite	Chalcopyrite, bornite, pyrite	Chalcopyrite, pyrite, molybdenite	Chalcopyrite, pyrite
Mineralization Style	Stockwork veins + disseminations	Stockwork, disseminated + breccias	Stockwork, disseminations, breccias	Stockwork + disseminations	Stockwork+ disseminated
REE Signature	LREE-enriched, Eu anomaly (variable)	LREE-enriched, moderate Eu anomaly	Strong LREE enrichment, Eu anomaly	LREE-enriched, minor Eu anomaly	LREE-enriched
Geochemical Affinity	High-K calc- alkaline to transitional	High-K calc- alkaline	Alkalic to high-K calc-alkaline	High-K calc- alkaline	High-K calc-alkaline
Tectonic Setting	Arc-related, evolving arc on composite crust	Arc setting, subduction-related	Alkalicarc in extensional back- arc context	Arc-related	Arc-related

Chapter 6. Conclusions

This study aimed to describe the lithology, alteration, vein types, and copper-gold bearing units to construct a paragenesis for the Saddle North porphyry deposit system in British Columbia, enhancing our understanding of the system's genesis and the evolution of alkali Cu-Au porphyry deposits in the region. The Saddle North deposit is hosted in lower Triassic sedimentary rocks, alongside marine volcanic and sedimentary rocks of the middle to upper Triassic Stuhini Group (Logan & Koyanagi, 1994). Within the intrusive complex, four principal porphyry units (monzonite-monzodiorite) intrude the host rock at varying stages, accompanied by associated hydrothermal activity. These monzodiorites are differentiated based on composition, alteration intensity, and crosscutting relationships.

Mineralization in the Saddle North porphyry copper gold deposit occurs genetically related to porphyrystyle stockwork veining density and the intensity of potassic alteration. The mineralization is closely associated with potassic alteration, which primarily occurs in the monzonite and monzodiorite (plagioclase-hornblende-biotite porphyry). The primary Cu-Au ore minerals are pyrite, chalcopyrite, and minor bornite, which are mainly found in quartz-sulphide veins but also occur as disseminations within the altered porphyry. The intrusive phases share not only similar emplacement ages but also comparable lithological, geochemical, and alteration characteristics, suggesting their formation during a widespread Late Triassic to Early Jurassic magmatic episode associated with subduction-driven arc evolution and crustal thickening in the Stikine terrane (Table 5.4). The temporal and geological coherence among these deposits underscores a shared tectonomagmatic context. It reinforces the interpretation of Saddle North as part of a larger porphyry metallogenic belt in northwestern British Columbia. This timing is comparable to other major porphyry Cu-Au deposits in the region, such as Red Chris, GJ, and North Rok, which exhibit similar mineralization styles, alteration patterns, and geochemical signatures (Greig, 2020; Logan & Mihalynuk, 2014; Mortensen et al., 1995; Table 5.4).

The vein paragenesis at Saddle North can be classified into eight types. Early vein types (Qz+Mg+Py+Cpy, A-veins, and B-veins) are closely related to strong K-feldspar alteration. These early veins are temporally and spatially linked to stage 1 of the hydrothermal alteration (the early mineralization event), reflecting the main event of the mineralized intrusions based on the sulphides assemblage (Py, Cp >Mo>>Bn) and quartz vein density could signify nearby high-grade zones. Variation of grades is associated with pyrite and chalcopyrite contained within Qz+K-feldspar+Py, Py veins, and D-veins, as the intermediate to weak potassic alteration gradually reduces in intensity. The late and post-mineralization stage carbonate veins are associated with sericite-carbonate, consistent with phyllic alteration present in nearly all the veins observed throughout the system. This distribution and the cross-cutting relationships of these vein types at Saddle North reflect a temporal evolution from early potassic alteration and copper-rich sulphide deposition to a later phyllic overprint, mirroring patterns documented in well-studied porphyry systems globally (e.g., Gustafson & Hunt, 1975; Sillitoe, 2010).

The intrusive units have been dated at FQMP-I1 205.3 \pm 1.7, FQMP-I2 (208.0 - 205.9) \pm 1.8, FQMP-I3 206.8 \pm 1.9, and FQMP-I4 (209.3 - 205.3) \pm 1.9 Ma. (Fig. 5.8). The new geochronological data obtained in this study are consistent with magmatism during the Late Triassic-Early Jurassic (~203-193 Ma) that is widespread in British Columbia (Schiarizza et al., 2009; Logan et al., 2011; Blackwell et al., 2012a) and is interpreted to be related to subduction along the western margin of North America. This timing aligns with other calc-alkaline porphyry Cu-Mo-(Au) deposit ages in the Stikine arc in British Columbia (Scott et al., 2008). Additionally, the Re-Os molybdenite age of 205.6 \pm 0.8 Ma from a mineralized quartz vein demonstrates a consistent association between crystallization and mineralization ages, reinforcing the idea of synchronous mineralization and intrusion emplacement. However, further geochronological studies are needed to refine the dating results and test the timing relationships of the intrusive phases and link these to alteration intensity, and vein architecture timing in controlling the distribution and grade of mineralization within the deposit.

In terms of implications for exploration, the consistent intrusive compositions (ranging from monzodiorite to monzonite), calc-alkaline to high-K calc-alkaline affinities, and synchronized emplacement timing observed across these deposits strongly suggest the presence of a laterally extensive and temporally coherent metallogenic belt. The specific geochemical fingerprints of the Saddle North intrusions characterized by enrichment in LREEs, depletion in Nb and Ti, and transitional arc signatures similar to those documented in other fertile porphyry systems that formed under compressional tectonic regimes with active crustal thickening (Chiaradia, 2015; Richards, 2011). This reinforces the interpretation that the Stikine terrane hosted a series of magma pulses with inherent high fertility potential, capable of generating large-scale mineralized systems when favourable structural and lithological conditions were met. Therefore, the integrated geological, geochemical, and geochronological characteristics of the Saddle North system not only firmly validate its classification as a classic porphyry Cu-Au deposit but also establish its importance as a key reference point for guiding future exploration efforts in northwestern British Columbia. A comprehensive understanding of its spatial and temporal relationships with other porphyry centers within the Stikine arc is crucial for developing refined regional targeting strategies, particularly in currently underexplored areas sharing similar basement architecture and magmatic histories.

References

Audétat, A. (2010). Source and evolution of magmatic-hydrothermal fluids. Geofluids, 10(1-2), 263-279.

Alldrick, D. J., Stewart, M. L., Nelson, J. L., & Simpson, K. A. (2004). Tracking the Eskay Rift through northern British Columbia-geology and mineral occurrences of the Upper Iskut River area. British Columbia Ministry of Energy and Mines, 2004-1.

Audétat, A. (2010). Source and evolution of magmatic-hydrothermal fluids. Geofluids, 10(1-2), 263-279. https://doi.org/10.1111/j.1468-8123.2010.00284.x

Barker, R. D., Barker, S. L., Wilson, S., & Stock, E. D. (2020). Quantitative Mineral Mapping of Drill Core Surfaces I: A Method for μ XRF Mineral Calculation and Mapping of Hydrothermally Altered, Fine-Grained Sedimentary Rocks from a Carlin-Type Gold Deposit. Economic Geology, 116(4), 803-819.

Blackwell, J., MacIntyre, D., & Villeneuve, M. (2012a). New U–Pb zircon geochronology from the Stikine Terrane, British Columbia: Constraints on magmatism and terrane evolution (Geological Survey of Canada, Open File). Natural Resources Canada.

Bruker, (2018), M4 Tornado: 2D Micro-XRF with ultimate speed and accuracy, (https://www.bruker.com/products/x-ray-diffraction-and-elemental-analysis/micro-xrf-and-txrf/m4- tornado/overview.html).

Chiaradia, M. (2015). Copper enrichment in arc magmas controlled by overriding plate thickness. Nature Geoscience, v. 8, no. 3, 215–219.

Chiaradia, M., Schaltegger, U., Spikings, R., Wotzlaw, J.-F., and Ovtcharova, M., (2013), How accurately can we date the duration of magmatic-hydrothermal events in porphyry systems? — an invited paper: Economic Geology, 108, 565–584.

Cooke, D. R., Agnew, P., Hollings, P., Baker, M., Chang, Z., Wilkinson, J. J., & Chen, H. (2020). Recent advances in the application of mineral chemistry to exploration for porphyry copper–gold–molybdenum deposits: detecting the geochemical fingerprints and footprints of hypogene mineralization and alteration. Geochemistry: Exploration, Environment, Analysis, 20(2), 176–188.

Farmer, G. L., Glazner, A. F., Kortemeier, W. T., Cosca, M. A., Jones, C. H., Moore, J. E., & Schweickert, R. A. (2013). Mantle lithosphere as a source of postsubduction magmatism, northern Sierra Nevada, California. Geosphere, 9(5), 1102-1124.

Febbo, G. E., Kennedy, L. A., Nelson, J. L., Savell, M. J., Campbell, M. E., Creaser, R. A., ... & Stein, H. J. (2019). The evolution and structural modification of the supergiant Mitchell Au-Cu porphyry, northwestern British Columbia. Economic Geology, 114(2), 303-324.

Flude, S., Haschke, M., & Storey, M. (2017). Application of benchtop micro-XRF to geological materials. Mineralogical Magazine, 81(4), 923-948.

Foley, S. F., Tiepolo, M., & Vannucci, R. (2000). Growth of early continental crust controlled by melting of amphibolite in subduction zones. Nature, 406(6792), 104–107.

Fryer, B. J., Jackson, S. E., & Longerich, H. P. (1993). The application of laser ablation microprobe-inductively coupled plasma-mass spectrometry (LAM-ICP-MS) to in situ (U) Pb geochronology. Chemical Geology, 109(1-4), 1-8. G.T. Gold Corporation Ltd. Mineral Resource Statement, Saddle North Copper Gold Project Technical Report N.I. 43-101 – August 20, 2020, Canada.

G.E. O'Brien J. (1991). Cordilleran terranes, Part B. In Geology of the Cordilleran Orogen in Canada. Edited by Gabrielse H. Yorath C.J. Geological Society of America, The Geology of North America, Vol. G-2, pp. 281–327.

Greig, C. J., Dudek, N. P., ver Hoeve, T. J., Newton, G., & Greig, R. E. (2021). Geology of the Tatogga property: Geologic framework for the Saddle North porphyry Cu-Au deposit and the Saddle South epithermal Au-Ag vein system, Iskut district, northwestern British Columbia, in Geological Fieldwork 2020: British Columbia Ministry of Energy, Mines and Low Carbon Innovation: British Columbia Geological Survey Paper 2021-01.

Kesler, S. E., Chryssoulis, S. L., & Simon, G. (2002). Gold in porphyry copper deposits: its abundance and fate. Ore Geology Reviews, 21(1-2), 103-124.

Klemme, S., van der Laan, S. R., & Mezger, K. (2006). The influence of high field strength elements on partial melting of eclogite. Chemical Geology, 234(3–4), 251–263.

Lang, J.R., Stanley, C.R., and Thompson, J.F.H., (1995), Porphyry copper-gold deposits related to alkalic igneous rocks in the Triassic-Jurassic arc terranes of British Columbia: Arizona Geological Society Digest 20, p. 219–236.

Lawley, C. J., Petts, D. C., Lee, W. S., Cajal, Y., Carrasco-Godoy, C., Campbell, I., ... & van Straaten, B. (2025). Critical raw material potential of porphyry copper—gold deposits in the golden triangle, British Columbia, Canada. Ore Geology Reviews, 106463.

Layton-Matthews, D., & McClenaghan, M. B. (2021). Current Techniques and Applications of Mineral Chemistry to Mineral Exploration; Examples from Glaciated Terrain: A Review. Minerals, 12(1), 59.

Lentz, D.R., 1996. Trace element systematics of felsic volcanic rocks associated with massive-sulfide deposits in the Bathurst mining camp: Petrogenetic, tectonic and chemostratigraphic implications for VHMS exploration, Geological Association of Canada Short Course Notes, pp. 359-402.

Liu, X., Sun, M., Zhao, G., Li, D., & Wang, Y. (2018). Geochemistry and tectonic setting of the metabasites from the Paleoproterozoic Jiao–Liao–Ji Belt: Implications for the tectonic evolution of the North China Craton. Geosciences, 8(7), 266. https://doi.org/10.3390/geosciences8070266

Logan, J. M., & Mihalynuk, M. G. (2014). Tectonic controls on early Mesozoic paired alkaline porphyry deposit belts (Cu-Au ± Ag-Pt-Pd-Mo) within the Canadian Cordillera. Economic Geology, 109(4), 827–858.

Logan, J. M., & Mihalynuk, M. G. (2014). Tectonic controls on early Mesozoic paired alkaline porphyry deposit belts (Cu-Au±Ag-Pt-Pd-Mo) within the Canadian Cordillera. Economic Geology, 109(4), 827-858.

Logan, J.M., 2005, Alkaline magmatism and porphyry Cu-Au deposits at Galore Creek, northwestern British Columbia: B.C. Ministry of Energy, Mines and Petroleum Resources, Paper 2005-1, p. 237–248.

Loucks, R. R. (2014). Distinctive composition of copper-ore-forming arc magmas. Australian Journal of Earth Sciences, 61(1), 5–16, 165-168.

Lowenstern, J. B. (2015). Quartz solubility in the $H_2O-NaCl$ system: A framework for understanding vein formation in porphyry copper deposits. Economic Geology, 110(8), 1835–1840. https://doi.org/10.2113/econgeo.110.8.1835

MacLean, W., Barrett, T., (1993). Lithogeochemical techniques using immobile elements. Journal of Geochemical Exploration, 48(2): 109-133.

Masterman, G.J., Cooke, D.R., Berry, R.F., Clark, A.H., Archibald, D.A., Mathur, R., Walshe, J.L., and Durán, M., (2004). 40Ar/39Ar and Re-Os geochronology of porphyry copper-molybdenum deposits and related coppersilver veins in the Collahuasi district, northern Chile: Economic Geology, v. 99, p. 673–690.

McKenzie, D. A. N., & O'Nions, R. K. (1991). Partial melt distributions from inversion of rare earth element concentrations. Journal of petrology, 32(5), 1021-1091.

Micko, J., Tosdal, R. M., Bissig, T., Chamberlain, C. M., & Simpson, K. A. (2014). Hydrothermal alteration and mineralization of the Galore Creek alkalic Cu-Au porphyry deposit, northwestern British Columbia, Canada. Economic Geology, 109(4), 891–914.

Middlemost, E. A. (1994). Naming materials in the magma/igneous rock system. Earth-Science Reviews, 37(3-4), 215-224.

Miller, E. A., & Smyth, C. P. (2015). Geological, geophysical and geochemical program, Tatogga Lake Property, Northwest British Columbia (Informe de evaluación No. 35329). British Columbia Ministry of Energy, Mines and Petroleum Resources.

Monger, J.W.H., Price, R.A., and Tempelman-Kluit, D.J., (1982). Tectonic accretion and the origin of two metamorphic and plutonic welts in the Canadian Cordillera. Geology, 10, 70-75.

Monger J.W.H. Wheeler J.O. Tipper H.W. Gabrielse H. Harms T. Struik L.C. Campbell R.B. Dodds C.J. Gehrels G.E. O'Brien J. (1991). Cordilleran terranes, Part B. In Geology of the Cordilleran Orogen in Canada. Edited by Gabrielse H. Yorath C.J. Geological Society of America, The Geology of North America, Vol. G-2, pp. 281–327. Monger, J., & Price, R. (2002). The Canadian Cordillera: geology and tectonic evolution. CSEG Recorder, 27(2), 17–36.

Mortensen, J.K., Ghosh, D., and Ferri, F., (1995), U-Pb age constraints of intrusive rocks associated with copper-gold porphyry deposits in the Canadian Cordillera: Canadian Institute of Mining, Metallugy, and Petroleum, Special Volume 46, p. 142–158.

Nelson, J. L., van Straaten, B., & Friedman, R. (2022). Latest Triassic–Early Jurassic Stikine–Yukon-Tanana terrane collision and the onset of accretion in the Canadian Cordillera: Insights from Hazelton Group detrital zircon provenance and arc–back-arc configuration. Geosphere, 18(2), 670-696.

Nelson, J.L., and Colpron, M., (2007). Tectonics and metallogeny of the Canadian and Alaskan Cordillera, 1.8 Ga to present. In: Goodfellow, W.D., (Ed.), Mineral Deposits of Canada: A Synthesis of Major Deposit Types, District Metallogeny, the Evolution of Geological Provinces, and Exploration Methods. Mineral Deposit Division, Geological Association of Canada, Special Publication 5, pp. 755-791.

Nelson, J. L., Colpron, M., & Israel, S. (2013). The Cordillera of British Columbia, Yukon, and Alaska: Tectonics and metallogeny. En M. Colpron, T. Bissig, B. G. Rusk, & L. G. Thompson (Eds.), Tectonics, metallogeny, and discovery: The North American Cordillera and similar accretionary settings (pp. 53–109). Society of Economic Geologists, Special Publication No. 17.

Pearce, J. A., & Cann, J. R. (1973). Tectonic setting of basic volcanic rocks determined using trace element analyses. Earth and Planetary Science Letters, 19(2), 290–300.

Pearce, J.A., & Norry, M.J. (1979). Petrogenetic implications of Ti, Zr, Y, and Nb variations in volcanic rocks. Chemical Geology, 26, 227–248.

Pearce, J. A., & Peate, D. W. (1995). Tectonic implications of the composition of volcanic arc magmas. Annual Review of Earth and Planetary Sciences, 23(1), 251-285.

Pearce, J.A. (1996). A user's guide to basalt discrimination diagrams. In Wyman, D.A. (Ed.), Trace Element Geochemistry of Volcanic Rocks: Applications for Massive Sulphide Exploration (pp. 79–113). Geological Association of Canada, Short Course Notes, Vol. 12.

Reed, M. H. (1997). Hydrothermal alteration and its relationship to ore fluid composition. Reviews in Economic Geology, 6, 323–365.

Richards, J.P., (2002). Discussion on 'Giant versus small porphyry copper deposits of Cenozoic age in norther Chile: Adakitic versus normal calc-alkaline magmatism' by Oyarzun et al. (Mineralium Deposita, v. 36, p. 794–798, 2001): Mineralium Deposita, v. 37, p. 788–790.

Richards, J. P. (2009). The porphyry copper-gold deposit environment: Ore genesis and exploration. Reviews in Economic Geology, 16, 107-143.

Richards, J.P. (2005). Cratonic basement and porphyry Cu–Au deposits in the Andes. Economic Geology, 100(5), 937–951.

Richards, J. P. (2013). High Sr/Y arc magmas and porphyry $Cu \pm Mo \pm Au$ deposits: Just add water. Economic zeology, 108(4), 613–619.

Richards, J. P., Spell, T., Rameh, E., Razique, A., & Fletcher, T. (2012). High Sr/Y magmas reflect arc maturity, high magmatic water content, and porphyry Cu±Mo±Au potential: Examples from the Tethyan arcs of central and eastern Iran and western Pakistan. Economic Geology, 107(2), 295–332.

Rollinson, H.R., (1993). Using Geochemical Data: Evaluation, Presentation, Interpretation. Pearson Education Limited, Essex.

Rosset, S., & Hart, C. J. R. (2015). Hydrothermal alteration and mineralization at the Kerr and Deep Kerr copper-gold porphyry deposits, northwestern British Columbia (parts of NTS 104B/08). Geoscience BC Summary of Activities, 2016-1.

Seedorff, E., Dilles, J. H., Proffett, J. M., Jr., Einaudi, M. T., Zurcher, L., Stavast, W. J., Barton, M. D., & Johnson, D. A. (2005). Porphyry deposits: Characteristics and origin of hypogene features. In J. W. Hedenquist, J. F. H. Thompson, R. J. Goldfarb, & J. P. Richards (Eds.), Economic Geology 100th Anniversary Volume (pp. 251–298). Society of Economic Geologists.

Sillitoe, R. H. (2010). Porphyry copper systems. Economic Geology, 105(1), 3-41.

Souther, J.G., (1972). Telegraph Creek map area, British Columbia. Geological Survey of Canada Paper 71-44, 38 p.

Stanley, B., & Nelson, J. (2021). Revised stratigraphy of the Stuhini and Hazelton groups and LA-ICP-MS zircon geochronology of the Scottie gold mine area, northwestern British Columbia. Geological Fieldwork, 2022-01.

Sun, S. S., & McDonough, W. F. (1989). Chemical and isotopic systematics of oceanic basalts: Implications for mantle composition and processes. Geological Society, London, Special Publications, 42(1), 313-345.

Tombe, S. P. (2019). Exploration and mining in the Northwest Region, British Columbia. Provincial Overview of Exploration and Mining in British Columbia, 2020-01.

von Quadt, A., Erni, M., Martinek, K., Moll, M., Peytcheva, I., and Heinrich, C.A., (2011), Zircon crystallization and the lifetimes of ore-forming magmatic-hydrothermal systems: Geology, v. 39, p. 731–734.

Wang, X., Cao, H., Zhang, H., Chen, G., Wu, J., & Duan, H. (2024). Origin and evolution of ore-forming fluid in magmatic—hydrothermal Cu–Pb–Zn deposits: Constraints from fluid inclusions, H–O–S isotopes, and trace elements. Minerals, 14(10), 961. https://doi.org/10.3390/min14100961

Wilkinson, J. J. (2013). Triggers for the formation of porphyry ore deposits in magmatic arcs. Nature Geoscience, 6(11), 917–925.

Wilson, M. (1989). (1989), Igneous Petrogenesis, A Global Tectonic Approach. London, UK, Unwin Hyman, https://doi. org/10, 1007, 978-1.

Winter, J D. (2010). Principles of Igneous and Metamorphic Petrology. Pearson Education.

Wood, D. A., Joron, J. L., & Treuil, M. (1992). A re-appraisal of the use of trace elements to classify and discriminate between magma series erupted in different tectonic settings. Earth and Planetary Science Letters, 105(4), 492–506.

Yuan, H., Gao, S., Liu, X., Li, H., Günther, D., & Wu, F. (2004). Accurate U-Pb age and trace element determinations of zircon by laser ablation-inductively coupled plasma-mass spectrometry. Geostandards and Geoanalytical Research, 28(3), 353-370.

Zhai, Y. S., Yao, S. Z., & Cai, K. Q. (2011). Mineral deposits, 3rd ed.; Geological Publishing Press: Beijing, China; pp. 124–125.

Appendix A. List of samples Saddle North

	DRILL				DRILL		
SAMPLE ID	HOLE ID	FROM (m)	TO (m)	SAMPLE ID	HOLE ID	FROM (m)	TO (m)
SSD23LZ001	TTD-109	18.56	18.67	SSD23LZ052	TTD-134	672	672.06
SSD23LZ002	TTD-109	510.9	511.7	SSD23LZ053	TTD-134	651.84	652
SSD23LZ003	TTD-109	619.33	620.47	SSD23LZ054	TTD-134	682.84	683
SSD23LZ004	TTD-109	942.7	943.5	SSD23LZ055	TTD-134	701	701.28
SSD23LZ005	TTD-109	1013.5	1014.7	SSD23LZ056	TTD-134	708.16	708.45
SSD23LZ006	TTD-109	1015.45	1017.3	SSD23LZ057	TTD-134	816.22	816.42
SSD23LZ007	TTD-109	1035	1035.27	SSD23LZ058	TTD-134	817.32	817.53
SSD23LZ008	TTD-109	1101.8		SSD23LZ059	TTD-134	820.65	820.85
SSD23LZ009	TTD-109	1103.2	1104	SSD23LZ060	TTD-134	826.08	826.9
SSD23LZ010	TTD-109	1133.82	1134.75	SSD23LZ061	TTD-134	839.32	839.6
SSD23LZ011	TTD-109	245.35		SSD23LZ062	TTD-134	842.13	842.26
SSD23LZ012	TTD-109	262.2		SSD23LZ063	TTD-134	846.62	846.82
SSD23LZ013	TTD-109	292.5	292.8	SSD23LZ064	TTD-134	852	852.9
SSD23LZ014	TTD-109	353.7	353.9	SSD23LZ065	TTD-134	858.06	858.22
SSD23LZ015	TTD-109	772.75	773	SSD23LZ066	TTD-134	859.31	859.49
SSD23LZ016	TTD-109	904.8	904.95	SSD23LZ067	TTD-134	868.4	868.69
SSD23LZ017	TTD-109	907	907.2	SSD23LZ068	TTD-134	883.29	883.56
SSD23LZ018	TTD-109	920.85	921	SSD23LZ069	TTD-134	849.8	894.92
SSD23LZ019	TTD-109	922.8	922.9	SSD23LZ070	TTD-134	909.62	909.76
SSD23LZ020	TTD-109	928.05	928.15	SSD23LZ071	TTD-134	911.45	911.62
SSD23LZ021	TTD-109	932.2	932.4	SSD23LZ072	TTD-134	914.28	914.4
SSD23LZ022	TTD-109	973	973.2	SSD23LZ073	TTD-134	930.24	930.4
SSD23LZ023	TTD-109	768.19	786.49	SSD23LZ074	TTD-134	944.39	944.54
SSD23LZ024	TTD-109	1039.09	1039.23	SSD23LZ075	TTD-134	956.54	956.67
SSD23LZ025	TTD-109	1044.62	1044.85	SSD23LZ076	TTD-134	960.39	960.68
SSD23LZ026	TTD-109	1063	1063.15	SSD23LZ077	TTD-134	968.19	968.68
SSD23LZ027	TTD-109	1117.4	1117.55	SSD23LZ078	TTD-134	978.79	978.94
SSD23LZ028	TTD-093	833.63		SSD23LZ079	TTD-134	991.28	992.28
SSD23LZ029	TTD-093	835.6	835.7	SSD23LZ080	TTD-134	1027	1027.3
SSD23LZ030	TTD-093	845.92	86	SSD23LZ081	TTD-128	1308	1308.13
SSD23LZ031	TTD-093	846	846.12	SSD23LZ082	TTD-128	1313.16	1313.28
SSD23LZ032	TTD-093	846.25	846.32	SSD23LZ083	TTD-128	1313.28	1313.95
SSD23LZ033	TTD-093	847.18		SSD23LZ084	TTD-128	1320.49	1320.7
SSD23LZ034	TTD-093	851.42	851.56	SSD23LZ085	TTD-128	1328.08	1328.2
SSD23LZ035	TTD-093	852	852.33	SSD23LZ086	TTD-128	1334.45	1334.64
SSD23LZ036	TTD-093	853	853.06	SSD23LZ087	TTD-128	1350.45	1350.6

SSD23LZ037	TTD-093	856.57	856.78	SSD23LZ088	TTD-128	1350.67	1350.78
SSD23LZ038	TTD-093	859.25	859.51	SSD23LZ089	TTD-128	1355.46	1355.67
SSD23LZ039	TTD-093	864.24	864.47	SSD23LZ090	TTD-128	1369	1369.1
SSD23LZ040	TTD-093	867.33	867.44	SSD23LZ091	TTD-128	1371.23	1371.32
SSD23LZ041	TTD-093	873.15	873.24	SSD23LZ092	TTD-128	1384.27	1384.44
SSD23LZ042	TTD-093	876.8	877	SSD23LZ093	TTD-128	1399.8	1400.55
SSD23LZ043	TTD-093	878.82	879	SSD23LZ094	TTD-128	1428.33	1428.45
SSD23LZ044	TTD-093	883.8	883.9	SSD23LZ095	TTD-128	1428.45	1429.14
SSD23LZ045	TTD-093	885.22	885.33	SSD23LZ096	TTD-128	1440	1440.18
SSD23LZ046	TTD-093	891	891.09	SSD23LZ097	TTD-128	1454	1454.21
SSD23LZ047	TTD-093	844.44	845.39	SSD23LZ098	TTD-128	1460.5	1460.67
SSD23LZ048	TTD-093	864	865.15	SSD23LZ099	TTD-128	1464.86	1465.1
SSD23LZ049	TTD-093	890	890.9	SSD23LZ100	TTD-128	1477.42	1474.86
SSD23LZ050	TTD-134	659	660	SSD23LZ101	TTD-106	450.23	451.1
SSD23LZ051	TTD-134	670.88	671	SSD23LZ102	TTD-106	467.12	467.27

Appendix B. Petrography

Sample ID: SSD23LZ001	Depth: 18.56-18.67 m	Drill Hole ID: TTD-109	Rock Type: Volcanic rock Diorite
Mineral	Abundance	Habit	Comments
Plagioclase	25%	Subhedral	Subhedral phenocrysts (< 5 mm long) partially sericitized
K-Feldspar	20%	Subhedral	Greyish crystals up to 2 cm long and fine-grained groundmass of dark grey plagioclase, quartz, and amphibole that is variably altered to sericite, chlorite and minor calcite.
Quartz	15%	Subhedral	Groundmass of fine-grained.
Mafic Minerals			
Hornblende	8%	Subhedral	Elongate crystals nearly replaced by chlorite
Biotite	5%	Subhedral	Elongate prismatic crystals were randomly orientated and replaced by chlorite.
Alteration Minerals			
Chlorite	5%	Anhedral	Occur as irregular-shaped masses adjacent to the crystals, possibly as an alteration product of the mafic minerals (hornblende) and also form as a replacement for biotite.
Epidote	3%	Anhedral	occur as two parallel linear veins with a quartz-rich vein, and also form a replacement of biotite.
Calcite	4%	Subhedral	Occur as roughly rectangular laths with occasionally rounded edges in veins and disseminated grains in the in the diorite host rock.
Opaque Minerals		1	
Pyrite	2%	Anhedral	small anhedral rounded crystals are sporadically disseminated throughout the host rock.
Chalcopyrite	2%	Anhedral	small anhedral rounded crystals are sporadically disseminated throughout the host rock.

Overall Comments: Volcanic greenish or greenish-brown colours, banding to massive aphanitic rock. Compositionally Subhedral to euhedral plagioclase phenocrysts-rich (<5 mm) and hornblende phenocrysts (<5 mm) intruded (sharp intrusive contact) by felsic granitic rock which is primarily composed of quartz, K-Feldspar, and orthoclase feldspar and groundmass of fine-grained quartz, and K-feldspar. Other minerals, such as biotite and hornblende, are typically current in small amounts with magnetite, chalcopyrite, and pyrite. The groundmass consists of differentiable, fine-grained quartz and plagioclase.

Sample ID: SSD23LZ007	Depth: 1035-1035.27 m	Drill Hole ID: TTD-109	Rock Type: Monzodiorite
Mineral	Abundance	Habit	Comments
Plagioclase	25%	Subhedral	Subhedral phenocrysts 3 to 5 mm in diameter partially sericitized
K-Feldspar	45%	Subhedral	Phenocryst felsic aphanitic composition ranges up to 3-4 cm, and fine-grained groundmass feldspar occurs with the quartz grains. However, the plagioclase appears with a dusty surface due to sericite alteration.
Quartz	3%	Subhedral	Fine grained groundmass.
Mafic Minerals	1		
Hornblende	4%	Subhedral	Elongate crystals nearly replaced by chlorite
Biotite	3%	Subhedral	elongate prismatic crystals were randomly orientated and replaced by chlorite.
Pyroxene	2%	Euhedral - Subhedral	Represented by regular and prismatic shaped crystals
Alteration Miner	als		
Chlorite	4%	Anhedral - Subhedral	Occur as irregularly shaped masses adjacent to the crystals, possibly as an alteration product of the mafic minerals (hornblende and biotite).
Calcite	4%	Subhedral	Rectangular with occasionally rounded edges in veins with quartz and with magnetite and sulphide grains.
Opaque Minerals	j		
Pyrite	2%	Anhedral	Small irregular crystals are sporadically disseminated throughout the host rock.
Chalcopyrite	2%	Anhedral	Small, rounded crystals are sporadically disseminated throughout the host rock.
Magnetite	5%	Anhedral	Occurs as disseminated, aggregates and in veins with pyrite and chalcopyrite

Overall Comments: Granitic rock primarily composed of K-Feldspar, orthoclase feldspar, and minor quartz. Other minerals, such as pyroxene, biotite and hornblende, are typically present in small amounts with magnetite, chalcopyrite, and pyrite. The groundmass consists mostly of fine-grained quartz and plagioclase. Veins calcite and quartz and with magnetite and sulphide grains.

Sample ID: SSD23LZ052	Depth: 672-672.06 m	Drill Hole ID: TTD-134	Rock Type: Monzodiorite		
Mineral	Abundance	Habit	Comments		
Plagioclase	35%	Subhedral	Subhedral phenocrysts 3 to 5 mm in diameter partially sericitized		
K-Feldspar	40%	Subhedral	Occurs as fine-grained groundmass with the quartz grains. The plagioclase appears with a dusty surface due to sericite alteration.		
Quartz	5%	Subhedral	Fine grained groundmass with K-feldspar appears with a dusty surface due to sericite alteration.		
Mafic Minerals	•				
Hornblende	4%	Subhedral	Elongate crystals nearly replaced by chlorite		
Biotite	3%	Subhedral	elongate prismatic crystals were randomly orientated and replaced by chlorite.		
Alteration Minerals					
Chlorite	4%	Anhedral	Occur as irregularly shaped masses adjacent to the crystals, possibly as an alteration product of the mafic minerals (Hornblende, and biotite).		
Epidote	7%	Anhedral	occur as two parallel linear veins of lath to prism-shaped amphibole wide with a quartz-rich vein.		
Calcite	4%	Subhedral	Rectangular with occasionally rounded edges in veins with quartz and sulphide grains and with magnetite and occurs as vein with sulphide.		
Opaque Minerals	1	•			
Pyrite	4%	Subhedral to euhedral	Crystals are sporadically disseminated, aggregate, and in veins, and occur along with calcite and minor magnetite.		
Chalcopyrite	3%	Subhedral to euhedral	Crystals are sporadically disseminated, aggregate, and in veins, and occur along with calcite and minor magnetite.		
Magnetite	2%	Anhedral	occurs disseminated, aggregates, and in veins with pyrite and chalcopyrite		

Overall Comments: Granitic rock, which is primarily composed of quartz, K-feldspar, and orthoclase feldspar. Other minerals, such as biotite and hornblende, are typically present in small amounts with magnetite, chalcopyrite, and pyrite. The groundmass consists mostly of fine-grained quartz and plagioclase. Vein type Qz+Mg+Py+Cpy, A-vein and D-vein.

Sample ID: SSD23LZ055	Depth: 701-701.28 m	Drill Hole ID: TTD-134	Rock Type: Monzodiorite
Mineral	Abundance	Habit	Comments
Plagioclase	45%	Subhedral	Subhedral phenocrysts 3 to 5 mm in diameter are partially sericitized.
K-Feldspar	35%	Subhedral	Phenocrysts and fine-grained groundmass feldspar occur with quartz (minor content). The K-feldspar appears with a dusty surface due to sericite alteration.
Quartz	4%	Subhedral	Fine-grained groundmass inequigranular with rounded grain boundaries. Mostly present in veins.
Mafic Minerals	•	1	
Hornblende	4%	Subhedral	Elongate crystals nearly replaced by chlorite
Biotite	3%	Subhedral	elongate tabular crystals were randomly orientated and replaced by chlorite.
Alteration Mineral	s		
Chlorite	4%	Anhedral	Occur as irregularly shaped masses adjacent to the crystals, possibly as an alteration product of the mafic minerals (Hornblende, and biotite).
Epidote	3%	Anhedral	occur as two parallel linear veins of lath to prism-shaped amphibole wide with a quartz-rich vein.
Opaque Minerals	•		
Pyrite	1%	Subhedral to euhedral	Crystals are sporadically disseminated, aggregate, and in veins throughout the host rock, and occur along with magnetite.
Chalcopyrite	1%	Subhedral to euhedral	Crystals are sporadically disseminated, aggregate, and in veins throughout the host rock, and occur along with magnetite.
Magnetite	2%	Anhedral	occurs disseminated, aggregates, and in veins with pyrite and chalcopyrite

Overall Comments: Granitic rock aphanitic granular texture composed primarily of plagioclase, and K-feldspar, and with minor content of quartz. Other minerals, such as biotite and hornblende, are typically current in small amounts with magnetite, chalcopyrite, and pyrite, some of the darker clots appear to magnetite and sulphides appear preferentially disseminated and in veins. Phenocrysts are randomly oriented, and the grey aphanitic groundmass consists mostly of fine-grained quartz and plagioclase (K-Feldspar).

Sample ID: SSD23LZ056	Depth: 708.16-708.45 m	Drill Hole ID: TTD-134	Rock Type: Monzodiorite		
Mineral	Abundance	Habit	Comments		
Plagioclase	35%	Subhedral	Subhedral phenocrysts 3 to 5 mm in diameter partially sericitized		
K-Feldspar	42%	Subhedral	Phenocrysts and fine-grained groundmass feldspar occur with quartz (minor content). The K-feldspar appears with a dusty surface due to sericite alteration.		
Quartz	5%	Subhedral	Fine-grained groundmass. inequigranular with rounded grain boundaries. Mostly present in veins.		
Mafic Minerals					
Hornblende	4%	Subhedral	Elongate crystals nearly replaced by chlorite		
Biotite	3%	Subhedral	elongate prismatic crystals were randomly orientated and replaced by chlorite.		
Pyroxene	2%	Sudnedral	Represented by regular and prismatic shapes crystals		
Alteration Minerals					
Chlorite	4%	Anhedral	Occur as irregularly shaped crystals, possibly as an alteration product of the mafic minerals (Hornblende, and biotite).		
Epidote	7%	Anhedral	occur as veins and as a product of alteration (prism-shaped amphibole).		
Calcite	4%	Subhedral	Occurs as rectangular with occasionally rounded edges in veins occasionally with quartz and with magnetite and sulphides grains.		
Opaque Minerals	I				
Pyrite	2%	Subhedral to euhedral	Crystals are sporadically disseminated, aggregate, and in veins throughout the host rock, and occur along with magnetite.		
Chalcopyrite	1%	Subhedral to anhedral	Crystals are sporadically disseminated, aggregate, and in veins throughout the host rock, and occur along with magnetite.		
Magnetite	3%	Anhedral	occurs disseminated, aggregates, and in veins with pyrite and chalcopyrite		
Gold	1%	Anhedral	Occurs as disseminated with sulphides (pyrite and Chalcopyrite), occasionally in veins also with magnetite		
	1	1			

Overall Comments: Granitic rock aphanitic granular texture composed primarily of plagioclase, and K-feldspar, and with minor content of quartz. Other minerals, such as biotite and hornblende, are typically current in small amounts with magnetite, chalcopyrite, and pyrite, and minor content gold (disseminated and in veins), some of the darker clots appear to magnetite and sulphides appear preferentially disseminated and in veins. The grey aphanitic groundmass consists mostly of fine-grained quartz and plagioclase (K-Feldspar). Vein type Qz+Mg+Py+Cpy, A-vein and D-vein.

Sample ID: SSD23LZ058	Depth: 817.32-817.53 m	Drill Hole ID: TTD-134	Rock Type: Volcanic Basaltic/Andesitic rock
Mineral	Abundance	Habit	Comments
Plagioclase	45%	Subhedral	Subhedral phenocrysts 5 mm long partially sericitized with a dusty surface.
K-Feldspar	40%	Subhedral	Subhedral phenocrysts 3 to 5 mm long partially sericitized appears with a dusty surface, finegrained groundmass feldspar occurs with quartz (minor content).
Quartz	1%	Subhedral	Fine-grained groundmass. inequigranular with rounded grain boundaries. Mostly present in veins.
Mafic Minerals			
Hornblende	7%	Subhedral	Elongate crystals nearly replaced by chlorite
Biotite	5%	Subhedral	Elongate prismatic crystals randomly orientated and replaced by chlorite.
Alteration Minerals	I	1	-
Chlorite	4%	Anhedral	Occur as irregularly shaped masses adjacent to the crystals, possibly as an alteration product of the mafic minerals (Hornblende, and biotite).
Epidote	7%	Anhedral	Occur as two parallel linear veins of lath to prism- shaped amphibole wide with a quartz-rich vein.
Calcite	4%	Subhedral	Rectangular occasionally rounded edges in veins with quartz and with magnetite and sulphides grains.
Opaque Minerals			
Pyrite	1%	Anhedral	Inequigranular crystals are sporadically disseminated throughout the host rock.
Chalcopyrite	8%	Anhedral	Anhedral inequigranular crystals are sporadically disseminated throughout the host rock.
Magnetite	10%	Anhedral	Occurs disseminated, aggregates, and in veins with pyrite and chalcopyrite

Overall Comments: Phenocrysts are randomly oriented, subhedral to euhedral plagioclase, hornblende and biotite with grey aphanitic groundmass consisting mostly of fine-grained quartz and plagioclase (K-Feldspar). Other minerals, such as biotite and hornblende, are typically elongate prismatic crystals with magnetite, chalcopyrite, and pyrite, and also in veins with calcite, also carbonate veins.

Sample ID: SSD23LZ062	Depth: 842.13-842.26 m	Drill Hole ID: TTD-134	Rock Type: Monzodiorite
Mineral	Abundance	Habit	Comments
Plagioclase	25%	Subhedral	Subhedral phenocrysts 5 mm long partially sericitized with a dusty surface. Randomly oriented.
K-Feldspar	20%	Subhedral	Subhedral phenocrysts 3 to 5 mm long partially sericitized appears with a dusty surface, finegrained groundmass feldspar occurs with quartz (minor content).
Quartz	15%	Subhedral	Fine-grained groundmass inequigranular with rounded grain boundaries. Mostly present in veins.
Mafic Minerals	I		
Hornblende	4%	Subhedral	Elongate crystals nearly replaced by chlorite
Biotite	3%	Subhedral	Elongate prismatic crystals were randomly orientated and replaced by chlorite.
Alteration Minerals	1		
Chlorite	4%	Anhedral	Occur as irregularly adjacent to the crystals, possibly as an alteration product of the mafic minerals (Hornblende, and biotite).
Epidote	7%	Anhedral	Occur as irregularly adjacent to the crystals and also with a quartz-rich vein.
Calcite	4%	Subhedral	Rectangular occasionally rounded edges in veins.
Opaque Minerals			
Pyrite	5%	Subhedral to euhedral	Crystals are sporadically disseminated, aggregate, and in veins, and occur along with magnetite.
Chalcopyrite	2%	Anhedral	Crystals are sporadically disseminated, aggregate, and in veins, and occur along with magnetite.
Magnetite	15%	Anhedral	Occurs disseminated, aggregates, and in veins with pyrite and chalcopyrite

Overall Comments: Granitic rock medium-grained and consists of porphyritic hornblende, biotite, plagioclase, and lesser K-feldspar in a fine-grained groundmass of K-feldspar, plagioclase, and minor quartz with veins type A and D + magnetite, with abundant magnetite (aggregate and veins), chalcopyrite, and pyrite.

Sample ID: SSD23LZ066	Depth: 859.31-859.49 m	Drill Hole ID: TTD-134	Rock Type: Monzodiorite
Mineral	Abundance	Habit	Comments
Plagioclase	45%	Euhedral to subhedral	Phenocrysts are 2 to 5 mm long and occur both elongated euhedral and subhedral tablets. plagioclase appears with a dusty surface due to sericite alteration.
K-Feldspar	32%	Subhedral	Subhedral phenocrysts 3 to 5 mm partially sericitized and fine-grained groundmass feldspar with quartz
Quartz	3%	Anhedral	Fine-grained groundmass inequigranular with rounded grain boundaries. Mostly present in veins.
Mafic Minerals			
Hornblende	15%	Subhedral	Elongate crystals nearly replaced by chlorite
Biotite	8%	Subhedral	elongate prismatic crystals were randomly orientated and replaced by chlorite.
Alteration Minerals			
Chlorite	2%	Anhedral	Occur as an irregular shape adjacent to the crystals, possibly as an alteration product of the mafic minerals (hornblende and biotite).
Calcite	5%	Subhedral	Roughly rectangular in veins and occasionally rounded edges with quartz, magnetite and sulphides.
Opaque Minerals		•	
Pyrite	2%	Subhedral to euhedral	Crystals are disseminated, aggregate, and in veins, and occur along with magnetite.
Chalcopyrite	3%	Subhedral to anhedral	Crystals are disseminated, aggregate, and in veins, and occur along with magnetite.
Magnetite	10%	Anhedral to subhedral	Occurs disseminated, aggregates, and in veins with pyrite and chalcopyrite.

Overall Comments: Granitic rock is medium-grained and consists of porphyritic plagioclase, K-Feldspar, and quartz. Other minerals, such as biotite and hornblende, are typically elongated prismatic crystals with magnetite, chalcopyrite, and Pyrite. The groundmass consists mostly of fine-grained quartz, K-feldspar and plagioclase. Vein type Qz+Mg+Py+Cpy, A-vein and D-vein.

Sample ID: SSD23LZ068	Depth: 883.29-883.56 m	Drill Hole ID: TTD-134	Rock Type: Breccia
Mineral	Abundance	Habit	Comments
Plagioclase	45%	Subhedral	Phenocrysts are 2 to 5 mm long and occur in both elongated euhedral and subhedral tablets. plagioclase appears with a dusty surface due to sericite alteration.
K-Feldspar	30%	Subhedral	Subhedral phenocrysts 3 to 5 mm partially sericitized and also occurs as fine-grained groundmass feldspar with quartz
Quartz	3%	Subhedral	Fine-grained groundmass inequigranular with rounded grain boundaries. Mostly present in veins.
Mafic Minerals	1		
Hornblende	4%	Subhedral	Elongate crystals nearly replaced by chlorite
Biotite	3%	Subhedral	elongate prismatic crystals were randomly orientated and replaced by chlorite.
Alteration Minerals			
Chlorite	5%	Anhedral	Occur as irregularly shaped masses adjacent to the crystals, possibly as an alteration product of the mafic minerals (Hornblende, and biotite).
Epidote	1%	Anhedral	Occur as irregularly shaped masses adjacent to the crystals.
Calcite	3%	Subhedral to anhedral	Rectangular crystals in veins and occasionally rounded edges in veins with quartz and with magnetite and sulphide grains.
Opaque Minerals			
Pyrite	1%	Anhedral	Small rounded disseminated are disseminated, aggregate, and in veins, and crystals occur along with magnetite.
Chalcopyrite	3%	Anhedral	Small rounded crystals are disseminated, aggregate, and in veins, and crystals occur along with magnetite.
Magnetite	5%	Anhedral to subhedral	Occurs disseminated, aggregates, and in veins with pyrite and chalcopyrite.

Overall Comments: Polymictic matrix breccia sub-angular to subrounded, poorly to moderately well sorted. The clasts are derived from phenocrystic orthoclase plagioclase-phyric monzonite and orthoclase-phyric monzodiorite. Porphyritic clast is medium-grained and consists of plagioclase, K-Feldspar, and quartz. Other minerals, such as biotite and hornblende, are typically elongated prismatic crystals with magnetite, chalcopyrite, and Pyrite. The groundmass consists mostly of fine-grained quartz, K-feldspar and plagioclase. Veins type A and D, and carbonate vein.

Sample ID: SSD23LZ071	Depth: 911.45-911.62 m	Drill Hole ID: TTD-134	Rock Type: Monzodiorite
Mineral	Abundance	Habit	Comments
Plagioclase	35%	Subhedral	Phenocrysts are 3 to 5 mm long and occur in both elongated euhedral and subhedral tablets. plagioclase appears with a dusty surface due to sericite alteration.
K-Feldspar	30%	Subhedral	Subhedral phenocrysts 2 to 4 mm partially sericitized with a dusty surface and also occur as fine-grained groundmass feldspar with quartz
Quartz	15%	Subhedral	Fine-grained groundmass inequigranular with rounded grain boundaries. Mostly present in veins.
Mafic Minerals			•
Hornblende	4%	Subhedral	Elongate crystals nearly replaced by chlorite
Biotite	3%	Subhedral	elongate prismatic crystals were randomly orientated and replaced by chlorite.
Alteration Minerals	1	1	
Chlorite	4%	Anhedral	Occur as irregularly shaped masses adjacent to the crystals, possibly as an alteration product of the mafic minerals (Hornblende, and biotite).
Epidote	1%	Anhedral	occur as two parallel linear veins of lath to prism-shaped with a quartz-rich vein.
Calcite	6%	Subhedral	Occurs rectangular with occasionally rounded edges in veins with quartz and with magnetite and sulphide grains.
Opaque Minerals		_	
Pyrite	1%	Anhedral	small anhedral rounded crystals are sporadically disseminated throughout the host rock.
Chalcopyrite	2%	Anhedral	small anhedral rounded crystals are sporadically disseminated throughout the host rock.
Magnetite	7%	Anhedral to subhedral	Occurs disseminated, aggregates, and in veins with pyrite and chalcopyrite.
	•	•	•

Overall Comments: Monzodiorite is medium-grained and consists of plagioclase, K-Feldspar, and quartz. Other minerals, such as biotite and hornblende, are typically elongated prismatic crystals with magnetite, chalcopyrite, and pyrite. The groundmass consists mostly of fine-grained quartz, K-feldspar and plagioclase. Veins type A and D.

Sample ID: SSD23LZ072	Depth: 914.28-914.4 m	Drill Hole ID: TTD-134	Rock Type: Monzodiorite
Mineral	Abundance	Habit	Comments
Plagioclase	40%	Subhedral	Phenocrysts are 3 to 5 mm long and occur in elongated euhedral and subhedral tablets. plagioclase appears with a dusty surface due to sericite alteration.
K-Feldspar	35%	Subhedral	Subhedral phenocrysts 2 to 4 mm partially sericitized with a dusty surface, and also occur as fine-grained groundmass feldspar with quartz
Quartz	1%	Subhedral	Fine-grained groundmass inequigranular with rounded grain boundaries. Mostly present in veins.
Mafic Minerals		l	
Hornblende	4%	Subhedral	Elongate crystals nearly replaced by chlorite
Biotite	3%	Subhedral	Elongate prismatic crystals were randomly orientated and replaced by chlorite.
Alteration Minerals			
Chlorite	4%	Anhedral	Occur as irregularly shaped masses adjacent to the crystals, possibly as an alteration product of the mafic minerals (hornblende, and biotite).
Epidote	1%	Anhedral	Occur as two parallel linear veins wide with quartzrich vein.
Calcite	6%	Subhedral	Occurs rectangular with occasionally rounded edges in veins with quartz and with magnetite and sulphide grains.
Opaque Minerals			
Pyrite	1%	Subhedral to euhedral	Crystals are sporadically disseminated, aggregate, and occur in veins throughout the host rock along with magnetite.
Chalcopyrite	2%	Subhedral to euhedral l	Crystals are sporadically disseminated, aggregate, and in veins throughout the host rock, and occur along with magnetite.
Magnetite	4%	Anhedral	Occurs disseminated, aggregates, and in veins with pyrite and chalcopyrite

Overall Comments: Granitic rock monzodiorite is medium-grained and consists of plagioclase, K-Feldspar, and quartz. Other minerals, such as biotite and hornblende, are typically elongated prismatic crystals with magnetite, chalcopyrite, and pyrite. The groundmass consists mostly of fine-grained quartz, K-feldspar and plagioclase. Phenocrysts are randomly oriented and the abundance typically varies between 35 and 50 %, and within the grey aphanitic groundmass consists mostly of fine-grained quartz and plagioclase which were hard to distinguish. Veins type A and D.

Sample ID: SSD23LZ073	Depth: 930.24-930.4 m	Drill Hole ID: TTD-134	Rock Type: Monzodiorite	
Mineral	Abundance	Habit	Comments	
Plagioclase	35%	Subhedral	Phenocrysts are 3 to 5 mm long and occur in both elongated euhedral and subhedral tablets. plagioclase appears with a dusty surface due to sericite alteration.	
K-Feldspar	25%	Subhedral	Subhedral phenocrysts 2 to 4 mm partially sericitized with a dusty surface, and also occur as fine-grained groundmass feldspar with quartz	
Quartz	2%	Subhedral	Fine-grained groundmass inequigranular with rounded grain boundaries. Mostly present in veins.	
Mafic Minerals	l	l		
Hornblende	4%	Subhedral	Elongate crystals nearly replaced by chlorite	
Biotite	3%	Subhedral	Elongate prismatic crystals were randomly orientated and replaced by chlorite.	
Alteration Minerals		l		
Chlorite	4%	Anhedral	Occur as irregularly shaped masses adjacent to the crystals, possibly as an alteration product of the mafic minerals (Hornblende, and biotite).	
Epidote	1%	Anhedral	Occur as two parallel linear veins wide with quartzrich vein.	
Calcite	6%	Subhedral	Occurs rectangular with occasionally rounded edges in veins with quartz and with magnetite and sulphide grains.	
Opaque Minerals				
Pyrite	1%	Subhedral to euhedral	Crystals are sporadically disseminated, aggregate, and in veins throughout the host rock, and occur along with magnetite.	
Chalcopyrite	2%	Subhedral to euhedral l	Crystals are sporadically disseminated, aggregate, and occur in veins throughout the host rock along with magnetite.	
Magnetite	4%	Anhedral	Occurs disseminated, aggregates, and in veins with pyrite and chalcopyrite	

Overall Comments: Granitic rock monzodiorite is medium-grained and consists of plagioclase, K-feldspar, and quartz. Other minerals, such as biotite and hornblende, are typically elongated prismatic crystals with magnetite, chalcopyrite, and pyrite. The groundmass consists mostly of fine-grained quartz, K-feldspar and plagioclase. Phenocrysts are randomly oriented, and the abundance typically varies between 35 and 50 %, and within the grey aphanitic groundmass consists mostly of fine-grained quartz and plagioclase which were hard to distinguish. Veins type A + M and D.

Sample ID: SSD23LZ075	Depth: 956.54-956.67 m	Drill Hole ID: TTD-134	Rock Type: Monzodiorite
Mineral	Abundance	Habit	Comments
Plagioclase	25%	Subhedral	Phenocrysts are 3 to 5 mm long and occur in both elongated euhedral and subhedral tablets. plagioclase appears with a dusty surface due to sericite alteration.
K-Feldspar	35%	Subhedral	Subhedral phenocrysts 2 to 4 mm partially sericitized with a dusty surface and also occur as fine-grained groundmass feldspar with quartz
Quartz	5%	Subhedral	Fine-grained groundmass inequigranular with rounded grain boundaries. Mostly present in veins.
Mafic Minerals	1		
Hornblende	4%	Subhedral	Elongate crystals nearly replaced by chlorite
Biotite	3%	Subhedral	Elongate prismatic crystals were randomly orientated and replaced by chlorite.
Alteration Mineral	S	•	
Chlorite	4%	Anhedral	Occur as irregularly shaped masses adjacent to the crystals, possibly as an alteration product of the mafic minerals (Hornblende, and biotite).
Epidote	1%	Anhedral	Occur as two parallel linear veins wide with quartzrich vein.
Calcite	3%	Subhedral	Occurs as rectangular with occasionally rounded edges in veins occasionally infilling quartz veins, and with magnetite and sulphide.
Opaque Minerals			
Pyrite	1%	Subhedral to euhedral	Crystals are sporadically disseminated, aggregate, and in veins throughout the host rock, and occur along with magnetite.
Chalcopyrite	3%	Subhedral to euhedral I	Crystals are sporadically disseminated, aggregate, and occur in veins throughout the host rock along with magnetite.
Magnetite	10%	Anhedral	Occurs as disseminated, aggregates, and in veins with pyrite and chalcopyrite

Overall Comments: Granitic rock monzodiorite is medium-grained and consists of plagioclase, K-feldspar, and quartz. Other minerals, such as biotite and hornblende, are typically elongated prismatic crystals with magnetite, chalcopyrite, and pyrite. The groundmass consists mostly of fine-grained quartz, K-feldspar and plagioclase. Phenocrysts are randomly oriented, and the abundance typically varies between 35 and 50 %, and within the grey aphanitic groundmass consists mostly of fine-grained quartz and plagioclase which were hard to distinguish. Veins type Qz+Mg+Py+Cpy, Ca+Py, and D.

Sample ID: SSD23LZ086	Depth: 1334.45-1334.64 m	Drill Hole ID: TTD-128	Rock Type: Monzodiorite
Mineral	Abundance	Habit	Comments
Plagioclase	15%	Subhedral	Phenocrysts are 1 to 3 mm long and occur in both elongated euhedral and subhedral tablets. plagioclase appears with a dusty surface due to sericite alteration.
K-Feldspar	10%	Subhedral	Subhedral phenocrysts 1 to 2 mm partially sericitized with a dusty surface and also occur as fine-grained groundmass feldspar with quartz
Quartz	5%	Subhedral	Fine-grained groundmass inequigranular with rounded grain boundaries. Mostly present in veins.
Mafic Minerals			
Hornblende	20%	Subhedral	Elongate crystals nearly replaced by chlorite
Biotite	10%	Subhedral	Elongate prismatic crystals were randomly orientated and replaced by chlorite.
Alteration Minerals			
Chlorite	4%	Anhedral	Occur as irregularly shaped masses adjacent to the crystals (hornblende and biotite), possibly as an alteration product of the mafic minerals.
Epidote	1%	Anhedral	Occur as two parallel linear veins wide with quartz-rich vein.
Calcite	15%	Subhedral	Occurs rectangular with occasionally rounded edges in veins occasionally infilling quartz veins, and with magnetite and sulphide.
Opaque Minerals		T	
Pyrite	5%	Subhedral to euhedral	Crystals are sporadically disseminated, aggregate, and in veins throughout the host rock, and occur along with magnetite.
Chalcopyrite	1%	Subhedral to euhedral l	Crystals are sporadically disseminated, aggregate, and occur in veins throughout the host rock along with magnetite.
Magnetite	3%	Anhedral	Occurs as randomly, aggregates, and in veins with pyrite and chalcopyrite

Overall Comments: Andesite to dacite appearance and is medium to very dark grey, massive, and strongly magnetic and it is a visually distinctive unit with euhedral laths of greyish white by the alignment of plagioclase up to 2 cm long enclosed in a massive, fine-grained groundmass of dark grey plagioclase, quartz, and amphibole that is variably altered to sericite, chlorite and calcite. Vein type Ca+Py.

Sample ID: SSD23LZ090	Depth: 1369-1369.10 m	Drill Hole ID: TTD-128	Rock Type: Monzodiorite	
Mineral	Abundance	Habit	Comments	
Plagioclase	25%	Subhedral	Phenocrysts are 1 to 3 mm long and occur in both elongated euhedral and subhedral tablets. plagioclase appears with a dusty surface due to sericite alteration.	
K-Feldspar	10%	Subhedral	Subhedral phenocrysts 1 to 2 mm partially sericitized with a dusty surface and also occur as fine-grained groundmass feldspar with quartz	
Quartz	2%	Subhedral	Fine-grained groundmass inequigranular with rounded grain boundaries. Mostly present in veins.	
Mafic Minerals	1			
Hornblende	10%	Subhedral	Elongate crystals nearly replaced by chlorite	
Biotite	5%	Subhedral	Elongate prismatic crystals were randomly orientated and replaced by chlorite.	
Alteration Minerals		•		
Chlorite	3%	Anhedral	Occur as irregularly shaped masses adjacent to the crystals, possibly as an alteration product of the mafic minerals (Hornblende, and biotite).	
Epidote	2%	Anhedral	Occur as two parallel linear veins wide with quartzrich vein.	
Calcite	10%	Subhedral	Occurs rectangular with occasionally rounded edges in veins occasionally infilling quartz veins, and with magnetite and sulphide.	
Opaque Minerals				
Pyrite	6%	Subhedral to euhedral	Crystals are sporadically disseminated, aggregate, and in veins throughout the host rock, and occur along with magnetite.	
Chalcopyrite	10%	Subhedral to euhedral l	Crystals are sporadically disseminated, aggregate, and occur in veins throughout the host rock along with magnetite.	
Magnetite	8%	Anhedral	Occurs disseminated, aggregates, and in veins with pyrite and chalcopyrite	

Overall Comments: Andesite to dacite appearance and is medium to very dark grey, massive, and strongly magnetic and it is a visually distinctive unit with euhedral laths of greyish white by the alignment of plagioclase up to 2 cm long enclosed in a massive, fine-grained groundmass of dark grey plagioclase, quartz, and amphibole that is variably altered to sericite, chlorite and calcite. Veins type: Ca+Py, Ca infill, and Qz+Py+Cpy(D-Vein).

Sample ID: SSD23LZ091	Depth: 1371.23-1371.32 m	Drill Hole ID: TTD-128	Rock Type: Monzodiorite
Mineral	Abundance	Habit	Comments
Plagioclase	25%	Subhedral	Phenocrysts are 1 to 3 mm long and occur in both elongated euhedral and subhedral tablets. plagioclase appears with a dusty surface due to sericite alteration.
K-Feldspar	10%	Subhedral	Subhedral phenocrysts 1 to 2 mm partially sericitized with a dusty surface and also occur as fine-grained groundmass feldspar with quartz
Quartz	3%	Subhedral	Fine-grained groundmass inequigranular with rounded grain boundaries. Mostly present in veins.
Mafic Minerals		•	
Hornblende	10%	Subhedral	Elongate crystals nearly replaced by chlorite
Biotite	5%	Subhedral	Elongate prismatic crystals were randomly orientated and replaced by chlorite.
Alteration Minera	als		
Chlorite	3%	Anhedral	Occur as irregularly shaped masses adjacent to the crystals, possibly as an alteration product of the mafic minerals (Hornblende, and biotite).
Epidote	2%	Anhedral	Occur as two parallel linear veins wide with quartz-rich vein.
Calcite	5%	Subhedral	Occurs rectangular with occasionally rounded edges in veins occasionally infilling quartz veins, and with magnetite and sulphide.
Opaque Minerals		-	
Pyrite	8%	Subhedral to euhedral	Crystals are sporadically disseminated, aggregate, and in veins throughout the host rock, and occur along with magnetite.
Chalcopyrite	6%	Subhedral to euhedral I	Crystals are sporadically disseminated, aggregate, and occur in veins throughout the host rock along with magnetite.
Magnetite	8%	Anhedral	Occurs disseminated, aggregates, and in veins with pyrite and chalcopyrite

Overall Comments: Andesite to dacite appearance and is medium to very dark grey, massive, and strongly magnetic and it is a visually distinctive unit with euhedral laths of greyish white by the alignment of plagioclase up to 2 cm long enclosed in a massive, fine-grained groundmass of dark grey plagioclase, quartz, and amphibole that is variably altered to sericite, chlorite and calcite. Veins type: Ca+Py, Ca infill, and Qz+MgPy+Cpy.

Sample ID: SSD23LZ098	Depth: 1428.45-1429.14 m	Drill Hole ID: TTD-128	Rock Type: Monzodiorite
Mineral	Abundance	Habit	Comments
Plagioclase	35%	Subhedral	Phenocrysts are 3 to 5 mm long and occur in both elongated euhedral and subhedral tablets. plagioclase appears with a dusty surface due to sericite alteration.
K-Feldspar	25%	Subhedral	Subhedral phenocrysts 2 to 4 mm partially sericitized with a dusty surface and also occur as fine-grained groundmass feldspar with quartz
Quartz	2%	Subhedral	Fine-grained groundmass inequigranular with rounded grain boundaries. Mostly present in veins.
Mafic Minerals	I		
Hornblende	4%	Subhedral	Elongate crystals nearly replaced by chlorite
Biotite	3%	Subhedral	Elongate prismatic crystals were randomly orientated and replaced by chlorite.
Alteration Mineral	S		
Chlorite	4%	Anhedral	Occur as irregularly shaped masses adjacent to the crystals, possibly as an alteration product of the mafic minerals (Hornblende, and biotite).
Epidote	1%	Anhedral	Occur as two parallel linear veins wide with quartzrich vein.
Calcite	3%	Subhedral	Occurs rectangular with occasionally rounded edges in veins occasionally infilling quartz veins, and with magnetite and sulphide.
Opaque Minerals			
Pyrite	1%	Subhedral to euhedral	Crystals are sporadically disseminated, aggregate, and in veins throughout the host rock, and occur along with magnetite.
Chalcopyrite	3%	Subhedral to euhedral l	Crystals are sporadically disseminated, aggregate, and occur in veins throughout the host rock along with magnetite.
Magnetite	5%	Anhedral	Occurs disseminated, aggregates, and in veins with pyrite and chalcopyrite

Overall Comments: Granitic rock monzodiorite is medium-grained and consists of plagioclase, K-feldspar, and quartz. Other minerals, such as biotite and hornblende, are typically elongated prismatic crystals with magnetite, chalcopyrite, and pyrite. The groundmass consists mostly of fine-grained quartz, K-feldspar and plagioclase. Phenocrysts are randomly oriented, and the abundance typically varies between 35 and 50 %, and within the grey aphanitic groundmass consists mostly of fine-grained quartz and plagioclase which were hard to distinguish. Veins type Qz+Mg+Py+Cpy, Ca+Py, and D.

Sample ID:	Depth:	Drill Hole ID:	Rock Type: Monzodiorite
SSD23LZ099 Mineral	1428.45-1429.14 m Abundance	TTD-128 Habit	Comments
Plagioclase	40%	Subhedral	Phenocrysts are 3 to 5 mm long and occur in both elongated euhedral and subhedral tablets. plagioclase appears with a dusty surface due to sericite alteration.
K-Feldspar	25%	Subhedral	Subhedral phenocrysts 2 to 4 mm partially sericitized with a dusty surface and also occur as fine-grained groundmass feldspar with quartz
Quartz	2%	Subhedral	Fine-grained groundmass inequigranular with rounded grain boundaries. Mostly present in veins.
Mafic Minerals		l	
Hornblende	5%	Subhedral	Elongate crystals nearly replaced by chlorite
Biotite	3%	Subhedral	Elongate prismatic crystals were randomly orientated and replaced by chlorite.
Alteration Mineral	5	l	
Chlorite	4%	Anhedral	Occur as irregularly shaped masses adjacent to the crystals, possibly as an alteration product of the mafic minerals (Hornblende, and biotite).
Epidote	1%	Anhedral	Occur as two parallel linear veins wide with quartzrich vein.
Calcite	5%	Subhedral	Occurs in veins, rectangular with occasionally rounded edges in veins with quartz and with magnetite and sulphide grains.
Opaque Minerals			
Pyrite	1%	Subhedral to euhedral	Crystals are sporadically disseminated, aggregate, and in veins throughout the host rock, and occur along with magnetite.
Chalcopyrite	2%	Subhedral to euhedral	Crystals are sporadically disseminated, aggregate, and occur in veins throughout the host rock along with magnetite.
Magnetite	5%	Anhedral	Occurs disseminated, aggregates, and in veins with pyrite and chalcopyrite

Overall Comments: Granitic rock monzodiorite is medium-grained and consists of plagioclase, K-feldspar, and quartz. Other minerals, such as biotite and hornblende, are typically elongated prismatic crystals with magnetite, chalcopyrite, and pyrite. The groundmass consists mostly of fine-grained quartz, K-feldspar and plagioclase. Phenocrysts are randomly oriented, and the abundance typically varies between 35 and 50 %, and within the grey aphanitic groundmass consists mostly of fine-grained quartz and plagioclase which were hard to distinguish. Veins type Qz+Mg+Py+Cpy, Ca+Py, and D.

Sample ID: SSD23LZ100	Depth: 1472.42-1474.69 m	Drill Hole ID: TTD-128	Rock Type: Monzodiorite
Mineral	Abundance	Habit	Comments
Plagioclase	35%	Subhedral	Phenocrysts are 3 to 5 mm long and occur in both elongated euhedral and subhedral tablets. plagioclase appears with a dusty surface due to sericite alteration.
K-Feldspar	25%	Subhedral	Subhedral phenocrysts 2 to 4 mm partially sericitized with a dusty surface and also occur as fine-grained groundmass feldspar with quartz
Nepheline	5%	Subhedral to anhedral	felpspathoid phenocrysts 3 to 5 mm in diameter to fine grained, displaying sharp irregular contacts. Altered sodalite
Quartz	2%	Subhedral	Fine-grained groundmass inequigranular with rounded grain boundaries. Mostly present in veins.
Mafic Minerals			
Hornblende	5%	Subhedral	Elongate crystals nearly replaced by chlorite
Biotite	3%	Subhedral	Elongate prismatic crystals were randomly orientated and replaced by chlorite.
Alteration Minerals	5		
Chlorite	2%	Anhedral	Occur as irregularly shaped masses adjacent to the crystals, possibly as an alteration product of the mafic minerals (Hornblende, and biotite).
Epidote	1%	Anhedral	Occur as two parallel linear veins wide with quartzrich vein.
Calcite	5%	Subhedral	Occurs in veins, rectangular with occasionally rounded edges in veins with quartz and with magnetite and sulphide grains.
Opaque Minerals		T	
Pyrite	4%	Subhedral to euhedral	Crystals are sporadically disseminated, aggregate, and in veins throughout the host rock, and occur along with magnetite.
Chalcopyrite	2%	Subhedral to euhedral	Crystals are sporadically disseminated, and occur as aggregate and in veins throughout the host rock along with magnetite.
Magnetite	7%	Anhedral	Occurs disseminated, aggregates, and in veins with pyrite and chalcopyrite

Overall Comments: Granitic rock monzodiorite is medium-grained and consists of plagioclase, K-feldspar, and quartz. Other minerals, such as biotite and hornblende, are typically elongated prismatic crystals with magnetite, chalcopyrite, and pyrite. The groundmass consists mostly of fine-grained quartz, K-feldspar and plagioclase. Phenocrysts are randomly oriented, and the abundance typically varies between 35 and 50 %, and within the grey aphanitic groundmass consists mostly of fine-grained quartz and plagioclase which were hard to distinguish. Veins type Qz+Mg+Py+Cpy, B vein, and D vein.

Appendix C. Geochemistry major (wt.%.) and trace (ppm) element data.

SAMPLES	SSD23LZ005	SSD23LZ006	SSD23LZ007	SSD23LZ047	SSD23LZ049	SSD23LZ050	SSD23LZ051
Rock Type	Porphyry Intrusion						
Lithology Code	FQMP I2	FQMP I2	FQMP I2	FQMP I3	FQMP I4	FQMP I2	FQMP I2
Al₂O₃%	15.86	17.16	15.94	17.08	17.37	16.88	19.69
BaO%	0.17	0.17	0.17	0.15	0.14	0.06	0.04
CaO%	3.74	4.74	4.06	2.37	3.20	3.86	2.80
Cr ₂ O ₃ %	0.01	0.01	<0.01	0.01	<0.01	<0.01	0.01
Fe₂O₃%	9.22	7.09	8.50	8.21	7.44	6.75	8.93
K₂O%	4.16	3.24	4.66	3.40	2.81	3.87	5.77
MgO%	2.23	2.43	2.07	2.47	2.81	1.16	1.10
MnO%	0.14	0.15	0.12	0.09	0.11	0.09	0.07
Na₂O%	3.23	4.81	3.40	3.84	3.79	2.73	0.51
P ₂ O ₅ %	0.30	0.32	0.30	0.32	0.34	0.28	0.36
SiO ₂ %	56.99	57.03	54.79	57.53	57.03	58.12	53.16
SrO%	0.06	0.08	0.06	0.05	0.03	0.01	0.01
TiO₂%	0.40	0.44	0.39	0.45	0.47	0.42	0.65
LOI	2.84	2.05	3.69	3.48	4.34	4.49	5.91
Total%	101.20	100.20	99.24	103.20	100.75	101.20	107.10

SAMPLES	SSD23LZ055	SSD23LZ056	SSD23LZ057	SSD23LZ058	SSD23LZ059	SSD23LZ060	SSD23LZ061
Rock Type	Porphyry Intrusion	Porphyry Intrusion	Andesitic - dacite	Andesitic - dacite	Porphyry Intrusion	Porphyry Intrusion	Porphyry Intrusion
Lithology Code	FQMP I2	FQMP I2	Volcanic- Volcaniclastic rock	Volcanic- Volcaniclastic rock	FQMP I1	FQMP I1	FQMP I1
Al₂O₃%	18.15	16.99	15.75	13.37	14.08	13.84	14.72
BaO%	0.05	0.17	0.17	0.15	0.17	0.26	0.16
CaO%	3.72	4.67	2.65	3.42	2.62	2.81	2.57
Cr₂O₃%	<0.01	<0.01	<0.01	<0.01	0.01	0.01	0.01
Fe₂O₃%	5.16	6.06	8.84	12.62	11.48	8.81	9.58
K₂O%	5.23	4.63	7.89	6.32	7.29	8.11	6.95
MgO%	1.12	1.46	2.43	2.55	0.85	1.22	1.64
MnO%	0.08	0.12	0.23	0.23	0.12	0.17	0.22
Na₂O%	0.68	1.26	0.95	0.91	1.56	0.57	1.48
P ₂ O ₅ %	0.32	0.28	0.28	0.21	0.22	0.24	0.24
SiO ₂ %	59.91	56.76	54.34	54.27	56.22	57.77	55.89
SrO%	0.01	0.02	0.03	0.04	0.04	0.04	0.03
TiO₂%	0.45	0.42	0.34	0.30	0.32	0.32	0.36
LOI	5.00	6.41	3.93	4.23	3.26	4.74	4.06
Total%	101.60	99.88	103.25	102.95	102.80	108.95	103.60

SAMPLES	SSD23LZ063	SSD23LZ064	SSD23LZ066	SSD23LZ069	SSD23LZ074	SSD23LZ076	SSD23LZ077
Rock Type	Porphyry Intrusion						
Lithology Code	FQMP I1						
Al ₂ O ₃ %	13.24	14.08	13.56	13.46	13.16	13.98	15.49
BaO%	0.15	0.17	0.14	0.17	0.18	0.21	0.14
CaO%	2.65	2.82	3.18	2.45	2.89	2.64	4.01
Cr₂O₃%	0.01	0.01	0.01	0.01	0.01	0.01	0.01
Fe ₂ O ₃ %	9.58	10.27	11.93	17.02	11.45	13.04	9.61
K₂O%	6.47	5.90	5.37	7.23	6.17	7.01	4.14
MgO%	1.64	1.77	1.64	1.48	1.60	1.72	2.35
MnO%	0.18	0.23	0.18	0.17	0.14	0.15	0.13
Na₂O%	1.38	1.68	1.68	1.30	1.75	1.41	2.76
P ₂ O ₅ %	0.18	0.24	0.26	0.25	0.24	0.26	0.31
SiO ₂ %	60.19	55.90	57.08	52.79	57.77	54.87	55.75
SrO%	0.03	0.04	0.04	0.03	0.04	0.04	0.06
TiO₂%	0.29	0.35	0.29	0.30	0.31	0.33	0.39
LOI	3.45	4.35	3.80	2.50	3.43	2.49	2.69
Total%	103.30	102.30	101.00	100.65	101.70	100.40	99.10

SAMPLES	SSD23LZ079	SSD23LZ080	SSD23LZ082	SSD23LZ085	SSD23LZ089	SSD23LZ092	SSD23LZ094
Rock Type	Porphyry Intrusion	Porphyry Intrusion	Andesitic - dacite	Andesitic - dacite	Andesitic - dacite	Porphyry Intrusion	Porphyry Intrusion
Lithology Code	FQMP I2	FQMP I3	Volcanic- Volcaniclastic rock	Volcanic- Volcaniclastic rock	Volcanic- Volcaniclastic rock	FQMP I2	FQMP I2
Al ₂ O ₃ %	15.62	16.10	15.02	16.44	16.49	16.32	15.43
BaO%	0.15	0.11	0.07	0.12	0.06	0.08	0.08
CaO%	4.19	5.28	6.37	4.91	4.42	3.47	5.74
Cr ₂ O ₃ %	0.01	0.01	0.01	0.01	0.01	0.01	0.01
Fe₂O₃%	10.34	8.07	9.59	5.80	7.06	11.48	7.63
K ₂ O%	4.26	3.56	3.29	2.72	3.08	4.02	3.00
MgO%	2.07	2.28	1.92	2.61	2.72	2.00	2.16
MnO%	0.13	0.13	0.12	0.06	0.10	0.13	0.11
Na₂O%	2.93	3.60	2.14	3.90	2.89	2.26	3.19
P ₂ O ₅ %	0.29	0.31	0.29	0.31	0.31	0.29	0.36
SiO₂%	55.74	54.21	50.13	55.46	55.28	53.92	53.32
SrO%	0.07	0.06	0.03	0.06	0.03	0.03	0.04
TiO₂%	0.39	0.41	0.39	0.43	0.43	0.43	0.41
LOI	3.20	5.64	8.84	6.49	5.04	4.16	6.33
Total%	101.05	102.10	>110	104.15	101.50	100.30	104.00

SAMPLES	SSD23LZ095	SSD23LZ096	SSD23LZ101	SSD23LZ102	SSD23LZ103
Rock Type	Porphyry Intrusion	Porphyry Intrusion	Porphyry Intrusion	Porphyry Intrusion	Andesitic - dacite
Lithology Code	FQMP I2	FQMP I2	FQMP I4	FQMP I4	Volcanic- Volcaniclastic rock
Al ₂ O ₃ %	16.32	16.98	16.96	16.92	17.41
BaO%	0.07	0.14	0.04	0.03	0.22
CaO%	6.43	4.96	3.33	4.84	2.64
Cr₂O₃%	0.01	0.01	0.01	0.01	0.01
Fe₂O₃%	7.32	7.18	7.69	7.43	6.31
K₂O%	2.83	3.56	3.47	3.37	3.26
MgO%	2.75	2.17	2.50	1.50	2.16
MnO%	0.12	0.09	0.16	0.13	0.11
Na₂O%	3.23	3.30	2.26	2.71	3.06
P ₂ O ₅ %	0.32	0.32	0.34	0.35	0.29
SiO₂%	52.88	56.26	56.42	56.33	59.01
SrO%	0.05	0.09	0.01	0.01	0.02
TiO₂%	0.45	0.44	0.46	0.45	0.44
LOI	7.09	3.96	5.56	5.38	4.88
Total%	104.70	101.95	106.20	100.15	102.25

SAMPLES	SSD23LZ005	SSD23LZ006	SSD23LZ007	SSD23LZ047	SSD23LZ049	SSD23LZ050	SSD23LZ051	SSD23LZ055	SSD23LZ056	SSD23LZ057	SSD23LZ058
Rock Type	Porphyry Intrusion	Andesitic - dacite	Andesitic - dacite								
Lithology Code	FQMP I2	FQMP I2	FQMP I2	FQMP I3	FQMP I4	FQMP I2	FQMP I2	FQMP I2	FQMP I2	Volcanic- Volcaniclast ic rock	Volcanic- Volcaniclast ic rock
Ba ppm	1505.00	1465.00	1495.00	1295.00	1125.00	392.00	199.50	326.00	1555.00	1505.00	1345.00
Ce ppm	22.90	31.10	18.80	29.60	28.80	29.30	20.70	32.60	30.90	15.60	11.50
Cr ppm	9.00	5.00	6.00	5.00	<5	6.00	9.00	<5	5.00	9.00	10.00
Cs ppm	1.32	1.04	0.79	1.10	2.15	2.06	4.25	4.41	4.01	1.28	0.76
Dy ppm	2.91	3.17	2.43	3.31	2.47	2.70	2.74	2.90	2.54	2.54	2.00
Er ppm	1.64	1.85	1.54	1.86	1.70	1.90	1.71	1.88	1.69	1.62	1.27
Eu ppm	0.77	0.93	0.71	0.88	0.75	0.86	0.86	0.84	0.83	0.56	0.47
Ga ppm	17.40	17.80	17.20	17.80	18.40	16.20	17.30	17.00	17.10	17.40	15.60
Gd ppm	3.10	3.19	2.62	3.31	3.07	2.78	2.95	2.80	2.98	2.66	1.94
Ge ppm	2.30	3.10	1.90	2.00	1.90	2.50	3.30	2.30	2.40	3.10	3.20
Hf ppm	1.62	1.73	1.81	1.78	1.70	2.22	1.68	2.00	1.86	1.68	1.12
Ho ppm	0.60	0.64	0.48	0.60	0.60	0.56	0.61	0.56	0.52	0.50	0.41
La ppm	10.60	15.60	8.90	14.80	15.00	15.50	11.00	16.90	15.60	7.70	5.50
Lu ppm	0.24	0.28	0.20	0.27	0.25	0.25	0.27	0.27	0.24	0.23	0.21
Nb ppm	4.34	4.89	3.22	4.64	4.91	5.71	4.97	5.33	5.02	3.50	1.86
Nd ppm	11.90	16.00	10.80	14.50	14.80	14.20	10.90	15.20	14.00	8.90	6.70
Pr ppm	2.81	3.77	2.51	3.79	3.58	3.48	2.59	3.90	3.54	2.10	1.49
Rb ppm	48.30	42.50	62.40	55.50	59.20	77.70	107.00	100.50	88.80	103.00	74.50
Sm ppm	2.84	3.52	2.38	3.21	3.51	2.95	2.74	3.41	2.58	2.40	1.58
S nppm	1.40	0.80	0.70	0.70	0.70	0.70	1.00	0.80	1.00	0.90	0.90
Sr ppm	585.00	713.00	532.00	508.00	310.00	99.80	60.30	61.70	206.00	294.00	328.00
Ta ppm	0.30	0.30	0.30	0.30	0.30	0.40	0.30	0.30	0.30	0.20	0.20
Tb ppm	0.47	0.50	0.35	0.49	0.41	0.53	0.47	0.41	0.44	0.42	0.33
Th ppm	3.84	4.02	3.47	4.36	3.92	3.91	1.37	4.69	4.30	2.58	1.98

Tm ppm	0.27	0.25	0.22	0.28	0.26	0.28	0.27	0.28	0.21	0.23	0.19
U ppm	1.14	1.66	0.81	1.45	1.74	1.10	0.72	2.16	1.78	0.50	0.36
V ppm	146.00	166.00	139.00	186.00	186.00	117.00	165.00	172.00	152.00	115.00	141.00
W ppm	0.50	<0.5	<0.5	0.60	3.60	11.20	4.00	8.70	0.50	1.80	2.90
Y ppm	15.60	16.90	14.30	16.60	16.00	16.30	16.20	15.80	15.20	14.60	11.70
Yb ppm	1.59	1.96	1.59	1.79	1.63	2.04	1.90	1.96	1.66	1.72	1.47
Zr ppm	55.00	67.00	60.00	61.00	57.00	78.00	53.00	75.00	65.00	57.00	38.00
As ppm	4.30	3.30	4.50	15.60	5.50	6.20	44.80	3.00	2.80	2.90	3.60
Bi ppm	0.08	0.03	0.12	0.11	0.07	0.10	0.30	0.04	0.02	0.57	0.20
Hg ppm	0.07	0.01	0.02	0.02	0.01	0.07	0.63	0.11	0.04	0.06	0.05
In ppm	0.11	0.02	0.04	0.01	0.01	0.02	0.04	0.02	0.02	0.17	0.12
Re ppm	0.00	0.00	0.00	0.04	0.00	0.04	0.03	0.02	0.02	0.03	0.01
Sb ppm	0.17	0.45	0.23	0.24	0.19	0.54	1.47	0.54	0.46	0.28	0.50
Sc ppm	10.90	5.00	10.90	6.10	5.30	2.60	3.30	3.30	4.50	9.80	10.20
Se ppm	3.90	0.50	1.30	3.80	0.90	3.60	8.20	1.80	1.10	7.60	8.20
Te ppm	0.11	0.01	0.03	0.06	<0.01	0.08	0.11	0.07	0.04	0.10	0.20
Tl ppm	0.03	0.03	0.03	0.03	0.04	0.07	0.17	0.07	0.08	0.05	0.05
Ag ppm	1.40	0.70	0.80	<0.5	<0.5	0.60	1.00	<0.5	0.70	4.20	3.80
Cd ppm	0.50	0.50	0.50	0.50	0.50	0.50	0.50	0.50	0.50	0.50	0.50
Co ppm	9.00	8.00	7.00	12.00	8.00	7.00	19.00	5.00	2.00	11.00	12.00
Cu ppm	2980.00	182.00	1190.00	1330.00	261.00	2440.00	3310.00	1105.00	1130.00	7180.00	7000.00
Li ppm	10.00	0.50	10.00	10.00	10.00	0.50	0.50	0.50	0.50	10.00	10.00
Mo ppm	0.50	1.00	1.00	5.00	1.00	6.00	7.00	2.00	1.00	6.00	3.00
Ni ppm	0.50	2.00	0.50	1.00	0.50	0.50	4.00	0.50	1.00	4.00	7.00
Pb ppm	9.00	7.00	5.00	11.00	9.00	3.00	9.00	5.00	4.00	12.00	8.00
Sc ppm	16.00	14.00	13.00	18.00	17.00	12.00	16.00	15.00	13.00	18.00	19.00
Zn ppm	100.00	69.00	97.00	98.00	125.00	33.00	39.00	47.00	43.00	140.00	152.00

SAMPLES	SSD23LZ059	SSD23LZ060	SSD23LZ061	SSD23LZ063	SSD23LZ064	SSD23LZ066	SSD23LZ069	SSD23LZ074	SSD23LZ076	SSD23LZ077	SSD23LZ079
	Porphyry										
Rock Type	Intrusion										
Lithology Code	FQMP I1	FQMP I2									
Ва ррт	1485.00	2400.00	1500.00	1490.00	1720.00	1355.00	1650.00	1625.00	2050.00	1485.00	1450.00
Ce ppm	13.30	16.00	17.10	12.30	17.70	14.30	13.00	12.40	13.00	22.50	20.70
Cr ppm	8.00	10.00	7.00	9.00	7.00	6.00	5.00	7.00	8.00	6.00	6.00
Cs ppm	0.97	0.98	1.18	0.68	1.16	0.88	0.47	0.83	0.97	2.03	1.14
Dy ppm	1.49	1.62	2.29	1.56	2.55	2.23	1.74	2.29	2.30	2.76	2.76
Er ppm	1.04	0.99	1.46	1.05	1.69	1.44	1.19	1.55	1.52	1.71	1.86
Eu ppm	0.48	0.50	0.65	0.48	0.74	0.73	0.48	0.56	0.61	0.86	0.79
Ga ppm	17.30	11.80	17.00	13.20	15.40	16.00	16.80	14.20	15.70	17.20	17.60
Gd ppm	1.48	1.75	1.98	1.63	2.44	2.36	1.97	2.34	2.51	3.16	2.94
Ge ppm	2.40	2.30	2.80	2.60	2.70	2.40	2.50	2.30	2.40	2.50	2.40
Hf ppm	1.88	1.67	1.62	1.87	2.07	1.82	1.71	1.48	2.10	1.92	1.74
Ho ppm	0.35	0.34	0.49	0.34	0.56	0.48	0.39	0.50	0.49	0.59	0.56
La ppm	6.70	8.20	8.50	6.70	9.50	6.80	6.60	5.80	6.10	11.80	10.20
Lu ppm	0.19	0.17	0.20	0.19	0.30	0.25	0.22	0.28	0.26	0.31	0.29
Nb ppm	2.75	3.49	4.29	3.81	4.55	2.70	1.86	1.88	1.68	4.11	3.61
Nd ppm	6.90	7.80	8.70	6.60	10.30	9.00	8.10	8.30	8.70	12.70	12.30
Pr ppm	1.69	1.95	2.18	1.64	2.42	1.93	1.75	1.90	1.97	3.04	2.94
Rb ppm	91.10	106.00	89.10	82.80	82.10	73.20	83.00	69.10	83.20	54.20	47.80
Sm ppm	1.53	1.76	1.93	1.56	2.36	2.17	1.88	2.20	2.36	2.94	3.42
S nppm	0.90	0.60	1.40	0.80	0.90	0.90	1.30	1.00	1.20	1.00	1.10
Sr ppm	348.00	401.00	286.00	286.00	403.00	306.00	267.00	337.00	363.00	632.00	627.00
Та ррт	0.20	0.30	0.30	0.30	0.30	0.20	0.20	0.20	0.20	0.30	0.40
Tb ppm	0.23	0.28	0.37	0.27	0.44	0.36	0.29	0.38	0.38	0.44	0.47
Th ppm	2.75	2.74	3.12	2.42	3.22	2.87	2.44	2.82	3.37	3.43	3.77
Tm ppm	0.15	0.17	0.21	0.14	0.24	0.20	0.17	0.21	0.21	0.24	0.25
U ppm	0.64	0.61	0.78	0.74	0.80	0.80	0.59	0.45	0.57	1.11	1.00

	l		1		105.00	105.00	1	1	100.00	1	1
V ppm	98.00	67.00	114.00	82.00	105.00	105.00	114.00	104.00	122.00	164.00	151.00
W ppm	2.40	3.20	4.00	1.20	3.00	3.30	1.50	1.40	2.40	1.90	1.80
Y ppm	9.80	9.80	12.80	10.40	16.00	14.00	11.20	13.60	14.00	16.40	16.30
Yb ppm	1.20	1.17	1.48	1.09	1.79	1.56	1.35	1.47	1.51	1.84	1.86
Zr ppm	64.00	58.00	60.00	70.00	75.00	63.00	61.00	52.00	78.00	67.00	61.00
As ppm	2.30	16.90	2.40	1.70	2.80	2.60	2.40	3.00	4.10	4.40	2.50
Bi ppm	0.14	0.68	0.18	0.13	0.13	0.08	0.11	0.07	0.09	0.07	0.03
Hg ppm	0.05	0.05	0.07	0.04	0.06	0.01	0.06	0.06	0.05	0.01	0.02
In ppm	0.10	0.20	0.15	0.06	0.10	0.03	0.10	0.14	0.13	0.06	0.04
Re ppm	0.01	0.07	0.02	0.01	0.05	0.00	0.00	0.00	0.00	0.01	0.00
Sb ppm	0.26	0.26	0.33	0.15	0.29	0.22	0.20	0.28	0.24	0.24	0.19
Sc ppm	2.60	3.30	4.80	3.60	5.40	5.00	5.90	6.10	8.10	11.10	9.80
Se ppm	3.90	8.70	4.80	4.00	6.20	1.40	2.40	4.40	4.30	1.80	1.80
Te ppm	0.08	0.10	0.06	0.07	0.06	0.04	0.08	0.04	0.14	0.05	0.03
Tl ppm	0.04	0.06	0.06	0.05	0.05	0.06	0.04	0.06	0.03	0.03	0.02
Ag ppm	3.20	1.70	3.60	1.70	2.60	0.70	1.50	1.90	2.30	1.00	1.30
Cd ppm	0.50	0.50	0.50	0.50	0.50	0.50	0.50	0.50	0.50	0.50	0.50
Co ppm	5.00	21.00	10.00	6.00	11.00	6.00	6.00	7.00	8.00	7.00	10.00
Cu ppm	5350.00	3370.00	8090.00	4300.00	3990.00	1945.00	2830.00	4680.00	4940.00	1760.00	2520.00
Li ppm	0.50	0.50	0.50	10.00	0.50	10.00	10.00	10.00	10.00	10.00	10.00
Mo ppm	4.00	25.00	3.00	6.00	13.00	2.00	1.00	1.00	1.00	1.00	1.00
Ni ppm	1.00	11.00	1.00	3.00	2.00	0.50	2.00	2.00	1.00	2.00	1.00
Pb ppm	7.00	11.00	8.00	7.00	10.00	10.00	12.00	10.00	9.00	8.00	7.00
Sc ppm	8.00	9.00	11.00	10.00	11.00	12.00	11.00	12.00	14.00	16.00	15.00
Zn ppm	113.00	84.00	122.00	170.00	136.00	138.00	143.00	108.00	127.00	91.00	106.00

SAMPLES	SSD23LZ080	SSD23LZ082	SSD23LZ085	SSD23LZ089	SSD23LZ092	SSD23LZ094	SSD23LZ095	SSD23LZ096	SSD23LZ101	SSD23LZ102	SSD23LZ103
Rock Type	Porphyry Intrusion	Andesitic - dacite	Andesitic - dacite	Andesitic - dacite	Porphyry Intrusion	Porphyry Intrusion	Porphyry Intrusion	Porphyry Intrusion	Porphyry Intrusion	Porphyry Intrusion	Andesitic - dacite
Lithology Code	FQMP I3	Volcanic- Volcaniclasti c rock	Volcanic- Volcaniclasti c rock	Volcanic- Volcaniclasti c rock	FQMP I2	FQMP I2	FQMP I2	FQMP I2	FQMP I4	FQMP I4	Volcanic- Volcaniclasti c rock
Ba ppm	1065.00	641.00	1185.00	514.00	748.00	721.00	643.00	1320.00	243.00	256.00	2140.00
Ce ppm	14.80	23.90	28.00	25.10	16.80	21.40	29.90	24.10	34.30	32.00	36.10
Cr ppm	5.00	5.00	5.00	6.00	6.00	5.00	5.00	5.00	5.00	5.00	6.00
Cs ppm	1.76	1.77	1.68	1.98	1.72	1.27	1.58	0.82	3.39	3.54	2.73
Dy ppm	2.17	2.53	2.56	2.70	2.39	2.35	2.95	2.45	2.51	2.79	3.32
Er ppm	1.44	1.59	1.59	1.63	1.60	1.54	1.85	1.64	1.58	1.76	2.07
Eu ppm	0.66	0.85	0.82	0.70	0.53	0.66	1.10	0.70	0.92	0.97	0.98
Ga ppm	17.60	14.70	16.60	18.20	18.20	17.40	16.30	17.90	16.60	16.90	17.40
Gd ppm	2.52	3.00	3.03	2.96	2.49	2.82	3.48	2.96	3.02	3.15	3.37
Ge ppm	2.00	1.70	2.10	2.10	2.20	1.80	1.80	2.20	2.00	1.70	2.10
Hf ppm	1.78	1.65	1.80	1.88	2.06	1.58	1.74	1.80	1.98	1.88	2.61
Ho ppm	0.48	0.52	0.53	0.56	0.52	0.48	0.61	0.50	0.53	0.59	0.68
La ppm	7.50	12.90	16.20	13.60	8.10	10.90	15.90	12.40	19.30	18.40	21.20
Lu ppm	0.23	0.27	0.25	0.27	0.29	0.23	0.28	0.26	0.30	0.29	0.35
Nb ppm	4.71	4.27	5.18	4.99	3.97	4.67	9.84	6.37	5.65	6.33	6.54
Nd ppm	9.50	13.20	14.40	13.80	10.60	12.20	16.60	13.60	17.10	16.60	16.80
Pr ppm	2.10	3.30	3.46	3.38	2.36	3.04	3.98	3.32	4.39	4.11	4.33
Rb ppm	55.80	78.80	53.50	60.40	75.40	62.50	60.90	58.30	80.80	80.90	81.20
Sm ppm	2.26	3.15	3.36	3.09	2.39	3.02	3.80	2.94	3.50	3.55	3.72
S nppm	0.60	0.80	0.60	0.50	0.70	1.00	0.70	0.50	1.40	0.90	1.60
Sr ppm	482.00	260.00	537.00	304.00	256.00	402.00	428.00	751.00	116.00	168.00	178.50
Ta ppm	0.30	0.30	0.30	0.30	0.30	0.30	0.30	0.30	0.30	0.40	0.40
Tb ppm	0.38	0.44	0.44	0.46	0.41	0.41	0.48	0.43	0.43	0.48	0.52
Th ppm	3.68	3.19	4.13	3.48	3.73	3.86	3.79	3.83	3.92	3.89	3.98
Tm ppm	0.20	0.23	0.23	0.25	0.23	0.19	0.26	0.23	0.23	0.25	0.30

U ppm	0.95	1.34	1.32	1.14	0.82	0.98	1.36	1.03	1.98	1.94	2.33
V ppm	149.00	155.00	172.00	171.00	192.00	142.00	179.00	170.00	194.00	197.00	128.00
W ppm	2.20	4.30	1.60	2.30	2.40	2.10	1.60	1.20	4.00	2.30	3.50
Y ppm	13.80	15.90	15.80	16.40	15.20	14.80	18.20	15.80	15.20	17.00	19.00
Yb ppm	1.49	1.59	1.80	1.74	1.71	1.44	1.83	1.49	1.77	1.74	2.18
Zr ppm	63.00	56.00	66.00	68.00	69.00	53.00	61.00	65.00	71.00	67.00	93.00
As ppm	3.00	3.00	3.40	3.80	2.60	3.20	1.80	3.00	7.40	4.70	1.10
Bi ppm	0.08	2.41	0.09	0.06	0.16	0.56	0.13	0.03	0.65	0.07	0.16
Hg ppm	0.01	0.10	0.06	0.08	0.02	0.03	0.02	0.01	0.03	0.01	0.03
In ppm	0.05	0.05	0.01	0.01	0.05	0.07	0.02	0.01	0.04	0.04	0.01
Re ppm	0.00	0.03	0.04	0.01	0.00	0.01	0.00	0.08	0.01	0.01	0.06
Sb ppm	0.25	0.66	0.38	0.50	0.34	0.40	0.29	0.33	0.38	0.58	0.20
Sc ppm	5.20	4.20	6.60	6.20	4.50	5.70	9.10	10.10	5.50	6.30	3.30
Se ppm	1.50	4.60	2.80	1.70	1.70	4.10	2.00	1.00	1.60	0.50	1.50
Te ppm	0.07	0.58	0.05	0.04	0.04	0.28	0.05	0.03	0.31	0.01	0.06
Tl ppm	0.03	0.09	0.05	0.06	0.05	0.06	0.06	0.04	0.07	0.07	0.11
Ag ppm	0.60	1.40	0.60	<0.5	0.90	1.60	0.60	0.70	0.50	0.50	0.50
Cd ppm	0.50	0.50	0.50	0.50	0.50	0.50	0.50	0.50	0.50	0.50	0.50
Co ppm	9.00	16.00	10.00	10.00	6.00	10.00	8.00	6.00	14.00	9.00	8.00
Cu ppm	1760.00	4210.00	1060.00	1455.00	2450.00	4610.00	1270.00	1090.00	216.00	261.00	180.00
Li ppm	10.00	10.00	10.00	10.00	10.00	10.00	10.00	10.00	10.00	10.00	10.00
Mo ppm	2.00	5.00	8.00	2.00	1.00	1.00	1.00	46.00	2.00	2.00	9.00
Ni ppm	0.50	0.50	1.00	0.50	2.00	2.00	1.00	1.00	0.50	0.50	4.00
Pb ppm	5.00	8.00	4.00	3.00	6.00	6.00	5.00	3.00	8.00	7.00	6.00
Sc ppm	16.00	16.00	16.00	16.00	15.00	14.00	17.00	16.00	18.00	16.00	12.00
Zn ppm	85.00	51.00	48.00	62.00	62.00	56.00	68.00	57.00	119.00	61.00	77.00

Sample ID	206/238 Age	2σ	207Pb/235U	2σ	206Pb/238U	2σ	238U/206Pb	2σ	207Pb/206Pb	2σ	U (ppm)	2σ	Th (ppm)	2σ	Pb (ppm)	2σ	U/Th	2σ
SSD23LZ005GR_1C	250.1	7.8	0.27	0.04	0.04	0.00	25.86	0.81	0.05	0.0	564.8	48.0	162.4	14.7	21.2	3.4	3.4	0.1
SSD23LZ005GR_57	241.6	8.8	0.27	0.04	0.04	0.00	26.57	0.93	0.05	0.0	494.2	27.9	224.5	11.5	28.1	2.8	2.1	0.1
SSD23LZ005GR_1R	231.8	7.3	0.24	0.03	0.04	0.00	27.95	0.91	0.05	0.0	714.4	21.6	307.4	8.3	34.6	2.6	2.3	0.1
SSD23LZ005GR_25	230.8	15.7	0.24	0.05	0.04	0.00	28.44	1.84	0.05	0.0	197.8	7.3	62.7	2.9	5.2	0.8	3.2	0.1
SSD23LZ005GR_20	228.9	22.2	0.28	0.09	0.04	0.00	29.08	2.71	0.06	0.0	195.3	12.7	49.6	3.2	4.7	1.6	4.0	0.2
SSD23LZ005GR_45	228.5	11.9	0.25	0.03	0.04	0.00	28.59	1.43	0.05	0.0	384.4	52.1	97.2	16.4	8.5	1.7	4.2	0.3
SSD23LZ005GR_19	226.2	9.5	0.25	0.04	0.04	0.00	28.84	1.24	0.05	0.0	507.1	32.4	202.4	15.5	19.0	2.7	2.6	0.1
SSD23LZ005GR_51	224.1	9.2	0.28	0.05	0.04	0.00	28.49	1.02	0.06	0.0	469.0	24.7	111.3	8.3	11.7	1.7	4.2	0.1
SSD23LZ005GR_3	222.1	10.9	0.22	0.05	0.04	0.00	29.24	1.61	0.04	0.0	289.0	17.1	75.8	6.6	7.5	1.5	3.8	0.1
SSD23LZ005GR_2	221.9	13.1	0.29	0.07	0.04	0.00	29.91	1.90	0.05	0.0	261.0	10.7	60.1	2.4	5.8	1.2	4.3	0.1
SSD23LZ005GR_55	221.3	12.1	0.27	0.04	0.03	0.00	29.56	1.69	0.06	0.0	411.2	20.6	115.2	6.4	12.1	1.9	3.5	0.1
SSD23LZ005GR_63	218.4	10.7	0.21	0.04	0.03	0.00	29.67	1.53	0.04	0.0	338.5	22.5	83.5	6.4	6.5	1.4	4.1	0.1
SSD23LZ005GR_44	218.2	11.3	0.23	0.05	0.03	0.00	30.03	1.59	0.05	0.0	249.2	14.6	56.7	4.4	4.4	1.0	4.5	0.2
SSD23LZ005GR_30	218.0	10.2	0.23	0.05	0.03	0.00	30.07	1.52	0.05	0.0	240.8	7.2	52.9	1.9	5.0	1.0	4.6	0.1
SSD23LZ005GR_62	215.8	15.9	0.19	0.05	0.03	0.00	30.16	1.93	0.04	0.0	196.0	27.1	42.9	7.4	3.9	1.2	4.7	0.2
SSD23LZ005GR_41	215.3	9.2	0.23	0.05	0.03	0.00	30.20	1.31	0.05	0.0	359.2	24.4	101.1	9.1	8.2	1.3	3.6	0.2
SSD23LZ005GR_10	215.2	14.1	0.23	0.05	0.03	0.00	31.09	2.15	0.05	0.0	235.5	18.0	55.3	4.9	4.8	1.0	4.3	0.2
SSD23LZ005GR_60	212.3	12.6	0.29	0.06	0.03	0.00	30.86	1.94	0.06	0.0	257.4	20.0	61.8	7.0	6.7	1.5	4.2	0.2
SSD23LZ005GR_52	212.2	10.5	0.21	0.06	0.03	0.00	30.71	1.59	0.04	0.0	234.3	28.3	56.7	7.7	5.1	1.1	4.2	0.1
SSD23LZ005GR_65	212.1	11.5	0.27	0.05	0.03	0.00	30.64	1.67	0.05	0.0	332.7	19.4	116.8	8.9	10.8	1.9	2.9	0.1
SSD23LZ005GR_49	211.4	9.8	0.23	0.05	0.03	0.00	30.32	1.34	0.05	0.0	372.6	18.8	136.8	9.9	12.5	1.8	2.7	0.1
SSD23LZ005GR_36	211.2	6.3	0.23	0.03	0.03	0.00	30.56	0.97	0.05	0.0	639.6	35.6	291.7	22.1	25.0	3.5	2.2	0.1
SSD23LZ005GR_7	211.2	10.0	0.24	0.04	0.03	0.00	31.11	1.56	0.05	0.0	304.6	5.7	74.9	1.4	6.9	0.9	4.0	0.1
SSD23LZ005GR_29	210.6	12.0	0.23	0.06	0.03	0.00	30.85	1.75	0.05	0.0	262.8	11.7	46.9	2.8	4.2	0.9	5.8	0.2
SSD23LZ005GR_35	210.4	9.8	0.22	0.04	0.03	0.00	31.15	1.59	0.05	0.0	346.2	10.6	91.5	3.5	7.7	1.5	3.8	0.1
SSD23LZ005GR_4	210.4	10.5	0.25	0.05	0.03	0.00	31.20	1.48	0.05	0.0	246.1	11.9	78.6	5.1	7.9	1.2	3.1	0.2
SSD23LZ005GR_58	209.2	10.4	0.22	0.05	0.03	0.00	30.68	1.51	0.05	0.0	231.8	7.0	76.0	2.4	7.1	1.0	3.0	0.1
SSD23LZ005GR_26	208.2	8.6	0.22	0.04	0.03	0.00	31.36	1.38	0.06	0.0	298.6	18.5	118.4	7.0	11.1	1.4	2.6	0.1
SSD23LZ005GR_54	208.0	10.5	0.21	0.05	0.03	0.00	31.34	1.64	0.05	0.0	271.4	8.4	59.2	3.5	6.6	1.3	4.6	0.1

]		l	I		Ì		I	ĺ	1	ĺ	ĺ	l		I	ĺ	1	ĺ	Ì
SSD23LZ005GR_66	206.6	9.7	0.25	0.04	0.03	0.00	30.90	1.33	0.05	0.0	433.4	27.6	157.9	9.8	15.8	2.1	2.7	0.1
SSD23LZ005GR_43	206.0	9.3	0.25	0.05	0.03	0.00	31.63	1.45	0.06	0.0	349.2	13.1	109.5	7.6	10.4	1.5	3.2	0.1
SSD23LZ005GR_61	205.8	10.6	0.23	0.05	0.03	0.00	31.18	1.64	0.05	0.0	265.4	21.5	69.8	8.1	9.5	1.7	3.9	0.2
SSD23LZ005GR_28	204.7	11.1	0.23	0.05	0.03	0.00	31.72	1.60	0.05	0.0	299.5	4.9	82.7	2.3	6.7	1.0	3.7	0.1
SSD23LZ005GR_59	204.4	9.3	0.24	0.04	0.03	0.00	31.74	1.55	0.05	0.0	357.9	18.8	80.4	4.2	6.2	1.1	4.3	0.1
SSD23LZ005GR_64	204.2	7.8	0.25	0.06	0.03	0.00	31.13	1.18	0.05	0.0	348.9	11.8	79.5	4.9	7.3	1.2	4.4	0.1
SSD23LZ005GR_40	204.1	12.6	0.19	0.05	0.03	0.00	32.51	2.13	0.05	0.0	279.1	14.3	66.6	4.3	6.2	1.3	4.2	0.1
SSD23LZ005GR_6	204.0	15.5	0.28	0.09	0.03	0.00	32.52	2.26	0.06	0.0	193.5	31.5	46.1	9.8	4.4	1.2	4.5	0.3
SSD23LZ005GR_47	202.9	9.6	0.24	0.04	0.03	0.00	32.17	1.55	0.06	0.0	363.4	20.5	128.0	8.5	10.9	1.7	2.8	0.1
SSD23LZ005GR_32	200.9	13.1	0.22	0.06	0.03	0.00	33.18	2.11	0.06	0.0	142.6	4.3	43.5	2.1	3.9	0.9	3.4	0.1
SSD23LZ005GR_24	199.2	9.3	0.20	0.05	0.03	0.00	32.53	1.72	0.05	0.0	268.6	15.6	83.0	3.6	8.2	1.3	3.3	0.1
Sample ID	206/238 Age	2σ	207Pb/235U	2σ	206Pb/238U	2σ	238U/206Pb	2σ	207Pb/206Pb	2σ	U (ppm)	2σ	Th (ppm)	2σ	Pb (ppm)	2σ	U/Th	2σ
SSD23LZ006GR 44	212.7	9.7	0.26	0.04	0.03	0.00	30.04	1.36	0.05	0.01	561.6	40.1	206.5	14.8	23.2	2.4	2.7	0.0
SSD23LZ006GR 76	212.7	12.4	0.28	0.05	0.03	0.00	30.40	1.72	0.06	0.01	282.3	24.1	85.0	9.0	10.3	1.7	3.3	0.0
SSD23LZ000GR_70	212.7	8.5	0.24	0.04	0.03	0.00	30.00	1.72	0.05	0.01	390.5	26.8	126.1	7.3	11.2	1.5	3.1	0.1
	212.3		0.22	0.03		0.00	30.25	1.28	0.04	0.01	500.1	9.2	85.5	9.8	10.0	1.6		0.1
SSD23LZ006GR_3	212.3	6.7	0.23	0.05	0.03	0.00	29.99	0.93	0.05	0.01	450.4	21.3		7.3		1.9	3.4	0.7
SSD23LZ006GR_8													137.5		15.6			
SSD23LZ006GR_52	211.5	8.3	0.26	0.04	0.03	0.00	30.09	1.17	0.05	0.01	459.0	24.4	173.7	10.8	17.6	2.3	2.6	0.0
SSD23LZ006GR_25	210.7	13.1	0.24	0.06	0.03	0.00	30.98	2.22	0.06	0.01	233.6	5.8	66.5	2.7	5.7	1.2	3.6	0.1
SSD23LZ006GR_22	210.0	10.7	0.20	0.04	0.03	0.00	30.20	1.53	0.05	0.01	330.6	23.4	42.8	2.4	4.1	0.8	7.8	0.4
SSD23LZ006GR_24	208.5	8.6	0.23	0.04	0.03	0.00	30.61	1.28	0.05	0.01	418.5	7.9	186.4	7.5	18.8	2.5	2.3	0.1
SSD23LZ006GR_41	208.3	11.5	0.27	0.07	0.03	0.00	30.99	1.79	0.06	0.01	199.1	12.2	46.6	3.1	4.6	0.9	4.4	0.1
SSD23LZ006GR_68	208.2	10.8	0.18	0.05	0.03	0.00	30.97	1.76	0.05	0.01	206.8	8.3	55.4	1.1	6.4	1.2	3.6	0.1
SSD23LZ006GR_47	208.2	10.8	0.23	0.05	0.03	0.00	30.89	1.61	0.05	0.01	199.5	20.3	50.9	6.6	5.2	1.1	4.0	0.1
SSD23LZ006GR_70	208.0	9.2	0.23	0.06	0.03	0.00	30.78	1.48	0.05	0.01	229.2	4.0	56.2	1.6	5.3	1.2	3.9	0.1
SSD23LZ006GR_43	207.5	8.6	0.23	0.04	0.03	0.00	30.42	1.37	0.05	0.01	328.4	12.7	96.6	3.3	9.7	1.3	3.4	0.1
SSD23LZ006GR_10	207.4	11.1	0.26	0.06	0.03	0.00	30.73	1.48	0.06	0.01	225.4	10.5	76.2	4.2	6.7	1.2	3.0	0.1
SSD23LZ006GR_21	207.3	12.1	0.23	0.04	0.03	0.00	31.32	1.93	0.06	0.01	210.3	13.9	44.5	4.2	4.3	0.9	4.9	0.2
SSD23LZ006GR_59	207.1	8.3	0.22	0.04	0.03	0.00	30.81	1.33	0.05	0.01	249.2	14.6	80.7	4.9	8.1	1.2	2.9	0.0
SSD23LZ006GR_60	206.8	18.6	0.25	0.05	0.03	0.00	30.91	2.57	0.05	0.01	529.9	17.8	217.7	6.7	19.0	3.4	2.3	0.1

SSD23LZ006GR 1	200.0	10.8	0.21	0.05	0.03	0.00	31.40	1.69	0.04	0.01	273.1	13.6	07.5		10.7	1.7	3.2	0.1
_	206.8												87.5	5.7				
SSD23LZ006GR_50	206.7	10.1	0.22	0.05	0.03	0.00	31.04	1.51	0.04	0.01	319.1	11.1	121.1	15.0	11.4	2.0	2.9	0.3
SSD23LZ006GR_69	206.7	8.2	0.25	0.04	0.03	0.00	30.84	1.22	0.06	0.01	281.4	12.3	74.8	2.9	7.3	1.2	3.6	0.1
SSD23LZ006GR_37	205.6	9.2	0.23	0.04	0.03	0.00	31.09	1.43	0.05	0.01	315.9	29.3	82.9	5.2	7.6	1.2	3.8	0.2
SSD23LZ006GR_17	204.3	10.7	0.25	0.06	0.03	0.00	31.63	1.76	0.06	0.01	290.1	10.0	77.4	2.5	7.3	1.1	3.8	0.1
SSD23LZ006GR_51	203.8	12.3	0.20	0.06	0.03	0.00	31.78	1.85	0.04	0.01	146.8	8.2	38.9	2.0	3.0	0.7	3.7	0.1
SSD23LZ006GR_29	202.3	7.1	0.20	0.03	0.03	0.00	31.08	0.98	0.05	0.01	447.0	28.8	107.4	6.3	9.8	1.5	4.2	0.1
SSD23LZ006GR_61	202.1	14.3	0.27	0.06	0.03	0.00	32.67	2.58	0.06	0.01	120.2	12.6	35.9	5.5	3.9	0.8	3.3	0.2
SSD23LZ006GR_78	201.2	9.6	0.20	0.05	0.03	0.00	31.47	1.38	0.05	0.01	173.1	7.6	39.6	1.8	4.1	0.8	4.4	0.1
SSD23LZ006GR_45	200.8	9.5	0.22	0.04	0.03	0.00	31.45	1.35	0.05	0.01	279.8	14.6	77.4	4.6	8.1	1.5	3.6	0.1
SSD23LZ006GR_80	200.2	9.9	0.24	0.05	0.03	0.00	32.10	1.67	0.05	0.01	266.7	20.9	101.6	10.4	10.6	1.6	2.7	0.1
SSD23LZ006GR_15	200.2	12.2	0.26	0.05	0.03	0.00	32.53	1.93	0.06	0.01	262.3	8.2	63.8	2.3	4.6	0.9	4.2	0.1
SSD23LZ006GR_40	199.8	9.7	0.25	0.05	0.03	0.00	32.15	1.65	0.05	0.01	340.4	22.5	87.6	10.1	7.8	1.4	4.1	0.2
SSD23LZ006GR_72	197.9	9.4	0.24	0.05	0.03	0.00	32.43	1.57	0.06	0.01	279.0	14.0	81.4	4.8	8.4	1.3	3.3	0.1
\$\$D3317006CD_66	107.3		0.24	0.04	0.03	0.00	32.50	1.50	0.06	0.01	341.6	31.3	45.6	2.2	3.7	0.6	7.0	0.4
SSD23LZ006GR_66	197.2	8.8	0.24	0.04	0.03	0.00	32.30	1.50	0.06	0.01	341.0	31.3	43.0	2.2	3.7	0.0	7.0	
Sample ID	206/238 Age	2σ	207Pb/235U	2σ	206Pb/238U	2σ	238U/206Pb	2σ	207Pb/206Pb	2σ		2σ		2.2		2σ	U/Th	2σ
Sample ID	206/238 Age	2σ	207Pb/235U	2σ	206Pb/238U	2σ	238U/206Pb	2σ	207Pb/206Pb	2σ	U (ppm)	2σ	Th (ppm)	2σ	Pb (ppm)	2σ	U/Th	2σ
Sample ID SSD23LZ047G_56	206/238 Age 216.7	2 σ 14.2	207Pb/235U 0.29	2 σ	206Pb/238U 0.03		238U/206Pb 29.70	2 σ 2.00	207Pb/206Pb 0.06	2 σ	U (ppm)	2 σ 15.9	Th (ppm)	2 σ 2.6	Pb (ppm) 3.6	2 σ	U/Th 4.3	2 σ
Sample ID SSD23LZ047G_56 SSD23LZ047G_34	206/238 Age 216.7 215.9	2 σ 14.2 7.0	207Pb/235U 0.29 0.23	2 σ 0.08 0.03	206Pb/238U 0.03 0.03	2 σ 0.00 0.00	238U/206Pb 29.70 29.02	2 σ 2.00 0.93	207Pb/206Pb 0.06 0.05	2 σ 0.02 0.01	U (ppm) 160.8 601.0	2 σ 15.9 54.1	Th (ppm) 36.7 195.1	2 σ 2.6 23.0	Pb (ppm) 3.6 19.6	2 σ 0.8 2.8	U/Th 4.3 3.2	2 σ 0.2 0.2
Sample ID SSD23LZ047G_56 SSD23LZ047G_34 SSD23LZ047G_7	206/238 Age 216.7 215.9 214.0	2σ 14.2 7.0 8.9	207Pb/235U 0.29 0.23 0.25	2σ 0.08 0.03 0.05	206Pb/238U 0.03 0.03	2σ 0.00 0.00 0.00	238U/206Pb 29.70 29.02 29.51	2σ 2.00 0.93 1.41	207Pb/206Pb 0.06 0.05	2σ 0.02 0.01 0.01	U (ppm) 160.8 601.0 261.8	2σ 15.9 54.1 20.6	Th (ppm) 36.7 195.1 55.3	2σ 2.6 23.0 4.1	Pb (ppm) 3.6 19.6 7.9	2σ 0.8 2.8	U/Th 4.3 3.2 4.7	2σ 0.2 0.2
Sample ID SSD23LZ047G_56 SSD23LZ047G_34 SSD23LZ047G_7 SSD23LZ047G_60	206/238 Age 216.7 215.9 214.0 213.6	2σ 14.2 7.0 8.9	207Pb/235U 0.29 0.23 0.25	2σ 0.08 0.03 0.05	206Pb/238U 0.03 0.03 0.03	2σ 0.00 0.00 0.00	238U/206Pb 29.70 29.02 29.51 29.48	2σ 2.00 0.93 1.41 1.21	207Pb/206Pb 0.06 0.05 0.05 0.06	2σ 0.02 0.01 0.01	U (ppm) 160.8 601.0 261.8 301.2	2σ 15.9 54.1 20.6 8.8	Th (ppm) 36.7 195.1 55.3 94.6	2σ 2.6 23.0 4.1 3.1	Pb (ppm) 3.6 19.6 7.9 9.2	2σ 0.8 2.8 1.3	U/Th 4.3 3.2 4.7 3.1	2σ 0.2 0.2 0.1
Sample ID SSD23LZ047G_56 SSD23LZ047G_34 SSD23LZ047G_7 SSD23LZ047G_60 SSD23LZ047G_28	206/238 Age 216.7 215.9 214.0 213.6 213.0	26 14.2 7.0 8.9 8.6 10.2	0.29 0.23 0.25 0.25	2σ 0.08 0.03 0.05 0.05	206Pb/238U 0.03 0.03 0.03 0.03 0.03	2σ 0.00 0.00 0.00 0.00 0.00	238U/206Pb 29.70 29.02 29.51 29.48 29.44	2σ 2.00 0.93 1.41 1.21 1.33	207Pb/206Pb 0.06 0.05 0.05 0.06 0.06	2σ 0.02 0.01 0.01 0.01 0.01	U (ppm) 160.8 601.0 261.8 301.2 237.6	2σ 15.9 54.1 20.6 8.8 7.3	Th (ppm) 36.7 195.1 55.3 94.6 68.5	26 23.0 4.1 3.1 2.9	Pb (ppm) 3.6 19.6 7.9 9.2 6.9	2σ 0.8 2.8 1.3 1.5	U/Th 4.3 3.2 4.7 3.1 3.4	2σ 0.2 0.2 0.1 0.1
Sample ID SSD23LZ047G_56 SSD23LZ047G_34 SSD23LZ047G_7 SSD23LZ047G_60 SSD23LZ047G_28 SSD23LZ047G_20	206/238 Age 216.7 215.9 214.0 213.6 213.0 211.2	2σ 14.2 7.0 8.9 8.6 10.2	207Pb/235U 0.29 0.23 0.25 0.25 0.21 0.26	2σ 0.08 0.03 0.05 0.05 0.05	206Pb/238U 0.03 0.03 0.03 0.03 0.03 0.03	2σ 0.00 0.00 0.00 0.00 0.00	238U/206Pb 29.70 29.02 29.51 29.48 29.44 30.77	2σ 2.00 0.93 1.41 1.21 1.33 2.53	207Pb/206Pb 0.06 0.05 0.05 0.06 0.04 0.05	2σ 0.02 0.01 0.01 0.01 0.01	U (ppm) 160.8 601.0 261.8 301.2 237.6 176.2	2σ 15.9 54.1 20.6 8.8 7.3	Th (ppm) 36.7 195.1 55.3 94.6 68.5 36.4	2σ 2.6 23.0 4.1 3.1 2.9	Pb (ppm) 3.6 19.6 7.9 9.2 6.9 4.7	2σ 0.8 2.8 1.3 1.5 1.1	U/Th 4.3 3.2 4.7 3.1 3.4 4.9	2σ 0.2 0.2 0.1 0.1 0.1
Sample ID SSD23LZ047G_56 SSD23LZ047G_34 SSD23LZ047G_7 SSD23LZ047G_60 SSD23LZ047G_28 SSD23LZ047G_20 SSD23LZ047G_9	206/238 Age 216.7 215.9 214.0 213.6 213.0 211.2 210.9	2σ 14.2 7.0 8.9 8.6 10.2 15.0	0.29 0.23 0.25 0.25 0.21 0.26	2σ 0.08 0.03 0.05 0.05 0.05 0.05	206Pb/238U 0.03 0.03 0.03 0.03 0.03 0.03 0.03	2σ 0.00 0.00 0.00 0.00 0.00 0.00	238U/206Pb 29.70 29.02 29.51 29.48 29.44 30.77 30.12	2σ 2.00 0.93 1.41 1.21 1.33 2.53	207Pb/206Pb 0.06 0.05 0.06 0.06 0.06 0.06 0.06 0.04 0.05	2σ 0.02 0.01 0.01 0.01 0.01 0.01	U (ppm) 160.8 601.0 261.8 301.2 237.6 176.2 315.7	2σ 15.9 54.1 20.6 8.8 7.3 7.0	Th (ppm) 36.7 195.1 55.3 94.6 68.5 36.4 103.5	2.6 23.0 4.1 3.1 2.9 3.6 4.8	Pb (ppm) 3.6 19.6 7.9 9.2 6.9 4.7 10.6	26 0.8 2.8 1.3 1.5 1.1	U/Th 4.3 3.2 4.7 3.1 3.4 4.9 3.0	0.2 0.2 0.1 0.1 0.1 0.3
Sample ID SSD23LZ047G_56 SSD23LZ047G_34 SSD23LZ047G_7 SSD23LZ047G_60 SSD23LZ047G_28 SSD23LZ047G_20 SSD23LZ047G_9 SSD23LZ047G_9	206/238 Age 216.7 215.9 214.0 213.6 213.0 211.2 210.9 209.9	2σ 14.2 7.0 8.9 8.6 10.2 15.0 8.0	0.29 0.23 0.25 0.25 0.21 0.26 0.25	2σ 0.08 0.03 0.05 0.05 0.05 0.07 0.05	206Pb/238U 0.03 0.03 0.03 0.03 0.03 0.03 0.03 0.03	2σ 0.00 0.00 0.00 0.00 0.00 0.00 0.00	238U/206Pb 29.70 29.02 29.51 29.48 29.44 30.77 30.12 29.65	2.00 0.93 1.41 1.21 1.33 2.53 1.20	207Pb/206Pb 0.06 0.05 0.05 0.06 0.04 0.05 0.05 0.05	2σ 0.02 0.01 0.01 0.01 0.01 0.01 0.01	U (ppm) 160.8 601.0 261.8 301.2 237.6 176.2 315.7 336.9	2σ 15.9 54.1 20.6 8.8 7.3 7.0 10.5	Th (ppm) 36.7 195.1 55.3 94.6 68.5 36.4 103.5 104.4	26 2.6 23.0 4.1 3.1 2.9 3.6 4.8	Pb (ppm) 3.6 19.6 7.9 9.2 6.9 4.7 10.6 10.9	2σ 0.8 2.8 1.3 1.5 1.1 1.4	U/Th 4.3 3.2 4.7 3.1 3.4 4.9 3.0 3.2	0.2 0.2 0.1 0.1 0.1 0.3 0.1
Sample ID SSD23LZ047G_56 SSD23LZ047G_34 SSD23LZ047G_7 SSD23LZ047G_60 SSD23LZ047G_28 SSD23LZ047G_20 SSD23LZ047G_9 SSD23LZ047G_51 SSD23LZ047G_51	206/238 Age 216.7 215.9 214.0 213.6 213.0 211.2 210.9 209.9	2σ 14.2 7.0 8.9 8.6 10.2 15.0 8.0 9.0	0.29 0.23 0.25 0.25 0.21 0.26 0.25 0.22	2σ 0.08 0.03 0.05 0.05 0.05 0.07 0.05 0.03	206Pb/238U 0.03 0.03 0.03 0.03 0.03 0.03 0.03 0.03 0.03 0.03	2σ 0.00 0.00 0.00 0.00 0.00 0.00 0.00 0.00	238U/206Pb 29.70 29.02 29.51 29.48 29.44 30.77 30.12 29.65 30.41	26 2.00 0.93 1.41 1.21 1.33 2.53 1.20 1.17	207Pb/206Pb 0.06 0.05 0.05 0.06 0.04 0.05 0.05 0.05 0.05	2σ 0.02 0.01 0.01 0.01 0.01 0.01 0.01	U (ppm) 160.8 601.0 261.8 301.2 237.6 176.2 315.7 336.9 294.2	26 15.9 54.1 20.6 8.8 7.3 7.0 10.5 15.4	Th (ppm) 36.7 195.1 55.3 94.6 68.5 36.4 103.5 104.4 82.6	26 2.6 23.0 4.1 3.1 2.9 3.6 4.8 3.2	Pb (ppm) 3.6 19.6 7.9 9.2 6.9 4.7 10.6 10.9 8.4	2.8 1.3 1.5 1.1 1.4 1.5 1.7	U/Th 4.3 3.2 4.7 3.1 3.4 4.9 3.0 3.2 3.6	0.2 0.2 0.1 0.1 0.1 0.3 0.1 0.1 0.1
Sample ID SSD23LZ047G_56 SSD23LZ047G_34 SSD23LZ047G_7 SSD23LZ047G_60 SSD23LZ047G_28 SSD23LZ047G_20 SSD23LZ047G_9 SSD23LZ047G_51 SSD23LZ047G_5 SSD23LZ047G_5	206/238 Age 216.7 215.9 214.0 213.6 213.0 211.2 210.9 209.9 209.6	2σ 14.2 7.0 8.9 8.6 10.2 15.0 8.0 9.0 8.7	207Pb/235U 0.29 0.23 0.25 0.25 0.21 0.26 0.25 0.22 0.23	2σ 0.08 0.03 0.05 0.05 0.05 0.07 0.05 0.03 0.05	206Pb/238U 0.03 0.03 0.03 0.03 0.03 0.03 0.03 0.03 0.03 0.03	2σ 0.00 0.00 0.00 0.00 0.00 0.00 0.00 0.00	238U/206Pb 29.70 29.02 29.51 29.48 29.44 30.77 30.12 29.65 30.41 30.28	2.00 0.93 1.41 1.21 1.33 2.53 1.20 1.17 1.31	207Pb/206Pb 0.06 0.05 0.05 0.06 0.04 0.05 0.05 0.05 0.05 0.05	2σ 0.02 0.01 0.01 0.01 0.01 0.01 0.01 0.01	U (ppm) 160.8 601.0 261.8 301.2 237.6 176.2 315.7 336.9 294.2 325.7	26 15.9 54.1 20.6 8.8 7.3 7.0 10.5 15.4 16.2	Th (ppm) 36.7 195.1 55.3 94.6 68.5 36.4 103.5 104.4 82.6 104.1	2.6 23.0 4.1 3.1 2.9 3.6 4.8 3.2 4.8	Pb (ppm) 3.6 19.6 7.9 9.2 6.9 4.7 10.6 10.9 8.4 10.2	2σ 0.8 2.8 1.3 1.5 1.1 1.4 1.5 1.4 1.7	U/Th 4.3 3.2 4.7 3.1 3.4 4.9 3.0 3.2 3.6 3.1	2σ 0.2 0.1 0.1 0.3 0.1 0.1 0.1
Sample ID SSD23LZ047G_56 SSD23LZ047G_34 SSD23LZ047G_7 SSD23LZ047G_60 SSD23LZ047G_28 SSD23LZ047G_20 SSD23LZ047G_9 SSD23LZ047G_51 SSD23LZ047G_51 SSD23LZ047G_5 SSD23LZ047G_48 SSD23LZ047G_48	206/238 Age 216.7 215.9 214.0 213.6 213.0 211.2 210.9 209.9	2σ 14.2 7.0 8.9 8.6 10.2 15.0 8.0 9.0	0.29 0.23 0.25 0.25 0.21 0.26 0.25 0.22	2σ 0.08 0.03 0.05 0.05 0.05 0.07 0.05 0.03	206Pb/238U 0.03 0.03 0.03 0.03 0.03 0.03 0.03 0.03 0.03 0.03	2σ 0.00 0.00 0.00 0.00 0.00 0.00 0.00 0.00	238U/206Pb 29.70 29.02 29.51 29.48 29.44 30.77 30.12 29.65 30.41	26 2.00 0.93 1.41 1.21 1.33 2.53 1.20 1.17	207Pb/206Pb 0.06 0.05 0.05 0.06 0.04 0.05 0.05 0.05 0.05	2σ 0.02 0.01 0.01 0.01 0.01 0.01 0.01	U (ppm) 160.8 601.0 261.8 301.2 237.6 176.2 315.7 336.9 294.2	26 15.9 54.1 20.6 8.8 7.3 7.0 10.5 15.4	Th (ppm) 36.7 195.1 55.3 94.6 68.5 36.4 103.5 104.4 82.6	26 2.6 23.0 4.1 3.1 2.9 3.6 4.8 3.2	Pb (ppm) 3.6 19.6 7.9 9.2 6.9 4.7 10.6 10.9 8.4	2.8 1.3 1.5 1.1 1.4 1.5 1.7	U/Th 4.3 3.2 4.7 3.1 3.4 4.9 3.0 3.2 3.6	0.2 0.2 0.1 0.1 0.1 0.3 0.1 0.1 0.1
Sample ID SSD23LZ047G_56 SSD23LZ047G_34 SSD23LZ047G_7 SSD23LZ047G_60 SSD23LZ047G_28 SSD23LZ047G_20 SSD23LZ047G_9 SSD23LZ047G_5 SSD23LZ047G_5 SSD23LZ047G_5 SSD23LZ047G_5	206/238 Age 216.7 215.9 214.0 213.6 213.0 211.2 210.9 209.9 209.6	2σ 14.2 7.0 8.9 8.6 10.2 15.0 8.0 9.0 8.7	207Pb/235U 0.29 0.23 0.25 0.25 0.21 0.26 0.25 0.22 0.23	2σ 0.08 0.03 0.05 0.05 0.05 0.07 0.05 0.03 0.05	206Pb/238U 0.03 0.03 0.03 0.03 0.03 0.03 0.03 0.03 0.03 0.03	2σ 0.00 0.00 0.00 0.00 0.00 0.00 0.00 0.00	238U/206Pb 29.70 29.02 29.51 29.48 29.44 30.77 30.12 29.65 30.41 30.28	2.00 0.93 1.41 1.21 1.33 2.53 1.20 1.17 1.31	207Pb/206Pb 0.06 0.05 0.05 0.06 0.04 0.05 0.05 0.05 0.05 0.05	2σ 0.02 0.01 0.01 0.01 0.01 0.01 0.01 0.01	U (ppm) 160.8 601.0 261.8 301.2 237.6 176.2 315.7 336.9 294.2 325.7	26 15.9 54.1 20.6 8.8 7.3 7.0 10.5 15.4 16.2	Th (ppm) 36.7 195.1 55.3 94.6 68.5 36.4 103.5 104.4 82.6 104.1	2.6 23.0 4.1 3.1 2.9 3.6 4.8 3.2 4.8	Pb (ppm) 3.6 19.6 7.9 9.2 6.9 4.7 10.6 10.9 8.4 10.2	2σ 0.8 2.8 1.3 1.5 1.1 1.4 1.5 1.4 1.7	U/Th 4.3 3.2 4.7 3.1 3.4 4.9 3.0 3.2 3.6 3.1	2σ 0.2 0.1 0.1 0.1 0.3 0.1 0.1 0.1
Sample ID SSD23LZ047G_56 SSD23LZ047G_34 SSD23LZ047G_7 SSD23LZ047G_60 SSD23LZ047G_28 SSD23LZ047G_20 SSD23LZ047G_9 SSD23LZ047G_51 SSD23LZ047G_51 SSD23LZ047G_54 SSD23LZ047G_48 SSD23LZ047G_48	206/238 Age 216.7 215.9 214.0 213.6 213.0 211.2 210.9 209.9 209.6 209.4 209.0	2σ 14.2 7.0 8.9 8.6 10.2 15.0 8.0 9.0 8.7 10.5	207Pb/235U 0.29 0.23 0.25 0.25 0.21 0.26 0.25 0.22 0.23 0.23	2σ 0.08 0.03 0.05 0.05 0.07 0.05 0.03 0.05 0.05	206Pb/238U 0.03 0.03 0.03 0.03 0.03 0.03 0.03 0.03 0.03 0.03 0.03 0.03	2σ 0.00 0.00 0.00 0.00 0.00 0.00 0.00 0.00 0.00 0.00	238U/206Pb 29.70 29.02 29.51 29.48 29.44 30.77 30.12 29.65 30.41 30.28 31.04	26 2.00 0.93 1.41 1.21 1.33 2.53 1.20 1.17 1.31 1.58 2.13	207Pb/206Pb 0.06 0.05 0.05 0.06 0.04 0.05 0.05 0.05 0.05 0.05 0.05	2σ 0.02 0.01 0.01 0.01 0.01 0.01 0.01 0.01 0.01 0.01	U (ppm) 160.8 601.0 261.8 301.2 237.6 176.2 315.7 336.9 294.2 325.7 190.7	26 15.9 54.1 20.6 8.8 7.3 7.0 10.5 15.4 16.2 18.0 9.8	Th (ppm) 36.7 195.1 55.3 94.6 68.5 36.4 103.5 104.4 82.6 104.1 45.3	26 2.6 23.0 4.1 3.1 2.9 3.6 4.8 3.2 4.8 6.4 2.6	Pb (ppm) 3.6 19.6 7.9 9.2 6.9 4.7 10.6 10.9 8.4 10.2 3.5	2σ 0.8 2.8 1.3 1.5 1.1 1.4 1.5 1.4 1.7 1.4 0.9	U/Th 4.3 3.2 4.7 3.1 3.4 4.9 3.0 3.2 3.6 3.1 4.1	2σ 0.2 0.1 0.1 0.1 0.3 0.1 0.1 0.1 0.1

I	İ	ı	İ	l	Ī	ı	İ	i	Ī	ı	I	İ	ı	ı	ı	1	ı	i
SSD23LZ047G_45	208.2	9.6	0.23	0.05	0.03	0.00	30.35	1.40	0.05	0.01	279.5	8.9	67.0	1.5	7.0	1.1	4.1	0.1
SSD23LZ047G_26	206.4	9.3	0.25	0.05	0.03	0.00	30.76	1.46	0.05	0.01	317.0	14.8	76.9	3.4	7.9	1.3	4.0	0.1
SSD23LZ047G_49	206.3	9.3	0.24	0.04	0.03	0.00	30.58	1.38	0.06	0.01	241.4	12.3	55.6	1.8	6.1	0.9	4.3	0.1
SSD23LZ047G_55	205.9	9.1	0.24	0.04	0.03	0.00	30.31	1.35	0.05	0.01	357.2	22.3	56.0	3.0	5.9	1.3	6.3	0.2
SSD23LZ047G_64	205.8	7.9	0.21	0.05	0.03	0.00	30.19	0.99	0.05	0.01	298.5	18.0	87.2	6.3	9.4	1.7	3.4	0.1
SSD23LZ047G_61	205.1	11.4	0.22	0.06	0.03	0.00	31.15	1.86	0.05	0.01	217.1	6.7	56.2	1.7	6.9	1.3	3.8	0.1
SSD23LZ047G_65	204.5	10.7	0.24	0.05	0.03	0.00	31.10	1.56	0.06	0.01	287.5	18.9	95.3	8.6	10.1	1.8	3.0	0.1
SSD23LZ047G_8	203.4	12.7	0.27	0.05	0.03	0.00	32.05	2.21	0.06	0.01	194.0	24.3	45.3	4.9	3.8	1.0	4.2	0.1
SSD23LZ047G_46	203.3	9.6	0.24	0.05	0.03	0.00	30.77	1.44	0.05	0.01	318.1	10.5	104.5	2.7	10.1	1.3	3.0	0.1
SSD23LZ047G_18	203.2	9.5	0.22	0.04	0.03	0.00	31.43	1.62	0.05	0.01	319.5	12.8	99.1	6.0	8.5	1.3	3.2	0.2
SSD23LZ047G_16	203.0	8.2	0.23	0.04	0.03	0.00	31.30	1.35	0.05	0.01	447.0	20.7	182.1	7.6	18.1	2.1	2.4	0.0
SSD23LZ047G_3	201.8	8.2	0.19	0.04	0.03	0.00	31.22	1.23	0.05	0.01	277.6	17.0	69.4	4.3	6.3	1.0	4.0	0.1
SSD23LZ047G_53	200.9	8.9	0.21	0.04	0.03	0.00	31.44	1.48	0.05	0.01	336.2	16.0	95.4	3.7	9.1	1.2	3.5	0.1
SSD23LZ047G_52	200.8	13.2	0.23	0.04	0.03	0.00	31.88	2.07	0.05	0.01	251.8	18.9	90.8	7.2	9.3	1.5	2.8	0.1
SSD23LZ047G_57	199.6	9.0	0.24	0.05	0.03	0.00	31.65	1.47	0.06	0.01	281.0	9.5	71.2	2.4	7.5	1.4	3.9	0.1
SSD23LZ047G_15	198.2	9.9	0.26	0.06	0.03	0.00	32.31	1.65	0.05	0.01	319.8	10.5	79.1	2.5	7.5	1.4	4.0	0.1
SSD23LZ047G_41	197.5	7.9	0.23	0.03	0.03	0.00	31.63	1.47	0.05	0.01	413.6	19.7	154.1	5.5	13.5	1.7	2.7	0.1
Sample ID	206/238 Age	2σ	207Pb/235U	2σ	206Pb/238U	2σ	238U/206Pb	2σ	207Pb/206Pb	2σ	U (ppm)	2σ	Th (ppm)	2σ	Pb (ppm)	2σ	U/Th	2σ
SSD23LZ049GR_63	217.1	10.6	0.23	0.04	0.03	0.00	29.43	1.51	0.05	0.01	344.9	13.4	158.0	6.6	16.6	1.5	2.1	0.0
SSD23LZ049GR_2	216.6	8.2	0.24	0.05	0.03	0.00	28.79	0.99	0.05	0.01	311.5	7.6	100.8	2.7	10.8	1.3	3.0	0.1
SSD23LZ049GR_35	215.9	9.7	0.24	0.03	0.03	0.00	29.51	1.45	0.05	0.01	500.9	12.6	259.3	7.1	24.3	1.9	1.9	0.0
SSD23LZ049GR_42	215.2	15.0	0.20	0.08	0.03	0.00	29.54	1.96	0.04	0.02	274.2	23.1	64.9	7.0	5.7	1.6	4.3	0.2
SSD23LZ049GR_31	214.5	15.1	0.20	0.07	0.03	0.00	29.93	2.43	0.04	0.01	228.8	20.2	60.3	5.0	6.3	1.1	3.8	0.1
SSD23LZ049GR_30	214.4	10.2	0.20	0.05	0.03	0.00	29.74	1.42	0.05	0.01	170.4	6.3	47.3	2.6	4.8	0.9	3.7	0.2
SSD23LZ049GR_37	214.0	10.4	0.24	0.06	0.03	0.00	29.83	1.53	0.05	0.01	206.7	9.8	57.6	3.6	4.9	0.9	3.6	0.1
SSD23LZ049GR_14	213.1	8.0	0.24	0.03	0.03	0.00	29.33	0.97	0.05	0.01	672.0	35.7	234.4	11.6	25.2	2.2	2.8	0.0
SSD23LZ049GR_25	213.1	8.2	0.21	0.05	0.03	0.00	29.70	1.12	0.05	0.01	341.6	31.4	94.6	10.0	9.0	1.7	3.6	0.1
SSD23LZ049GR_41	212.2	11.7	0.26	0.07	0.03	0.00	30.02	1.75	0.05	0.01	227.5	12.7	54.9	3.3	4.3	0.8	4.1	0.1
SSD23LZ049GR_49	212.1	12.3	0.21	0.05	0.03	0.00	30.39	1.84	0.04	0.01	177.5	10.8	42.9	3.1	4.3	1.0	4.2	0.2
SSD23LZ049GR_46	211.6	18.3	0.21	0.08	0.03	0.00	31.58	2.82	0.04	0.01	101.6	3.5	22.9	1.0	2.0	0.6	4.5	0.2

		l			-	1	-	1								I		I
SSD23LZ049GR_4	210.7	10.9	0.22	0.05	0.03	0.00	30.27	1.60	0.05	0.01	266.0	15.9	71.2	3.1	7.1	1.2	3.6	0.2
SSD23LZ049GR_9	210.6	9.9	0.22	0.05	0.03	0.00	30.20	1.48	0.05	0.01	267.0	8.0	66.7	1.9	6.7	1.0	3.9	0.1
SSD23LZ049GR_28	210.3	5.5	0.23	0.04	0.03	0.00	29.70	0.86	0.05	0.01	434.3	23.8	152.7	6.8	15.6	2.0	2.8	0.1
SSD23LZ049GR_8	210.3	9.3	0.25	0.04	0.03	0.00	30.15	1.34	0.05	0.01	237.7	13.0	86.1	5.3	6.7	1.1	2.7	0.1
SSD23LZ049GR_58	210.2	11.5	0.21	0.05	0.03	0.00	30.57	1.72	0.04	0.01	242.7	4.9	54.6	1.8	5.2	0.8	4.5	0.1
SSD23LZ049GR_61	209.5	6.9	0.21	0.04	0.03	0.00	30.15	1.02	0.05	0.01	438.3	12.8	140.5	9.1	13.5	1.9	3.2	0.2
SSD23LZ049GR_23	208.6	13.5	0.26	0.06	0.03	0.00	31.26	2.27	0.06	0.01	179.1	3.5	49.9	2.4	6.3	1.3	3.6	0.1
SSD23LZ049GR_56C	208.1	10.8	0.23	0.05	0.03	0.00	30.44	1.54	0.05	0.01	398.4	18.3	90.3	3.9	7.4	1.7	4.4	0.1
SSD23LZ049GR_38	208.0	6.1	0.24	0.03	0.03	0.00	30.27	0.89	0.05	0.01	351.1	20.1	104.0	7.6	8.8	1.1	3.4	0.1
SSD23LZ049GR_29	207.4	8.7	0.24	0.05	0.03	0.00	30.62	1.29	0.06	0.01	289.5	21.7	119.1	12.3	11.5	2.2	2.5	0.1
SSD23LZ049GR_15	207.3	7.8	0.24	0.04	0.03	0.00	30.50	1.13	0.06	0.01	499.5	31.8	154.9	11.9	15.2	2.4	3.2	0.1
SSD23LZ049GR_1	207.1	4.9	0.22	0.03	0.03	0.00	30.01	0.83	0.05	0.01	699.4	55.5	217.6	20.8	20.7	2.4	3.1	0.1
SSD23LZ049GR_3	206.3	8.8	0.25	0.05	0.03	0.00	30.66	1.27	0.05	0.01	292.8	21.1	115.7	10.6	10.5	1.7	2.5	0.1
SSD23LZ049GR_45	206.2	8.8	0.25	0.05	0.03	0.00	30.47	1.23	0.05	0.01	480.3	20.0	161.4	9.8	13.8	1.6	3.0	0.1
SSD23LZ049GR_60	204.7	13.5	0.22	0.08	0.03	0.00	31.17	1.95	0.05	0.02	240.2	12.8	61.7	3.2	5.7	1.6	3.8	0.1
SSD23LZ049GR_17	204.6	13.2	0.27	0.05	0.03	0.00	31.15	1.93	0.06	0.01	179.0	10.7	41.6	3.3	3.8	0.9	4.3	0.1
SSD23LZ049GR_48	204.6	12.0	0.24	0.06	0.03	0.00	30.90	1.86	0.05	0.01	446.3	26.4	177.5	9.8	13.8	3.5	2.5	0.1
SSD23LZ049GR_6	203.1	7.6	0.23	0.04	0.03	0.00	30.73	1.21	0.05	0.01	345.6	9.5	66.4	2.0	5.0	0.9	5.0	0.2
SSD23LZ049GR_55	203.0	10.5	0.22	0.05	0.03	0.00	31.57	1.74	0.05	0.01	196.0	9.3	39.1	2.0	3.1	0.9	5.0	0.1
SSD23LZ049GR_10	202.7	11.6	0.22	0.06	0.03	0.00	31.76	1.94	0.05	0.01	221.4	13.5	52.6	2.8	5.7	1.1	4.0	0.1
SSD23LZ049GR_43	200.7	13.0	0.24	0.06	0.03	0.00	32.43	2.25	0.06	0.01	201.7	14.6	58.0	3.2	4.9	1.4	3.5	0.1
Sample ID	206/238 Age	2σ	207Pb/235U	2σ	206Pb/238U	2σ	238U/206Pb	2σ	207Pb/206Pb	2σ	U (ppm)	2σ	Th (ppm)	2σ	Pb (ppm)	2σ	U/Th	2σ
SSD23LZ050GR 3	215.7	10.4	0.27	0.07	0.03	0.00	29.61	1.46	0.06	0.02	228.1	12.7	78.4	3.8	7.2	1.1	2.8	0.1
SSD23LZ050GR_58	215.4	10.5	0.24	0.06	0.03	0.00	29.82	1.47	0.05	0.01	307.9	23.1	109.2	8.8	11.9	1.8	2.9	0.1
SSD23LZ050GR 67	215.1	11.5	0.21	0.05	0.03	0.00	29.90	1.50	0.05	0.01	325.9	22.7	123.8	5.6	12.5	1.4	2.6	0.1
SSD23LZ050GR 20	214.6	13.4	0.25	0.07	0.03	0.00	30.31	2.00	0.06	0.01	184.5	15.4	74.5	7.9	8.1	1.3	2.6	0.1
SSD23LZ050GR_50	213.6	16.6	0.27	0.09	0.03	0.00	30.03	2.48	0.05	0.02	220.9	11.2	67.8	3.5	5.5	2.1	3.3	0.1
SSD23LZ050GR 16	213.5	12.3	0.22	0.04	0.03	0.00	30.04	1.68	0.05	0.01	349.9	24.3	110.4	8.1	11.8	2.0	3.3	0.1
SSD23LZ050GR 17	212.8	9.3	0.22	0.05	0.03	0.00	29.59	1.26	0.05	0.01	261.9	16.4	73.4	4.4	8.0	1.5	3.7	0.1
SSD23LZ050GR 1	210.8	12.0	0.24	0.05	0.03	0.00	30.38	1.90	0.05	0.01	256.5	11.9	87.3	4.7	7.7	1.3	2.9	0.1

SSD23LZ050GR 42	210.4	11.0	0.23	0.05	0.03	0.00	30.63	1.61	0.05	0.01	252.1	11.7	76.8	3.3	7.5	1.4	3.2	0.1
SSD23LZ050GR 18	210.4	11.9	0.27	0.05	0.03	0.00	30.09	1.58	0.06	0.01	230.7	17.0	77.4	6.5	9.4	1.5	3.1	0.1
SSD23LZ050GR 8	210.1	12.1	0.27	0.07	0.03	0.00	30.20	1.60	0.06	0.01	181.2	17.7	66.4	6.3	7.0	1.3	2.7	0.1
SSD23LZ050GR_38	210.0	8.8	0.22	0.05	0.03	0.00	30.46	1.41	0.04	0.01	304.9	6.2	98.1	2.5	8.8	1.4	3.0	0.0
SSD23LZ050GR 35	209.5	10.4	0.20	0.06	0.03	0.00	30.69	1.56	0.04	0.01	226.5	13.5	72.5	4.4	6.9	1.3	3.1	0.1
SSD23LZ050GR_60	209.4	19.2	0.23	0.09	0.03	0.00	30.85	3.00	0.05	0.02	379.1	13.6	158.2	9.1	14.4	3.4	2.4	0.1
SSD23LZ050GR_22	209.3	11.4	0.21	0.03	0.03	0.00	30.79	1.68	0.05	0.01	234.4	8.9	81.9	2.6	9.8	1.4	2.9	0.1
SSD23LZ050GR_72	209.2	9.1	0.22	0.05	0.03	0.00	30.53	1.33	0.05	0.01	319.7	16.8	111.3	7.4	9.5	1.3	2.9	0.1
SSD23LZ050GR_47	208.7	11.5	0.24	0.06	0.03	0.00	31.08	1.94	0.05	0.01	265.4	17.8	93.4	5.6	9.3	1.5	2.8	0.1
SSD23LZ050GR_32	207.6	8.5	0.20	0.04	0.03	0.00	30.74	1.27	0.04	0.01	240.8	7.5	76.1	3.5	7.3	1.2	3.1	0.1
SSD23LZ050GR_59	206.9	9.1	0.25	0.06	0.03	0.00	30.22	1.37	0.06	0.02	300.2	19.2	112.5	9.6	11.2	1.7	2.8	0.1
SSD23LZ050GR_36	206.5	11.3	0.27	0.06	0.03	0.00	30.96	1.94	0.06	0.01	179.4	14.6	53.0	5.4	5.8	1.1	3.4	0.1
SSD23LZ050GR_55	205.7	9.9	0.20	0.04	0.03	0.00	30.86	1.42	0.04	0.01	288.4	11.0	90.6	2.9	9.5	1.3	3.2	0.1
SSD23LZ050GR_63	205.6	12.0	0.20	0.04	0.03	0.00	31.16	1.97	0.04	0.01	429.9	9.8	160.1	4.8	11.7	2.6	2.7	0.1
SSD23LZ050GR_10	205.6	9.3	0.23	0.06	0.03	0.00	30.92	1.50	0.05	0.01	298.4	12.7	84.8	2.8	9.4	1.7	3.5	0.1
SSD23LZ050GR_61	205.4	18.8	0.25	0.10	0.03	0.00	31.56	3.40	0.05	0.02	289.5	12.1	91.8	4.2	7.8	2.0	3.2	0.1
SSD23LZ050GR_27	205.4	9.4	0.23	0.05	0.03	0.00	31.20	1.49	0.05	0.01	221.0	9.0	75.2	2.2	6.9	0.9	3.0	0.1
SSD23LZ050GR_48	205.0	11.9	0.26	0.06	0.03	0.00	31.67	1.93	0.06	0.01	209.9	4.2	68.9	2.2	6.9	1.1	3.1	0.1
SSD23LZ050GR_19	204.6	12.4	0.23	0.06	0.03	0.00	31.68	1.96	0.05	0.01	187.3	11.2	59.5	4.0	6.6	1.2	3.3	0.1
SSD23LZ050GR_46	204.2	7.4	0.24	0.03	0.03	0.00	31.22	1.21	0.05	0.01	548.6	15.4	264.5	5.8	24.7	1.9	2.1	0.0
SSD23LZ050GR_28	204.0	11.8	0.20	0.05	0.03	0.00	31.14	1.59	0.05	0.01	236.1	10.7	68.6	2.7	6.3	1.3	3.5	0.1
SSD23LZ050GR_70	203.6	11.3	0.22	0.05	0.03	0.00	31.64	1.64	0.05	0.01	206.5	16.6	64.1	5.7	7.3	1.3	3.3	0.1
SSD23LZ050GR_65	203.4	9.7	0.25	0.08	0.03	0.00	31.30	1.50	0.06	0.02	364.9	20.3	140.2	8.8	13.5	2.6	2.7	0.1
SSD23LZ050GR_44	203.1	7.9	0.24	0.04	0.03	0.00	31.41	1.20	0.05	0.01	391.8	19.1	154.0	8.3	14.2	1.6	2.5	0.1
SSD23LZ050GR_54	202.9	12.2	0.22	0.05	0.03	0.00	31.87	2.37	0.04	0.01	246.0	8.3	72.2	2.9	7.4	1.1	3.5	0.1
SSD23LZ050GR_7	202.9	8.0	0.22	0.05	0.03	0.00	31.31	1.26	0.05	0.01	281.0	20.7	93.7	8.0	7.9	1.4	3.0	0.1
SSD23LZ050GR_64	202.7	10.4	0.22	0.05	0.03	0.00	31.78	1.65	0.05	0.01	224.1	13.0	72.9	5.1	6.9	1.2	3.2	0.1
SSD23LZ050GR_14	200.6	11.5	0.20	0.04	0.03	0.00	31.57	1.66	0.05	0.01	240.7	16.7	70.5	5.4	6.7	1.1	3.5	0.2
SSD23LZ050GR_2	200.0	9.7	0.20	0.06	0.03	0.00	31.67	1.60	0.04	0.01	412.0	11.4	159.6	3.6	13.1	2.0	2.5	0.0
SSD23LZ050GR_49	198.3	8.7	0.21	0.04	0.03	0.00	32.36	1.55	0.05	0.01	403.0	22.2	151.0	9.4	12.8	1.7	2.7	0.1

Sample ID	206/238 Age	2σ	207Pb/235U	2σ	206Pb/238U	2σ	238U/206Pb	2σ	207Pb/206Pb	2σ	U (ppm)	2σ	Th (ppm)	2σ	Pb (ppm)	2σ	U/Th	2σ
SSD23LZ060GR_53	214.8	11.1	0.22	0.03	0.03	0.00	29.15	1.47	0.05	0.01	434.9	43.8	174.7	18.9	15.9	2.7	2.5	0.0
SSD23LZ060GR_54	214.7	17.0	0.20	0.04	0.03	0.00	29.54	2.74	0.04	0.01	464.1	14.9	227.7	5.6	20.0	2.9	2.1	0.1
SSD23LZ060GR_37	213.8	18.0	0.23	0.07	0.03	0.00	29.78	2.41	0.05	0.02	368.2	17.1	98.9	5.1	10.0	3.1	3.7	0.1
SSD23LZ060GR_29	213.5	9.4	0.24	0.04	0.03	0.00	29.67	1.29	0.05	0.01	420.0	54.5	162.6	28.6	16.6	3.5	2.7	0.2
SSD23LZ060GR_1	209.6	8.3	0.23	0.03	0.03	0.00	30.38	1.20	0.06	0.01	601.6	41.5	186.9	14.2	19.5	2.3	3.2	0.1
SSD23LZ060GR_36	209.0	10.0	0.20	0.05	0.03	0.00	30.42	1.58	0.04	0.01	237.2	13.1	99.1	7.7	9.7	1.6	2.4	0.1
SSD23LZ060GR_24	208.9	11.6	0.21	0.07	0.03	0.00	30.21	1.74	0.05	0.02	319.7	15.2	81.7	3.4	9.1	1.8	3.9	0.1
SSD23LZ060GR_26	208.7	11.4	0.21	0.04	0.03	0.00	30.72	1.79	0.05	0.01	321.5	19.2	98.2	7.4	9.3	1.4	3.3	0.1
SSD23LZ060GR_21	208.5	8.9	0.24	0.05	0.03	0.00	30.44	1.30	0.05	0.01	294.1	7.3	77.8	1.9	7.0	1.1	3.9	0.1
SSD23LZ060GR_40	208.0	8.1	0.23	0.05	0.03	0.00	30.31	1.21	0.05	0.01	446.2	29.7	63.6	6.8	6.7	1.4	7.4	0.4
SSD23LZ060GR_18	207.7	15.4	0.21	0.05	0.03	0.00	30.78	2.54	0.05	0.01	430.0	12.1	147.6	3.8	14.1	2.8	3.0	0.1
SSD23LZ060GR_45	207.3	8.3	0.25	0.04	0.03	0.00	30.36	1.22	0.05	0.01	516.1	35.7	286.8	22.5	25.1	2.8	1.9	0.0
SSD23LZ060GR_27	207.1	13.2	0.26	0.06	0.03	0.00	30.66	1.86	0.06	0.01	243.2	28.3	70.4	9.2	5.9	1.6	3.5	0.1
SSD23LZ060GR_47	206.7	8.8	0.22	0.04	0.03	0.00	30.57	1.51	0.05	0.01	357.6	5.4	125.9	4.4	11.9	2.2	2.9	0.1
SSD23LZ060GR_19	206.7	12.6	0.22	0.05	0.03	0.00	30.78	1.85	0.05	0.01	326.5	21.7	98.4	5.4	7.3	1.4	3.4	0.1
SSD23LZ060GR_49	206.6	12.0	0.21	0.04	0.03	0.00	30.40	1.63	0.05	0.01	208.0	11.9	48.3	2.6	4.2	0.9	4.4	0.1
SSD23LZ060GR_61	206.3	10.4	0.24	0.04	0.03	0.00	30.82	1.84	0.05	0.01	388.7	14.4	88.5	3.4	10.5	1.7	4.4	0.1
SSD23LZ060GR_42	206.1	10.9	0.22	0.05	0.03	0.00	30.97	1.80	0.05	0.01	250.9	10.3	62.1	3.5	6.1	1.2	4.1	0.1
SSD23LZ060GR_7	205.3	8.3	0.23	0.05	0.03	0.00	31.02	1.29	0.06	0.01	399.7	20.4	121.4	10.0	11.1	2.0	3.4	0.1
SSD23LZ060GR_51	205.0	8.1	0.25	0.07	0.03	0.00	30.41	1.24	0.05	0.01	423.8	16.8	155.8	9.1	13.3	2.8	2.8	0.1
SSD23LZ060GR_6	205.0	9.3	0.23	0.05	0.03	0.00	31.21	1.50	0.06	0.01	332.4	16.5	83.4	3.7	7.1	1.1	4.0	0.1
SSD23LZ060GR_30	204.0	9.1	0.18	0.04	0.03	0.00	30.66	1.23	0.04	0.01	376.2	60.9	113.9	20.8	10.7	2.4	3.4	0.1
SSD23LZ060GR_62	203.8	5.8	0.21	0.05	0.03	0.00	30.59	0.88	0.05	0.01	463.5	16.2	146.3	5.6	15.6	2.0	3.2	0.0
SSD23LZ060GR_52	203.8	5.6	0.23	0.02	0.03	0.00	30.65	0.88	0.05	0.01	875.6	40.7	259.7	10.1	25.3	3.2	3.4	0.1
SSD23LZ060GR_48	203.2	7.1	0.25	0.03	0.03	0.00	30.58	1.02	0.06	0.01	495.7	34.8	187.9	16.0	16.0	1.4	2.7	0.1
SSD23LZ060GR_25	203.2	19.6	0.31	0.13	0.03	0.00	31.26	3.20	0.07	0.03	138.4	7.3	36.8	2.7	3.0	1.8	3.8	0.2
SSD23LZ060GR_34	202.9	12.6	0.19	0.05	0.03	0.00	31.85	2.18	0.05	0.01	222.1	13.6	72.5	4.9	6.1	1.1	3.0	0.0
SSD23LZ060GR_43	202.3	8.5	0.22	0.03	0.03	0.00	30.86	1.13	0.05	0.01	320.3	13.5	103.5	5.7	8.9	1.4	3.2	0.1
SSD23LZ060GR_17	202.0	16.9	0.25	0.06	0.03	0.00	31.67	2.99	0.06	0.02	556.7	34.4	205.1	11.0	18.2	3.1	2.8	0.1

														1				I
SSD23LZ060GR_23	201.9	12.3	0.22	0.07	0.03	0.00	31.58	2.06	0.05	0.02	284.2	19.2	79.7	4.6	8.2	2.0	3.6	0.1
SSD23LZ060GR_41	200.6	9.6	0.20	0.04	0.03	0.00	31.63	1.52	0.05	0.01	432.7	16.2	187.5	6.2	16.0	1.6	2.3	0.1
SSD23LZ060GR_13	199.7	7.5	0.24	0.05	0.03	0.00	31.79	1.25	0.06	0.01	349.6	21.7	127.8	8.2	11.1	1.6	2.8	0.1
SSD23LZ060GR_16	199.1	19.5	0.26	0.09	0.03	0.00	32.29	3.43	0.06	0.02	310.4	33.4	104.0	10.3	9.1	2.2	3.0	0.1
SSD23LZ060GR_28	198.8	9.9	0.22	0.05	0.03	0.00	31.73	1.60	0.05	0.01	221.5	23.0	58.9	7.0	5.3	1.2	3.9	0.1
SSD23LZ060GR_3	198.8	8.2	0.23	0.04	0.03	0.00	32.05	1.23	0.06	0.01	545.1	17.3	248.6	20.9	23.5	3.1	2.3	0.2
Sample ID	206/238 Age	2σ	207Pb/235U	2σ	206Pb/238U	2σ	238U/206Pb	2σ	207Pb/206Pb	2σ	U (ppm)	2σ	Th (ppm)	2σ	Pb (ppm)	2σ	U/Th	2σ
SSD23LZ079GR_43	212.6	12.7	0.21	0.05	0.03	0.00	29.87	1.73	0.04	0.01	138.5	9.8	26.7	2.2	2.5	0.6	5.4	0.2
SSD23LZ079GR_45	212.2	11.1	0.30	0.06	0.03	0.00	29.74	1.61	0.06	0.01	289.8	18.8	79.9	8.6	11.0	2.0	3.9	0.2
SSD23LZ079GR_16	212.0	17.0	0.21	0.05	0.03	0.00	30.24	2.49	0.04	0.01	140.6	13.8	30.9	3.4	3.1	1.1	4.6	0.2
SSD23LZ079GR_55	211.4	16.6	0.30	0.09	0.03	0.00	30.91	2.63	0.06	0.02	173.6	13.2	37.6	2.6	3.7	0.8	4.5	0.2
SSD23LZ079GR 13	210.5	17.6	0.25	0.10	0.03	0.00	30.09	2.90	0.05	0.02	166.0	8.4	32.6	2.1	3.3	1.5	5.2	0.3
SSD23LZ079GR 6	210.4	8.2	0.21	0.03	0.03	0.00	29.74	1.17	0.05	0.01	616.8	29.2	234.3	11.3	25.2	2.9	2.6	0.0
SSD23LZ079GR 37	210.0	13.3	0.28	0.07	0.03	0.00	30.35	1.83	0.06	0.01	212.7	15.6	68.6	5.7	7.2	1.3	3.3	0.1
SSD23LZ079GR 21	209.5	14.9	0.21	0.04	0.03	0.00	30.35	2.03	0.05	0.01	269.0	20.8	66.9	6.8	4.8	0.9	4.1	0.2
SSD23LZ079GR 2	208.8	10.1	0.22	0.04	0.03	0.00	30.24	1.52	0.05	0.01	385.1	27.5	86.9	8.1	11.2	2.2	4.5	0.1
SSD23LZ079GR 47	207.4	15.3	0.23	0.06	0.03	0.00	30.60	2.30	0.05	0.01	149.2	4.6	35.5	1.2	4.1	1.0	4.3	0.1
SSD23LZ079GR 38	207.1	10.5	0.21	0.06	0.03	0.00	30.47	1.66	0.05	0.01	189.1	13.0	64.1	5.1	7.0	1.1	3.0	0.1
		7.6		0.04							582.5	29.0			19.2	2.3	3.0	
SSD23LZ079GR_42	206.9		0.25		0.03	0.00	30.07	1.15	0.05	0.01			198.0	10.7	-			0.1
SSD23LZ079GR_46	206.8	9.9	0.27	0.05	0.03	0.00	30.45	1.59	0.05	0.01	400.7	10.5	95.8	3.6	10.2	1.8	4.3	0.1
SSD23LZ079GR_59	206.3	9.6	0.25	0.04	0.03	0.00	30.02	1.25	0.06	0.01	294.7	20.8	82.2	6.9	9.1	1.6	3.6	0.1
SSD23LZ079GR_18	206.0	9.5	0.21	0.03	0.03	0.00	30.12	1.31	0.05	0.01	499.7	27.0	137.5	6.8	10.4	1.3	3.6	0.1
SSD23LZ079GR_58	205.0	10.1	0.27	0.04	0.03	0.00	30.75	1.57	0.06	0.01	335.4	20.2	106.5	6.9	9.5	1.4	3.1	0.1
SSD23LZ079GR_57	204.7	12.7	0.22	0.06	0.03	0.00	30.67	1.73	0.05	0.02	193.8	15.8	43.7	4.5	4.7	1.0	4.4	0.1
SSD23LZ079GR_40	204.5	9.6	0.22	0.03	0.03	0.00	30.69	1.42	0.05	0.01	462.4	21.3	199.9	10.1	19.4	2.5	2.4	0.0
SSD23LZ079GR_54	204.5	10.5	0.25	0.06	0.03	0.00	30.45	1.43	0.05	0.01	241.4	10.2	75.5	3.5	8.0	1.4	3.1	0.1
SSD23LZ079GR_20	204.3	9.9	0.20	0.04	0.03	0.00	30.82	1.53	0.04	0.01	265.5	19.0	74.5	3.9	6.7	1.3	3.5	0.1
SSD23LZ079GR_56	204.3	10.2	0.26	0.07	0.03	0.00	30.87	1.56	0.06	0.01	329.9	24.2	108.0	5.5	11.7	1.7	3.0	0.2
SSD23LZ079GR_32	204.2	8.4	0.22	0.04	0.03	0.00	29.89	1.34	0.05	0.01	273.4	26.2	70.4	6.9	8.2	1.5	3.9	0.1
SSD23LZ079GR_26	203.6	7.5	0.23	0.03	0.03	0.00	30.66	1.19	0.05	0.01	443.4	29.2	152.7	9.9	13.0	1.5	2.8	0.1

		1				İ	Ī	1	·	1		1		I	ĺ		I	1
SSD23LZ079GR_41	203.1	10.9	0.19	0.06	0.03	0.00	30.65	1.47	0.04	0.01	230.2	24.0	93.9	12.6	9.1	2.0	2.6	0.1
SSD23LZ079GR_10	203.0	18.6	0.24	0.08	0.03	0.00	31.00	2.81	0.05	0.02	335.3	12.1	119.8	5.8	11.8	3.0	2.8	0.1
SSD23LZ079GR_27	201.6	11.5	0.23	0.05	0.03	0.00	31.47	1.78	0.05	0.01	382.2	28.3	100.4	9.2	9.2	1.3	3.8	0.1
SSD23LZ079GR_50	200.5	11.6	0.23	0.07	0.03	0.00	31.22	1.93	0.05	0.01	305.7	9.1	63.9	3.1	5.1	1.6	4.8	0.2
SSD23LZ079GR_29	200.5	10.9	0.20	0.06	0.03	0.00	31.63	1.82	0.05	0.01	218.7	5.1	42.7	2.0	3.5	0.9	5.1	0.2
SSD23LZ079GR_61	197.5	13.4	0.24	0.08	0.03	0.00	32.00	2.46	0.06	0.02	269.4	12.2	62.7	2.4	6.2	1.5	4.3	0.2
Sample ID	206/238 Age	2σ	207Pb/235U	2σ	206Pb/238U	2σ	238U/206Pb	2σ	207Pb/206Pb	2σ	U (ppm)	2σ	Th (ppm)	2σ	Pb (ppm)	2σ	U/Th	2σ
SSD23LZ095GR 15	213.4	20.3	0.20	0.08	0.03	0.00	29.79	2.82	0.05	0.02	441.6	34.0	91.2	10.4	9.0	2.4	4.9	0.2
_																		
SSD23LZ095GR_31	212.7	9.3	0.20	0.04	0.03	0.00	29.63	1.38	0.05	0.01	250.9	9.1	76.7	2.9	8.3	1.1	3.2	0.1
SSD23LZ095GR_42	212.3	8.7	0.23	0.05	0.03	0.00	29.71	1.25	0.05	0.01	298.9	16.7	88.2	4.3	10.4	1.7	3.4	0.1
SSD23LZ095GR_45	212.2	14.3	0.26	0.08	0.03	0.00	30.55	2.20	0.05	0.01	173.7	9.5	52.1	3.3	6.5	1.3	3.4	0.1
SSD23LZ095GR_5	211.9	10.7	0.27	0.05	0.03	0.00	29.86	1.70	0.07	0.01	285.7	13.8	73.7	4.5	8.0	1.3	4.0	0.1
SSD23LZ095GR_43	211.5	11.4	0.30	0.07	0.03	0.00	29.71	1.49	0.07	0.01	191.3	9.5	60.4	3.7	5.9	1.1	3.3	0.1
SSD23LZ095GR_34	210.2	15.5	0.31	0.09	0.03	0.00	29.88	2.00	0.07	0.02	275.9	10.0	64.6	3.0	10.3	4.1	4.2	0.2
SSD23LZ095GR_20	210.1	12.4	0.24	0.06	0.03	0.00	30.48	2.06	0.06	0.02	224.3	13.2	58.0	3.7	6.0	1.3	3.8	0.1
SSD23LZ095GR_26	209.6	11.3	0.23	0.05	0.03	0.00	30.39	1.83	0.06	0.01	296.1	6.6	85.9	3.0	8.6	1.2	3.4	0.1
SSD23LZ095GR_27	209.6	11.7	0.23	0.06	0.03	0.00	29.97	1.60	0.06	0.02	342.9	7.0	119.5	4.4	10.9	2.1	2.8	0.1
SSD23LZ095GR_37	209.5	15.1	0.23	0.08	0.03	0.00	30.16	2.65	0.05	0.02	337.9	42.6	67.4	11.1	7.7	2.5	5.0	0.3
SSD23LZ095GR_35	209.5	20.5	0.23	0.08	0.03	0.00	30.76	2.94	0.06	0.02	245.2	27.4	54.1	6.5	7.2	2.3	4.4	0.2
SSD23LZ095GR 46	209.2	8.7	0.23	0.05	0.03	0.00	30.17	1.25	0.05	0.01	256.6	13.1	72.9	3.9	6.3	1.2	3.6	0.1
SSD23LZ095GR 3	208.7	8.4	0.23	0.04	0.03	0.00	30.00	1.23	0.05	0.01	381.5	12.5	120.8	4.8	12.1	1.7	3.2	0.1
SSD23LZ095GR 52	208.7	7.5	0.25	0.03	0.03	0.00	30.19	1.13	0.05	0.01	531.4	17.6	180.8	5.6	15.6	1.6	3.0	0.1
SSD23LZ095GR 30	208.5	13.5	0.23	0.06	0.03	0.00	30.82	2.02	0.06	0.02	200.6	14.7	44.1	3.8	4.5	1.1	4.4	0.1
_																		
SSD23LZ095GR_28	208.4	12.7	0.20	0.06	0.03	0.00	30.72	1.88	0.05	0.02	209.1	11.4	62.6	1.7	6.6	1.1	3.2	0.1
SSD23LZ095GR_53	208.3	9.9	0.26	0.07	0.03	0.00	30.24	1.61	0.06	0.02	300.7	10.1	70.2	2.2	6.8	1.7	4.4	0.1
SSD23LZ095GR_39	208.3	12.7	0.24	0.06	0.03	0.00	30.28	1.86	0.06	0.01	249.5	6.2	57.5	3.1	7.9	2.2	4.3	0.2
SSD23LZ095GR_18	207.5	13.8	0.20	0.06	0.03	0.00	30.99	2.08	0.05	0.01	176.8	16.9	52.2	6.8	6.1	1.3	3.5	0.2
SSD23LZ095GR_4	207.0	9.1	0.23	0.04	0.03	0.00	30.36	1.40	0.06	0.01	325.3	15.2	89.9	3.2	10.2	1.5	3.7	0.1
SSD23LZ095GR_32	206.8	9.8	0.22	0.05	0.03	0.00	30.34	1.55	0.05	0.01	400.4	17.5	122.4	7.0	13.2	2.6	3.2	0.1
SSD23LZ095GR_16	206.5	14.7	0.21	0.09	0.03	0.00	30.66	2.46	0.05	0.02	204.9	28.0	49.4	8.9	4.9	1.4	4.2	0.3

SSD23LZ095GR_50	61.2 6.4	6.4 6.2	1.2	4.1	
			1	4.1	0.1
SSD23/7095GR 60 203.7 7.4 0.19 0.03 0.03 0.00 31.01 1.17 0.04 0.01 507.6 12.9 1	100.3 6.4	6.4 10.1	1.3	6.1	0.1
5552525561_00 2501 711 012 0100 0100 0100 1111 0101 0101	171.6 6.4	6.4 16.5	2.1	3.0	0.1
SSD23LZ095GR_57 202.3 12.6 0.24 0.06 0.03 0.00 30.86 1.71 0.05 0.01 250.9 13.4 6	69.7 3.3	3.3 6.6	1.4	3.7	0.1
SSD23LZ095GR_63	98.1 4.0	4.0 9.5	1.7	3.5	0.1
SSD23LZ095GR_2 201.5 8.0 0.22 0.04 0.03 0.00 30.72 1.12 0.05 0.01 431.9 14.0 6	69.6 4.5	4.5 7.9	1.5	6.3	0.2
SSD23LZ095GR_6 200.9 14.1 0.26 0.09 0.03 0.00 31.30 2.29 0.06 0.02 510.1 18.2 1	110.8 3.7	3.7 12.8	3.0	4.7	0.1
SSD23LZ095GR_24	37.4 4.6	4.6 4.7	1.2	4.1	0.3
SSD23LZ095GR_38	30.9 2.1	2.1 4.1	1.8	5.4	0.3
SSD23LZ095GR 41 197.5 25.6 0.16 0.07 0.03 0.00 32.94 4.73 0.04 0.02 240.5 9.5 5	51.7 1.8	1.8 6.6	1.6	4.7	0.2
	179.0 9.0		5.1	3.0	0.1
Sample ID 206/238 Age 2σ 207Pb/235U 2σ 206Pb/238U 2σ 238U/206Pb 2σ 207Pb/206Pb 2σ U (ppm) 2σ Τ	Th (ppm) 2σ	2σ Pb (ppm)	2σ	U/Th	2σ
SSD23LZ101GR_25 211.2 16.5 0.27 0.07 0.03 0.00 30.56 2.24 0.06 0.02 153.9 6.0 3	38.9 3.0	3.0 3.6	1.0	3.9	0.2
SSD23LZ101GR_63	107.2 7.6	7.6 9.8	1.5	3.7	0.1
SSD23LZ101GR_23 209.5 11.0 0.23 0.05 0.03 0.00 30.12 1.52 0.05 0.01 224.7 8.7 5	59.5 2.3	2.3 7.3	1.2	3.7	0.1
SSD23LZ101GR_27 209.3 10.7 0.21 0.06 0.03 0.00 30.56 1.65 0.04 0.01 317.3 19.2 8	82.5 7.1	7.1 7.8	1.2	3.8	0.2
SSD23LZ101GR_51 208.8 9.0 0.21 0.04 0.03 0.00 30.15 1.29 0.05 0.01 381.4 19.0 1	145.7 8.0	8.0 14.4	1.8	2.7	0.0
SSD23LZ101GR_18	101.4 4.3	4.3 10.1	1.5	2.7	0.1
SSD23LZ101GR_54	130.1 10.7	10.7 13.2	2.0	2.7	0.1
SSD23LZ101GR_64	128.3 6.4	6.4 10.9	1.6	6.5	0.1
SSD23LZ101GR_8	137.7 3.4	3.4 14.5	3.2	3.1	0.1
SSD23LZ101GR_28	89.3 7.3	7.3 8.9	1.6	6.4	0.2
SSD23LZ101GR_65	86.1 3.1	3.1 8.5	1.2	4.9	0.1
	109.2 10.0	10.0 11.5	1.8	3.6	0.1
	77.2 4.2		1.6	4.0	0.1
	219.9 12.7		2.0	2.9	0.1
	74.9 2.7		1.2	3.4	0.1
	70.3 4.7		1.2	4.3	0.1